UC Merced

UC Merced Previously Published Works

Title

Multiphysics modeling of lithium-ion, lead-acid, and vanadium redox flow batteries

Permalink

Authors

Castro, Michael T
Del Rosario, Julie Anne D
Chong, Meng Nan
et al.

Publication Date

DOI

Peer reviewed

ELSEVIER

Multiphysics modeling of lithium-ion, lead-acid, and vanadium redox flow batteries

Michael T. Castro [a,f,*], Julie Anne D. Del Rosario [a,f], Meng Nan Chong [b], Po-Ya Abel Chuang [c], Jaeyoung Lee [d,e], Joey D. Ocon [a,f,*]

[a] *Laboratory of Electrochemical Engineering (LEE), Department of Chemical Engineering, University of the Philippines Diliman, Quezon City 1101, Philippines*
[b] *School of Engineering, Chemical Engineering Discipline, Monash University Malaysia, Jalan Lagoon Selatan, Bandar Sunway, Selangor Darul Ehsan, 47500, Malaysia*
[c] *Thermal and Electrochemical Energy Laboratory (TEEL), Department of Mechanical Engineering, University of California, Merced, California, 95343, USA*
[d] *Electrochemical Reaction & Technology Laboratory (ERTL), School of Environmental Science and Engineering, Gwangju Institute of Science and Technology (GIST), 123 Cheomdangwagi-ro, Buk-gu, Gwangju 61005, Republic of Korea*
[e] *Ertl Center for Electrochemistry and Catalysis, Gwangju Institute of Science and Technology (GIST), 123 Cheomdangwagi-ro, Buk-gu, Gwangju 61005, Republic of Korea*
[f] *DOST-NICER Center for Advanced Batteries, University of the Philippines Diliman, Quezon City 1101, Philippines*

ARTICLE INFO

ABSTRACT

The increasing demand for batteries' application in grid-balancing, electric vehicles, and portable electronics has prompted research efforts on improving their performance and safety features. The improvement of batteries involves the comparison of multiple battery designs and the determination of electrochemical and thermal property distributions at the continuum scale. This is achieved by using multiphysics modeling for investigatory battery research, as conventional experimental approaches would be costly and impractical. The fundamental electrochemical models for these batteries have been established, hence, new models are being developed for specific applications, such as thermal runaway and battery degradation in lithium-ion batteries, gas evolution in lead-acid batteries, and vanadium crossover in vanadium redox flow batteries. The inclusion of new concepts in multiphysics modeling, however, necessitates the consideration of phenomena beyond the continuum scale. This work presents a comprehensive review on the multiphysics models of lithium-ion, lead-acid, and vanadium redox flow batteries. The electrochemical models of these chemistries are discussed along with their physical interpretations and common applications. Modifications of these multiphysics models for adaptation and matching to end applications are outlined. Lastly, we comment on the direction of future work with regards to the interaction of multiphysics modeling with modeling techniques in other length and time scales. Molecular-scale models such as density functional theory and kinetic Monte Carlo can be used to create new multiphysics models and predict transport property correlations from first principles. Nanostructures and pore-level geometries can be optimized and integrated into continuum-scale models. The reduction of multiphysics models via machine learning, mathematical simplification, or regression enables their application in battery management systems and energy systems modeling.

1. Introduction

Batteries play a pivotal role in the fight against climate change and greenhouse gas emissions. Leading in this effort are lithium-ion (Li-ion) batteries, which are paving the way for electric vehicles due to their high energy and power density [1]. The decreasing cost of Li-ion batteries aids the penetration of renewable energy, wherein energy storage is necessary for peak shaving and frequency stabilization [2,3]. Vanadium redox flow (VRF) batteries are also gaining momentum for grid-balancing applications due to their robustness, long cycle life, and ability to have their energy and power ratings sized separately [4,5]. In addition, batteries also have traditional roles in uninterruptible power supplies[6] and automobiles [7,8]. These are supplied by the cheaper and commercially mature lead-acid battery [6–8].

The pervasive use of batteries has prompted research on their safe and efficient design, but the practicality of these studies is difficult to achieve experimentally. For example, investigating the effect of a design

Nomenclature

Abbreviation

AGM	absorptive glass mat
CFD	computational fluid dynamics
DEM	discrete element modeling
LAM	loss of active material
LCO	lithium cobalt oxide
LFP	lithium iron phosphate
Li-ion	lithium-ion
LLI	loss of lithium inventory
LMO	lithium manganese oxide
LNMO	lithium nickel manganese oxide
NCA	nickel cobalt aluminum oxide
NMC	nickel manganese cobalt oxide
SEI	solid electrolyte interphase
P2D	pseudo two-dimensional
Si/G	silicon-graphite
SPM	single particle model
SOC	state of charge
VRF	vanadium redox flow
VRLA	valve-regulated lead-acid
a	volumetric surface area, m^{-1}
a_0	initial volumetric surface area, m^{-1}
c_f	fixed site concentration, $mol\ m^{-3}$
$c_{H^+,0}^L$	initial H^+ concentration in the liquid phase, $mol\ m^{-3}$
$c_{Li^+,max}^S$	maximum Li^+ concentration in the solid phase, $mol\ m^{-3}$
d_p	particle diameter, m
D	diffusion coefficient, $m^2\ s^{-1}$
f	activity coefficient, dimensionless
F	faraday constant, $C\ mol^{-1}$
$\mathbf{g}$	acceleration due to gravity, $m\ s^{-2}$
j	reaction current density, $A\ m^{-2}$
j_0	exchange current density, $A\ m^{-2}$
$\mathbf{j}$	current density vector, $A\ m^{-2}$
k_{Li}	li-ion reaction rate constant, $m^{2.5}\ mol^{-0.5}\ s^{-1}$
K_{KC}	Kozeny-Carman coefficient, dimensionless
k_V	VRF reaction rate constant, $m\ s^{-1}$
p	pressure, Pa
$\dot{q}$	volumetric heat generation, $W\ m^{-3}$
r	radial direction in spherical coordinates, m
r_p	particle radius, m
R	ideal gas constant, $J\ mol^{-1}\ K^{-1}$
t	time, s
t_i	transference number of i, dimensionless
T	temperature, K
$\mathbf{v}$	velocity, $m\ s^{-1}$

V_{eq}	equilibrium potential, V
V_m	molar volume, $m^3\ mol^{-1}$
z_f	fixed site charge, dimensionless
z_i	charge of i, dimensionless
α_A	anodic transfer coefficient, dimensionless
α_C	cathodic transfer coefficient, dimensionless
β	Boussinesq coefficient, $m^3\ mol^{-1}$
γ	empirical current density coefficient, dimensionless
ε	volume fraction, dimensionless
η	overpotential, V
κ	hydraulic permeability, m^2
μ	viscosity, Pa s
ρ	mass density, $kg\ m^{-3}$
σ	electrical conductivity, $S\ m^{-1}$
ϕ	electric potential, V

List of superscripts

Phase	Description
L	liquid phase
S	solid phase

Location	description
N	…of the negative electrode
P	…of the positive electrode

The superscripts indicate the phase and/or location of a property. For example, ε^L means "volume fraction of the liquid" or porosity, while ε^{LN} means "porosity of the negative electrode."

List of subscripts

Label	Description
act	activation heating
eff	effective (denotes Bruggeman-corrected properties)
ele	electrical heating
ion	ionic heating
ref	evaluated at a reference state
rev	reversible heating
s	…at the surface

Species	Description
H^+	…of the H^+ ion
Li^+	…of the Li^+ ion
Pb	…of solid Pb
PbO_2	…of solid PbO_2
$PbSO_4$	…of solid $PbSO_4$
V^{2+}	…of the V^{2+} ion
V^{3+}	…of the V^{3+} ion
VO^{2+}	…of the VO^{2+} ion
VO_2^+	…of the VO_2^+ ion
i	…of species i

parameter on battery performance entails constructing and observing multiple battery setups [9–11]. This problem is amplified in battery optimization studies, wherein the design must be improved iteratively. In other studies, inactive regions in the battery are identified to enhance the utilization of battery materials [12,13]. This requires the determination of electrochemical and thermal properties at different points inside the battery. The measurements must also not interfere with the processes in the battery, which is problematic considering that some systems (e.g., Li-ion battery layers) are less than a millimeter thick. There is also growing interest regarding thermal management [14–17] and safety systems [18–22], which can be costly to design using experiments alone.

The limitations of experimental approaches are overcome by multiphysics modeling. A multiphysics model uses fundamental laws and equations from various disciplines to predict the outcome of a battery system. The equations are solved simultaneously to reflect the interdependence of physical and chemical properties. This method incurs less costs because the battery behavior is determined *in silico*. The evolution of physical and chemical property distributions in the battery system over time also arises naturally from solving the governing equations. These models typically describe the battery at the continuum scale using properties such as concentration, potential, current density, and heat generation.

One of the most popular multiphysics models was that developed by Doyle, Newman, and Fuller for Li-ion batteries. The model was based on Newman's porous electrode theory and concentrated electrolyte theory [23]. Their work in 1994 demonstrated the modeling and optimization of Li-ion batteries [24]. They then validated this model two years later
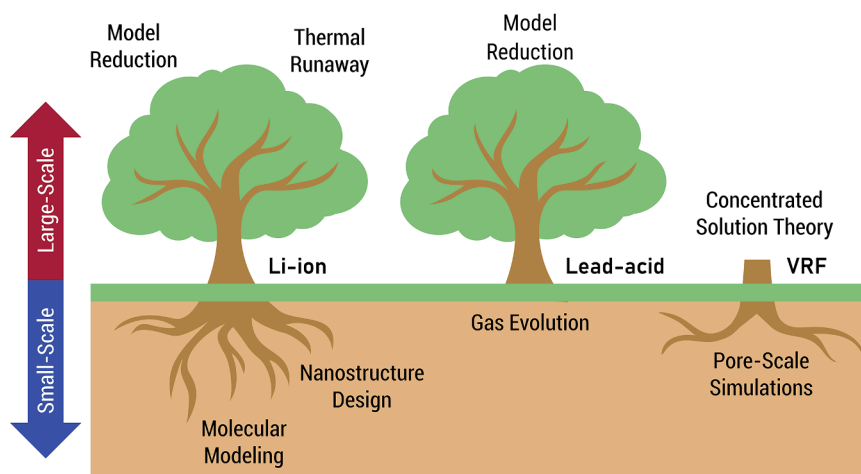
Fig. 1. Multiphysics modeling originated as a continuum-scale modeling technique, but recent work has focused on its coupling with techniques from other length scales.

[25]. Tiedemann and Newman presented the lead-acid multiphysics model earlier in 1979 [26]. Afterwards, Gu et al. improved on this in 1987 by modeling charge and rest behavior [27]. The model was also based on Newman's theories but did not account electrolyte convection induced by density differences in the electrolyte reservoir. Alavyoon et al. modeled convection in 1991 [28], enabling Gu et al. to propose a refined model in 1997 [29]. The VRF multiphysics model was introduced much later in 2008 by Shah et al. [30]. A refined model accounting for heat generation was published a year later [31].

These pioneering models, however, can predict the electrochemical operation of a battery only under ideal operating conditions. Multiphysics models have therefore been developed to account for detrimental phenomena, such as thermal runaway [32] in Li-ion batteries, gas evolution [33] and sulfation [34] in lead-acid batteries, and capacity fade due to vanadium crossover [35] in VRF batteries. Other models also described possible design improvements including Li-ion batteries with silicon negative electrodes [36], lead-acid batteries redesigned as flow batteries [37], and VRF batteries with compressed electrodes [38]. These extended multiphysics models provide a more realistic description

of batteries, allowing their safety and lifespan to be considered in addition to their performance.

While multiphysics modeling has been traditionally concerned with the continuum scale, recent work has focused on its integration with models from other length scales (Fig. 1). For instance, molecular-scale techniques, such as kinetic Monte Carlo simulations and density functional theory, have been used to predict transport properties [39] and model the formation of the solid electrolyte interphase (SEI) [40] in Li-ion batteries from first principles. On the other hand, the multiphysics model for lead-acid batteries has been simplified via data reduction [41] and regression [42] techniques, which could allow their use in battery diagnosis, energy systems modeling, and other large-scale applications that require faster models. This new paradigm broadens the applicability of multiphysics modeling as an investigatory tool.

In this review, we discuss recent developments on the multiphysics modeling of Li-ion, lead-acid, and VRF batteries along with their potential integration with studies in other length scales. These chemistries were selected due to their widespread application in renewable energy technologies in the past decade [3,43], which prompted a multitude of multiphysics modeling studies. The discussion on each chemistry is structured in four parts. First, the structure and reactions in the battery are described. Second, the electrochemical model is presented with its numerical solutions, physical interpretations, and common applications. Third, recent works on the multiphysics modeling of each battery chemistry are outlined with an emphasis on the coupling with modeling techniques from other length scales. Lastly, a commentary is made on the research direction of multiphysics modeling for each chemistry.

2. Lithium-ion

2.1. Description

Li-ion batteries consist of a graphite insertion negative electrode and an intercalation positive electrode. The Li-ion chemistry is often named after the positive electrode material – the choice of which dictates its application. Lithium cobalt oxide (LCO) is a staple in consumer electronics due to its high energy density [44]. Lithium iron phosphate (LFP) is ideal for energy storage because of its thermal stability relative to other chemistries [45]. Lithium manganese oxide (LMO) is found in fast-discharge applications [46]. Nickel cobalt aluminum oxide (NCA) and nickel manganese cobalt oxide (NMC) are gaining usage in electric vehicles due to their high energy density and low cost [47,48]. The half-reactions of graphite [49,50], LCO [51], LFP [49], LMO [52,53], NCA [54,55], and NMC [56,57] are given by (Eqs. 1–6), respectively, wherein the forward reactions occur during discharge.
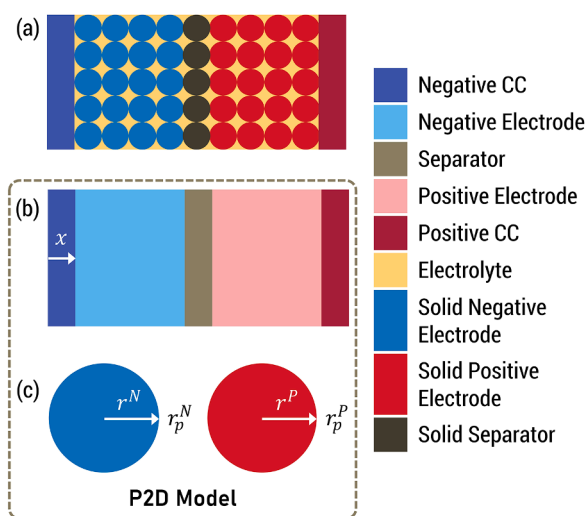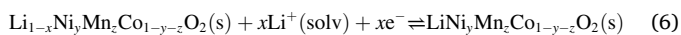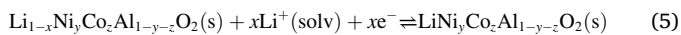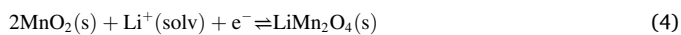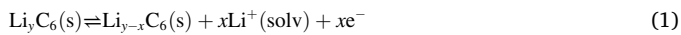

Fig. 2. Computational domain of the Li-ion battery model. The realistic description of the battery (a) is too computationally expensive to model, so the solid and liquid phases in the electrodes and separator are treated as superimposed phases (b). The solid phase is then coupled to an auxiliary spherical domain (c) to simulate the diffusion of Li^+ ions into the electrodes. The 1D battery and 1D spherical electrode models constitute the P2D model.

Table 1
Charge and mass transport equations in Li-ion batteries.

Name	Equation		Ref.
Solid phase charge transport			[73]
	$\mathbf{j}^{\mathrm{S}} = -\sigma_{\mathrm{eff}}^{\mathrm{S}} \nabla \phi^{\mathrm{S}}$	(7)	
	$\nabla \cdot \mathbf{j}^{\mathrm{S}} = -aj$	(8)	
Liquid phase charge transport			[25,72]
	$\mathbf{j}^{\mathrm{L}} = -\sigma_{\mathrm{Li}^+,\mathrm{eff}}^{\mathrm{L}} \nabla \phi^{\mathrm{L}} + \dfrac{2RT\sigma_{\mathrm{Li}^+,\mathrm{eff}}^{\mathrm{L}}}{F}\left(1 - t_{\mathrm{Li}^+}\right)\left(1 + \dfrac{\partial \ln f}{\partial \ln c_{\mathrm{Li}^+}^{\mathrm{L}}}\right)\nabla \ln c_{\mathrm{Li}^+}^{\mathrm{L}}$	(9)	
	$\nabla \cdot \mathbf{j}^{\mathrm{L}} = aj$	(10)	
Solid phase mass transport			[24,11]
	$\dfrac{\partial c_{\mathrm{Li}^+}^{\mathrm{S}}}{\partial t} = \dfrac{D_{\mathrm{Li}^+}^{\mathrm{S}}}{r^2}\left[\dfrac{\partial}{\partial r}\left(r^2 \dfrac{\partial c_{\mathrm{Li}^+}^{\mathrm{S}}}{\partial r}\right)\right]$	(11)	
	$-\nabla \cdot c_{\mathrm{Li}^+}^{\mathrm{S}}\big|_{r=0} = 0$	(12)	
	$-D_{\mathrm{Li}^+}^{\mathrm{S}} \nabla c_{\mathrm{Li}^+}^{\mathrm{S}}\big|_{r=r_p} = \dfrac{j}{F}$	(13)	
Liquid phase mass transport			[70,71]
	$\dfrac{\partial c_{\mathrm{Li}^+}^{\mathrm{L}} \varepsilon^{\mathrm{L}}}{\partial t} = \nabla \cdot \left(D_{\mathrm{Li}^+,\mathrm{eff}}^{\mathrm{L}} \nabla c_{\mathrm{Li}^+}^{\mathrm{L}}\right) + \left(1 - t_{\mathrm{Li}^+}\right)\dfrac{aj}{F}$	(14)	
Effective properties			[70,72]
	$\sigma_{\mathrm{eff}}^{\mathrm{S}} = \sigma^{\mathrm{S}} \varepsilon^{\mathrm{S}\,1.5}$	(15)	
	$D_{\mathrm{Li}^+,\mathrm{eff}}^{\mathrm{L}} = D_{\mathrm{Li}^+}^{\mathrm{L}} \varepsilon^{\mathrm{L}\,1.5}$	(16)	
	$\sigma_{\mathrm{Li}^+,\mathrm{eff}}^{\mathrm{L}} = \sigma_{\mathrm{Li}^+}^{\mathrm{L}} \varepsilon^{\mathrm{L}\,1.5}$	(17)	
Material properties			[49,72]
	$a = \dfrac{3\varepsilon^{\mathrm{S}}}{r_{\mathrm{p}}}$	(18)	

$$\mathrm{Li}_y\mathrm{C}_6(s) \rightleftharpoons \mathrm{Li}_{y-x}\mathrm{C}_6(s) + x\mathrm{Li}^+(\mathrm{solv}) + xe^- \tag{1}$$

$$\mathrm{Li}_{1-x}\mathrm{CoO}_2(s) + x\mathrm{Li}^+(\mathrm{solv}) + xe^- \rightleftharpoons \mathrm{LiCoO}_2(s) \tag{2}$$

$$\mathrm{Li}_{y-x}\mathrm{FePO}_4(s) + x\mathrm{Li}^+(\mathrm{solv}) + xe^- \rightleftharpoons \mathrm{Li}_y\mathrm{FePO}_4(s) \tag{3}$$

$$2\mathrm{MnO}_2(s) + \mathrm{Li}^+(\mathrm{solv}) + e^- \rightleftharpoons \mathrm{LiMn}_2\mathrm{O}_4(s) \tag{4}$$

$$\mathrm{Li}_{1-x}\mathrm{Ni}_y\mathrm{Co}_z\mathrm{Al}_{1-y-z}\mathrm{O}_2(s) + x\mathrm{Li}^+(\mathrm{solv}) + xe^- \rightleftharpoons \mathrm{LiNi}_y\mathrm{Co}_z\mathrm{Al}_{1-y-z}\mathrm{O}_2(s) \tag{5}$$

$$\mathrm{Li}_{1-x}\mathrm{Ni}_y\mathrm{Mn}_z\mathrm{Co}_{1-y-z}\mathrm{O}_2(s) + x\mathrm{Li}^+(\mathrm{solv}) + xe^- \rightleftharpoons \mathrm{LiNi}_y\mathrm{Mn}_z\mathrm{Co}_{1-y-z}\mathrm{O}_2(s) \tag{6}$$

The electrode layers are separated by a porous polyethylene or polypropylene separator film [58–62]. The negative and positive electrodes are fitted with copper and aluminum current collector foils, respectively [63–67]. Both electrodes are made porous to increase the active surface area for reaction. The electrolyte is 1.0 M LiPF$_6$ dissolved in organic carbonates (e.g., dimethyl carbonate, diethyl carbonate, ethylene carbonate, methyl ethyl carbonate, or mixtures thereof) [68, 69]. The battery layers may be rolled to form cylindrical cells or stacked to form pouch or prismatic cells.

2.2. Electrochemical model

2.2.1. Governing equations

The computational domain of the Li-ion multiphysics model is illustrated in Fig. 2. The electrodes of a Li-ion battery consist of numerous solid electrode particles surrounded by liquid electrolyte, while the separator is a solid polymer also soaked in liquid electrolyte (Fig. 2a). Modeling the countless electrode particles at a very fine resolution, however, is too computationally demanding. Instead, the electrode regions are approximated using Newman's porous electrode theory, which treats the solid electrode particles and the liquid electrolyte as superimposed phases (Fig. 2b). The solid phase allows the transport of both charge (electrons) and mass (Li$^+$), with the latter being modeled as the diffusion of Li$^+$ into an auxiliary spherical particle domain (Fig. 2c). The binary electrolyte [70,71] participates in simultaneous charge (charge of Li$^+$) and mass (Li$^+$) transport. The separator is also modeled according to Newman's porous electrode theory, but neither charge nor mass is transported through the solid phase (inert separator material). The current collectors are solid sheets of metal wherein only solid phase charge transport occurs. This model is known

Table 2
Kinetics in Li-ion batteries.

Name	Equation		Ref.
Current Density	$j = j_0 \left[\exp\left(\frac{\alpha_A \eta F}{RT} \right) - \exp\left(\frac{-\alpha_C \eta F}{RT} \right) \right]$	(19)	[24, 70]
Overpotential	$\eta = \phi^S - \phi^L - V_{eq}$	(20)	[24, 70]
Exchange current density	$j_0 = F k_{Li} \left(c^L_{Li^+} \right)^{\alpha_A} \left(c^S_{Li^+,s} \right)^{\alpha_C} \left(c^S_{Li^+,max} - c^S_{Li^+,s} \right)^{\alpha_A}$	(21)	[24, 70]

Table 3
Heat generation in Li-ion batteries.

Name	Equation		Ref.
Reversible heating	$\dot{q}_{rev} = ajT \frac{\partial V_{eq}}{\partial T}$	(22)	[76,77]
Activation heating	$\dot{q}_{act} = aj\eta$	(23)	[78,77]
Electrical heating	$\dot{q}_{ele} = -\mathbf{j}^S \cdot \nabla \phi^S$	(24)	[78,49]
Ionic heating	$\dot{q}_{ion} = -\mathbf{j}^L \cdot \nabla \phi^L$	(25)	[78,49]

as the pseudo-2D (P2D) model because it couples the 1D charge and mass transport in the continuum-scale domain and 1D diffusion in the particle-scale domain. The P2D model has been utilized in several studies, although other researchers have extended the continuum-scale model from 1D to 3D [68,72].

The charge and mass transport equations in Li-ion batteries are summarized in Table 1. Charge in the solid phase is transported by electrons, so the current density vector is given by Ohm's law (Eq. 7). The solid phase charge balance (Eq. 8), given by the divergence of the current density vector, reflects the generation of electrons due to the electrochemical reactions. In the liquid phase, charge transport is described by Newman's concentrated solution theory (Eq. 9). The first term on the right-hand side is the contribution of potential gradients, while the second term is that of concentration gradients. Note that Ohm's law is not strictly obeyed in the presence of large concentration gradients. The liquid phase charge balance (Eq. 10) is negative of that of the solid phase to satisfy the electroneutrality assumption.

The diffusion of Li$^+$ in the solid phase is given by Fick's law (Eq. 11). It is written in spherical coordinates with a symmetry boundary condition (Eq. 12) because of the assumed spherical shape of the solid particles. The amount of Li$^+$ that diffuses into or out of the sphere is controlled by reaction kinetics, which in turn is related to the current density (Eq. 13). In the liquid phase, mass transport of Li$^+$ is described by concentrated solution theory (Eq. 14). The first term on the right-hand side represents diffusion, while the second term denotes both migration and Li$^+$ generation.

The tortuosity of the porous materials impedes mass and charge transport, so conductivities and diffusion coefficients are adjusted using the Bruggeman correlation (Eqs. 15–17). The diffusion coefficient of Li$^+$ in the solid phase is not adjusted because the particles themselves are not porous. Rather, the porosity arises when the particles agglomerate to form the solid electrode phase. The active surface area of the electrode (Eq. 18) is derived by assuming that the particles are spherical.

The equations describing the kinetics in Li-ion batteries are summarized in Table 2. Butler-Volmer kinetics (Eq. 19) is assumed when mass transfer effects are negligible. The overpotential is defined by (Eq. 20) wherein the equilibrium potential is measured with respect to a lithium metal electrode [74]. The exchange current density (Eq. 21) is given as a function of solid and liquid phase concentration.

The equations describing heat generation in Li-ion batteries are summarized in Table 3. Heat generation in the battery is due to reactions, current-voltage (IV) losses, and heat of mixing. Electrochemical reaction heat can be subdivided into reversible and irreversible components. Reversible heating (Eq. 22) is attributed to the equilibrium potential, while irreversible or activation heating (Eq. 23) is due to the overpotential. The heat from IV losses in the solid and liquid phases are referred to as electrical heating (Eq. 24) and ionic heating (Eq. 25), respectively, and their sum is known as Joule heating or ohmic heating. The heat of mixing is often ignored due to its small magnitude [75].

The appropriate boundary conditions are then selected to close the system of partial differential equations. Ions from the liquid electrolyte in the electrode region cannot penetrate the current collector region, so a no-flux condition for both concentration and potential is placed at this interface [49,79]. Electrons from the solid phase of the electrodes cannot pass through the separator, which corresponds to a zero potential flux [70,72].

2.2.2. Electrochemical properties

A large potential gradient is observed between the tabs and the current collector plate (Fig. 3a). This is attributed to the narrowing path between the tabs and plate, which decreases the area for current flow and increases the potential gradient [49,72]. Nonuniform reaction current profiles result in the electrode region (Fig. 3b) [72,80]. Areas near the tab therefore become more utilized (Fig. 3c) [49,72,80] and accumulate stresses due to the state of charge (SOC)-dependent expansion of the electrodes [81,82]. Note that mechanical stresses are not captured
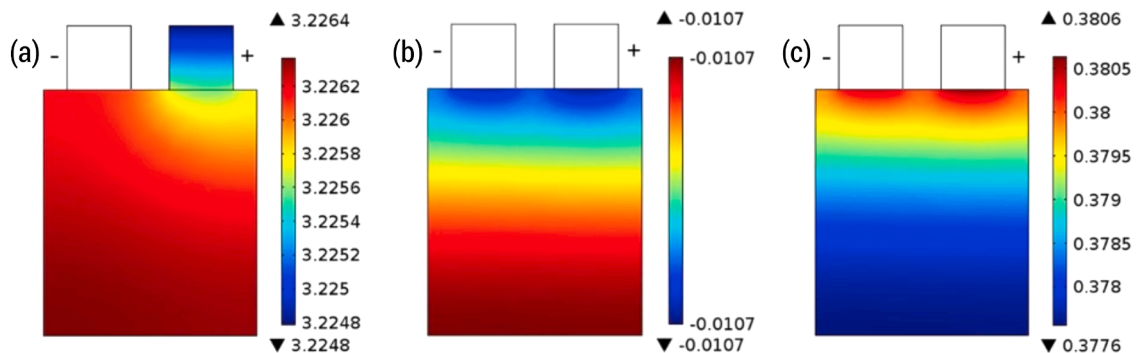

Fig. 3. Potential in the positive current collector (a) at 50% depth of discharge. Reaction current density (b) and SOC (c) distribution halfway through the positive electrode thickness at 2C discharge and 50% depth of discharge. Electrode material near the tabs is more actively utilized. (Fig. from [72])
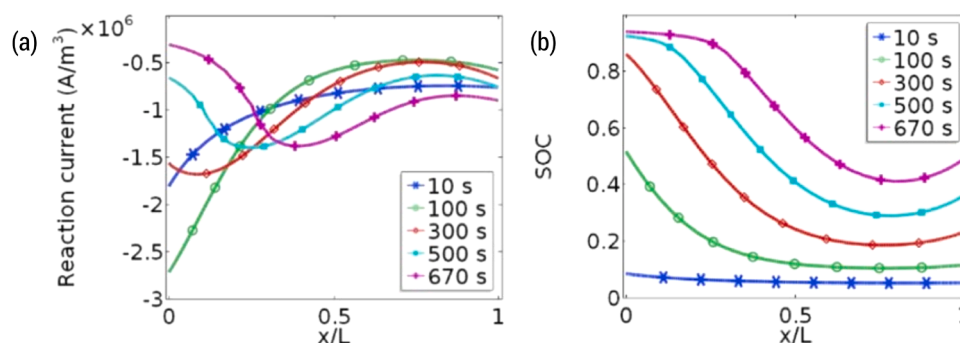
Fig. 4. Reaction current (a) and SOC (b) distributions in the positive electrode under 5C discharge. The separator-positive electrode and positive electrode-current collector interfaces are at $x/L = 0$ and $x/L = 1$, respectively. Most of the reactions occur near the separator-positive electrode interface due to the high overpotential in this area. (Fig. from [80])

by the electrochemical model, but nonetheless they can be reduced by having an even SOC distribution. Samba et al. showed that widened tabs placed on opposite sides of the battery promote a more uniform distribution of electrochemical properties [49].

The maximum reaction current initially forms at the separator-positive electrode interface (Fig. 4a) [80,83–85]. The SOC in this area saturates (Fig. 4b), and the reaction front shifts towards the current collector [80,83–85]. Thin batteries [86] under low C-rate operation [78] yield uniform concentration and SOC profiles. In the anode, the SOC profiles are more uniform in comparison [78,84].

2.2.3. Thermal properties

The large potential gradient in the current collector tabs yields high temperatures due to Joule heating, especially at high C-rates [11,49]. The effect is more pronounced in the positive tab due to the low electrical conductivity of aluminum [11,49]. The nonuniform reaction current in the positive electrode also generates higher temperatures near the positive tabs [68,80]. Optimized tab widths therefore result in uniform temperatures due to an even distribution of electrochemical properties [11,49]. Low C-rate operation also ensures that the current collectors have lower temperatures than the electrodes [11], which contributes to heat dissipation [78].

In the positive electrode, Joule heating is always maximum at the separator-positive electrode interface [80,84]. This is minimized in thinner batteries where the potential drop is lower [86] or at low C-rates where the current is small [87]. Activation and reversible heating initially develops near the separator but moves towards the current collector together with the reaction front [80,84]. Activation heating becomes significant at very low temperatures [88]. The magnitude of reversible heating depends on the chemistry [87]. It is greatest in LCO, followed by LMO and LFP [87]. The negative electrode generates more reversible heat than LFP and LMO positive electrodes, but less heat than LCO [86,87].

2.2.4. Research trends

This subsection discusses research trends regarding the continuum-scale electrochemical modeling of a Li-ion battery under normal operating conditions. Capacity fade, thermal runaway, and other non-ideal operating conditions are discussed in the succeeding sections. Existing literature on the multiphysics modeling of Li-ion batteries has touched on five commercially mature chemistries: LCO [87,89], LFP [9,49,93,94, 72,80,84,87,89–92], LMO [78,86,87,89], NCA [68,83,89,95,96], and NMC [10,11,103,104,80,89,97–102]. Nazari and Farhad compared LCO, LFP, and LMO in terms of their heat generation [87], while Zhang et al. studied the temperature increases of the five chemistries at various C-rates [89]. Both studies agree that the LFP cathode produces less heat [87,89].

There are also a handful of studies dealing with the optimization of design parameters. Hosseinzadeh et al. optimized a Li-ion battery and showed that moderately thick electrodes and small particle sizes yield a high energy density, while thin electrodes and high porosities increase the power density [9]. Li et al. noted that the thickness and porosity of the positive electrode had the largest effect on temperature rise and adjusted those parameters, among other things, to minimize the temperature rise in a Li-ion battery [10]. Mei et al. determined the current collector tab dimensions that would minimize the battery temperature [11]. This type of research is closely related to sensitivity analysis, wherein the importance of a design parameter towards the battery performance is determined. Lin et al. showed that the thickness of the positive electrode strongly influences the dischargeable capacity and maximum cell temperature [99]. Zhang et al. conducted a sensitivity analysis for a Li-ion battery, which was used to develop a methodology for identifying modeling parameters from experimental data [93].

The Li-ion battery simulations are typically performed with COMSOL Multiphysics® [9,11,49,72,80,86–88], and good agreement is usually observed between experimental and simulated voltages [9,49,72,80, 87]. Some authors have also developed computational frameworks for modeling Li-ion batteries. Newman, one of the contributors to the P2D electrochemical model, created the Dualfoil framework for simulating Li-ion batteries [105,106]. Another notable framework is LIONSIMBA written by Torchio et al. in MATLAB® [107], which boasts faster computation times than COMSOL Multiphysics® [107,108]. Kosch et al. also showed their framework, which applied orthogonal collocation and the Lobatto IIIA method to reduce computational costs [98]. Allu et al. presented their own framework and demonstrated its applicability in a variety of cell geometries [78].

2.3. Extended models

2.3.1. Mechanical stresses

Mechanical stresses in the electrodes of Li-ion batteries are attributed to thermal stresses from thermal expansion and diffusion-induced stresses from the expansion of electrodes upon lithiation [109,110]. The latter has a greater magnitude in Li-ion batteries [110] and is the focus of many studies. When left unchecked, these stresses may fracture the electrode and reduce the amount of active material electrically connected with the battery [111]. This mode of capacity loss is known as loss of active material (LAM), which was modeled by Yang et al. as a linear function of the excess strain energy resulting from mechanical stresses [112].

The mitigation of LAM sparked an interest in modeling the mechanical stresses in Li-ion batteries. At the particle scale, research is directed towards finding the stress distribution in electrode particles of various geometries. Spherical particles showed heightened stresses at contact points with other particles [82]. This was also true for spheroid particles, which experienced higher stresses than spherical particles in non-contact areas [113]. Similar observations were also found in hollow spheroid particles in comparison to hollow spherical particles,
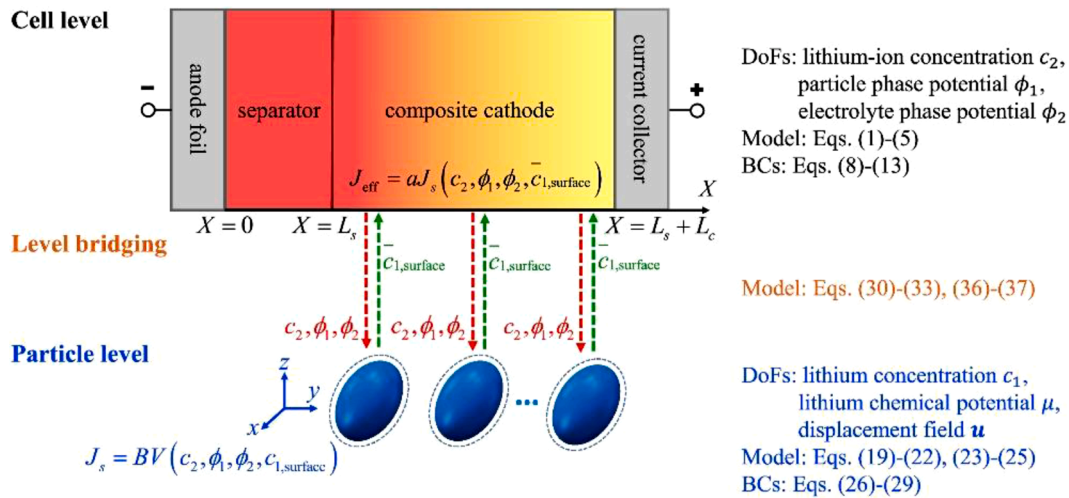
Fig. 5. The multi-scale coupling scheme developed by Bai et al. (2019) to model stresses in Li-ion batteries. Continuum-scale properties are used by the particle-scale models to predict mechanical stresses and the surface Li$^+$ concentration, which in turn, affects the continuum-scale kinetics. (Fig. from [117])

suggesting earlier fracture in the former [114]. Other studies dealt with the actual geometries of electrode particles. Kim et al. confirmed that diffusion-induced stresses are greatest at the contact point between electrode particles and that concentration gradients in these areas increase with higher C-rates [110]. Wu et al. revealed that stresses in realistically shaped particles were much higher than in spherical particles at concave areas. Moreover, the uneven stress loading in the electrode particles can promote rotation, which could damage the binder [115].

Naturally, researchers were interested in scaling up the particle-scale electrode model. One approach was to consider the solid electrode as a lattice of spheres, rather than superimposing the solid and liquid phases as with the P2D electrochemical model. This model predicts that electrode material near the separator is more utilized, which is consistent

with the P2D electrochemical model, and that stresses are higher at the contact points between particles, in line with the mechanical stress models [82]. Lower C-rates and smaller particles lead to less stresses [81]. Some authors used this approach to investigate stresses in the separator. Wu et al. found that higher C-rates result in small increases in stresses in the separator [109]. Xiao et al. argued that loose packing of particles yields tensile stresses in the separator, while close packing results in compressive stresses [116]. Other works discussed the coupling of the continuum-scale P2D electrochemical model with the particle-scale stress model (Fig. 5). Bai et al. revealed that stresses can increase diffusion, so spheroid particles had higher charge capacities than spherical particles [117]. Sauerteig et al. demonstrated that compression of a Li-ion battery due to swelling decreases ionic conductivity in the electrodes [118].
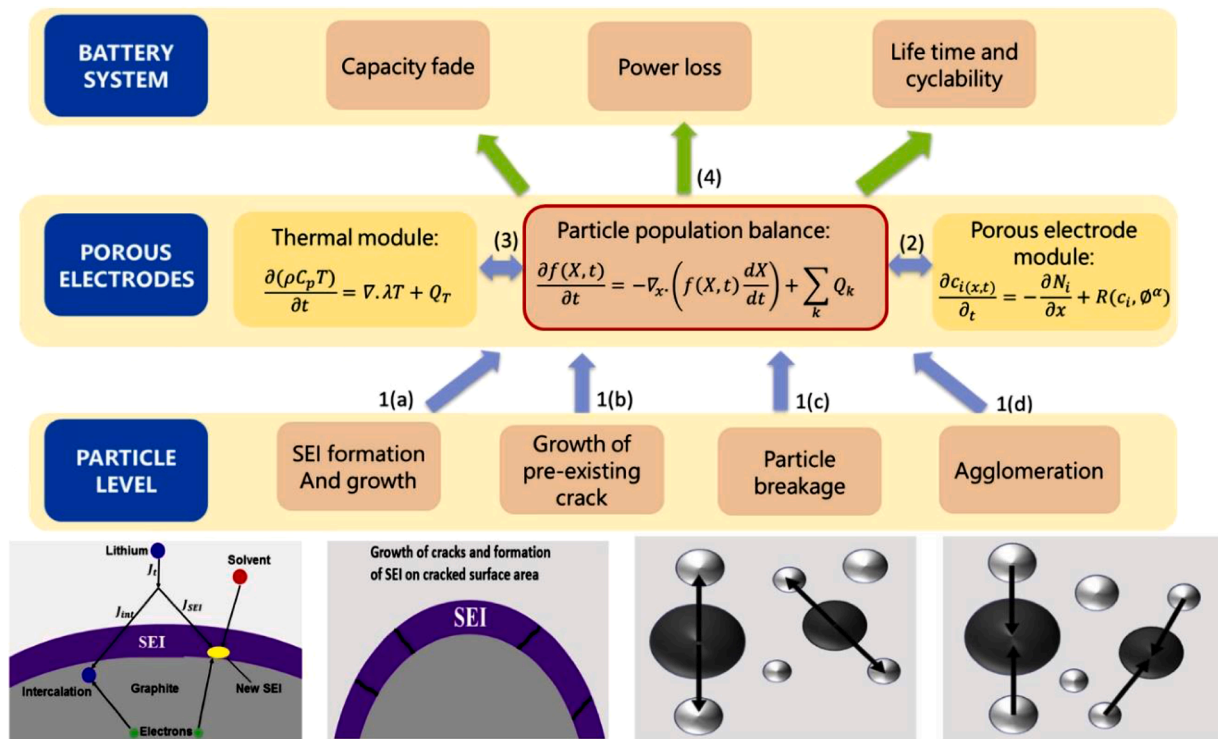

Fig. 6. The multi-scale coupling scheme developed by Tahmasbi and Eikerling (2018) to model degradation in Li-ion batteries. SEI formation, fractures, and agglomeration are statistically averaged by a particle population balance to determine electrode-scale and battery-scale properties. (Fig. from [130])

2.3.2. SEI Formation and lithium plating

The loss of lithium inventory (LLI) is another capacity fade mode defined as the depletion of Li^+ ions utilizable in electrochemical reactions [119,120]. The formation of the SEI layer on the negative electrode is one of the side reactions that contribute to LLI. The SEI layer initially forms during the first few cycles of the Li-ion battery from the decomposition of organic carbonates and $LiPF_6$ in the electrolyte. This consumes Li^+ ions found in $LiPF_6$, but this is necessary to prevent further decomposition of the electrolyte [121]. As the Li-ion battery is cycled, a different set of complex side reactions occur in the SEI. The layer thickens as more $LiPF_6$ is consumed [112,121]. SEI formation accelerates at higher temperatures [121]. Another side reaction is lithium plating, wherein Li^+ deposits on the negative electrode as metallic lithium instead of inserting itself into graphite. This occurs at high C-rates and low temperatures [122,123].

LLI contributes to greater capacity loss than LAM in Li-ion batteries [124,125], so this has been incorporated in a number of multiphysics modeling studies. Most works account only for SEI formation, which is typically modeled as a single reaction [111,112,126,127], although Xie et al. was able to consider the elementary SEI formation reactions in their work [128]. The SEI layer grows as the reaction proceeds, which results in an electrical resistance proportional to its thickness [111,112, 126–128]. Liu et al. demonstrated that optimizing a Li-ion battery for power density can also reduce the SEI thickness [129]. SEI formation occurs at the particle level, so coupling with particle-scale models is expected. Tahmasbi and Eikerling proposed a statistical physics-based degradation model accounting for SEI formation on the particles, the propagation of fractures, the growth of SEI on these fractures, and the size distribution of the electrode particles [130] (Fig. 6). Lithium plating was discussed by Yang et al., who accounted for it via Butler-Volmer kinetics. The lithium growth was modeled as an additional resistance in series with the SEI layer resistance [112].

Other researchers have focused on investigating SEI formation via molecular modeling. Understanding the growth of the SEI layer from first principles can help minimize its contribution to capacity fade [131]. Röder et al. developed an algorithm for modeling SEI formation that couples the continuum-scale Li-ion model with the short timescales and stochastic nature of kinetic Monte Carlo simulations [40]. They used the algorithm to simulate an entire discharge process [40] and determine the effect of particle size with SEI layer thickness [132]. Shinagawa et al. developed a similar model and simulated the discharge curves of a Li-ion battery after several cycles [133], effectively demonstrating a capacity fade model from first principles.

2.3.3. Silicon negative electrodes

Silicon negative electrodes have gained notable attention for use in Li-ion batteries due to their high energy density. Unfortunately, their widespread deployment is hindered by their three-fold expansion upon lithiation, which leads to increased stresses, poor cyclability, and a host of other problems. In response, models have been developed to understand the transport properties and stresses of spherical particles upon lithiation [134–137]. These studies typically employ a core-shell model wherein the region of lithiated silicon forms a shell around a silicon core. Other geometries, such as cylindrical particles [138], nanowires [139], and thin films [36,134,140,141] have also been investigated.

With a better understanding of lithiated silicon, researchers have begun using multiphysics models to mitigate stresses in silicon negative electrodes. One approach is to form the electrode into nanostructures, which provides enough clearance for silicon to expand [142,143]. For instance, Yang et al. developed a model for the lithiation of silicon nanowires that could replicate the anisotropic swelling observed in experiments [139]. Wang et al. studied the effect of varying the design parameters (i.e., aspect ratio, spacing) of silicon nanowalls on the capacity of a silicon half-cell [144]. Other studies modeled the degradation of silicon negative electrodes to suggest strategies for addressing this issue. For spherical electrode particles, Zhang et al. suggested reducing

the cutoff voltage during charging [145]. As for thin film electrodes, Pal et al. recommended using soft and elastic current collectors such as graphite and polymers [146]. An alternative strategy was investigated by Zheng et al. wherein silicon was supported by a nickel scaffold to improve its cyclability [147].

Another approach to mitigate the expansion of silicon is by using silicon-graphite (Si/G) composite electrodes. The Si/G particle is typically modeled as a core-shell structure with silicon in the outer shell and graphite in the inner core [148,149]. Some of the graphite particles in a Li-ion battery are then replaced with the Si/G particles [148]. Liu et al. coupled the P2D electrochemical model, the 3D mechanical model of the battery, and the particle-scale model. Their work revealed that a rigid battery casing would result in a slightly higher voltage and that charging at a higher C-rate causes a larger concentration gradient in the Si/G particles [149]. They also found that the size of the battery casing has little effect on the capacity [148]. Gao et al. compared distributions of silicon in a composite electrode (i.e., different Si wt% in the Si/G particles but same Si/G particle wt% in the bulk electrode vs. same Si wt% in the Si/G particles but different Si/G particle wt% in the bulk electrode) and demonstrated that the latter achieved lower stresses [150]. Their group also compared the typical core-shell structure with other structures, and showed that yolk-shell and dual-shell structures have better crack resistance [151].

2.3.4. Thermal runaway

Thermal runaway occurs when the temperature of a battery rises sharply due to runaway side reactions. The first step in the thermal runaway of a Li-ion battery is the decomposition of the SEI layer [152], which occurs at around 90°C to 120°C [153,154]. Without the SEI layer, the negative electrode is exposed and readily reacts with the electrolyte [154]. The increasing temperature then allows the positive electrode to react with the electrolyte [152,153]. The onset temperature of this step and its maximum temperature depends on the chemistry [45]. The final step in the process is the thermal decomposition of the electrolyte [152], which occurs at around 200°C [153,154]. All these reactions are exothermic, and the results can be catastrophic if the runaway reactions are not stopped.

The temperature required to trigger thermal runaway in Li-ion batteries may be initiated by internal short circuits due to puncture, crushing, and indentation. These damage the separator and permit electrical contact between the electrodes and current collectors, resulting in a large current and therefore large Joule heating [155]. Internal short circuits may occur during electric vehicle crashes [156, 157], hence its relevance in Li-ion battery research. Zhang et al. modeled the crushing of a Li-ion pouch cell and found that a larger crushed area yields a lower maximum temperature [158]. In contrast, Yuan et al. conducted a similar simulation with cylindrical Li-ion batteries and revealed that larger indenters result in larger maximum temperatures [159]. This discrepancy likely occurs because the area of crushing is larger than that of indentation, so equilibrium is reached faster. Liu et al. noted that crushing a cylindrical lithium-ion battery at a higher speed leads to a higher maximum temperature [160]. Yiding et al. simulated the crushing and indentation of a cylindrical battery and revealed that higher SOCs lead to higher maximum temperatures [161]. These observations are explained by the increase of Joule heating with current, which depends on the amount of Li^+ available for transfer from the negative to the positive electrode. Consequently, some conditions, such as low SOC and temperature, will not lead to thermal runaway [158–161]. These studies couple mechanical deformation and thermal modeling, which are reviewed extensively by Kermani and Sahraei [162] and Liu et al. [163], respectively.

Another mechanism that can initiate thermal runway is ultrafast discharge, which amplifies thermal phenomena that are often negligible under normal operating conditions. Ultrafast discharge is becoming increasingly relevant due to its application in electric vehicles. Taslimi Taleghani et al. demonstrated that an electrical contact resistance exists
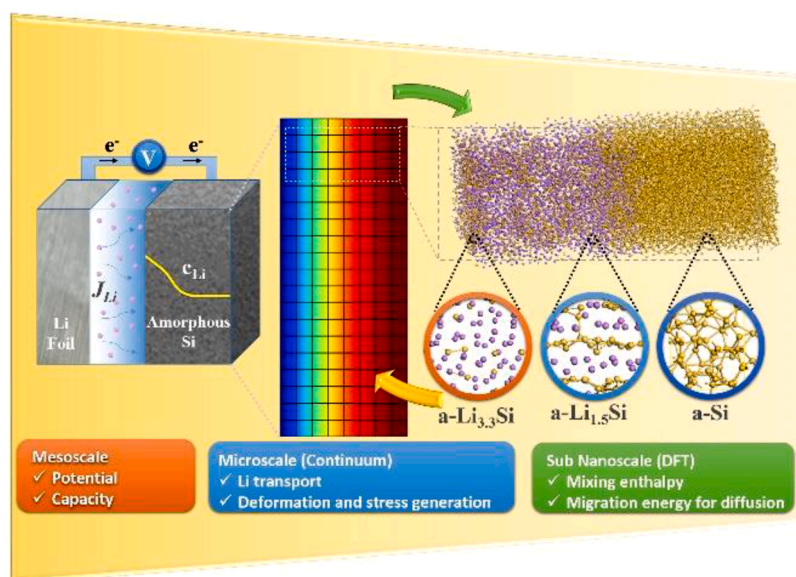
Fig. 7. The multi-scale model developed by Gwak et al. (2016) for modeling a silicon negative electrode. Physicochemical properties used by the continuum-scale models are obtained from the molecular-scale model. (Fig. from [174])

at the surface of an LFP positive electrode. This contact resistance manifests at 2C and increases greatly at higher C-rates [164]. Sangiri et al. modeled thermal contact resistances due to imperfect contact between battery components. These become significant heat generation sources at ultrahigh C-rates (10C and above) [165]. Wang et al. applied the concept of thermal inertia to Li-ion batteries after ultrafast discharge. Their model shows that the temperature of a Li-ion battery will continue increasing even after discharge has stopped [166].

The prevention of thermal runaway is a large-scale problem due to the deployment of Li-ion battery packs for electric vehicles and grid-level energy storage. In response, some researchers have focused on mapping safety regimes. For instance, Liu et al. indicated a set of SOCs and initial resistances at which thermal runaway will occur after indentation [155]. Zhang et al. demonstrated that thermal runaway can be stopped by eliminating the heat source, then presented a safety regime of heat source intensity and duration time [70]. This has also motivated the design of safety systems to stop the cascade of thermal runaway across multiple batteries via minichannels [18], phase change materials [19], firewalls [20], heatsinks [21], discharging adjacent batteries [22], and increasing the heat transfer coefficient [32]. The work of Abada et al., which used coupled battery aging and thermal runaway models, cautions that degraded batteries begin thermal runaway at a lower temperature [167]. Rheienfeld et al. also compared the thermal runaway behavior of various cell sizes and formats during external short circuits and noted the difficulty of controlling the temperature at the center of a cell [73].

Multiphysics models are valuable in the initial design and planning of safety systems, however, their computational cost implies that simplified models are more appropriate for active monitoring and control of batteries under thermal runaway. Ye et al. derived a semi-analytical thermal runway model due to nail puncture and showed that the peak temperature and heat generation depends on the puncture location [168]. Coman et al. developed a lumped model for venting in a Li-ion battery during thermal runaway [169]. An et al. developed an analytical model for the thermal runaway of a Li-ion battery due to external short circuits. The model was validated against numerical results and was used in designing a cooling strategy to stop thermal runaway [170].

2.4. Outlook

2.4.1. Molecular scale to continuum scale

Continuum-scale multiphysics models rely on empirical correlations for estimating physical properties such as equilibrium potentials, entropies, rate constants, and diffusion coefficients of the electrodes. While these properties have been determined for commercially mature chemistries, their unavailability can hinder the investigation of novel chemistries. Molecular-scale models can fill this gap as shown by recent works, which have determined physical properties from first principles. For instance, Hanke et al. replicated the concentration-dependent ionic conductivity, diffusion coefficient, and transference number of Li^+ in $LiPF_6$/propylene carbonate solutions using molecular modeling [39]. Ji et al. generated a correlation between the Li^+ diffusion coefficient in graphite and mechanical strain via density functional theory [171]. The diffusion coefficient of Li^+ in silicon has also been estimated via kinetic Monte Carlo simulations [172,173]. Gwak et al. even demonstrated a multi-scale approach that combines density functional theory with continuum-scale electrochemical and mechanical models to simulate the operation of a silicon negative electrode (Fig. 7) [174]. These studies can also generate new multiphysics models, such as the SEI formation models presented earlier, which coupled continuum-scale models and kinetic Monte Carlo simulations [40,131–133]. The predictive power of molecular-scale techniques can be harnessed by estimating physico-chemical properties of materials for use in novel chemistries, such as lithium metal batteries and the Li-ion lithium nickel manganese oxide (LNMO) chemistry. This paradigm would be valuable for scaling up research on novel battery materials.

2.4.2. Material scale to continuum scale

There have been advances in the design of Li-ion batteries, but these are now being performed at the nanoscale. Kraft et al. developed a nanostructured graphite negative electrode that can charge and discharge faster while resisting lithium plating [175]. Xu et al. also demonstrated their model of a micro-battery that utilized carbon fibers as the negative electrode [176]. Most importantly, nanostructured electrodes are viewed as a solution to mitigate the undesired expansion of silicon negative electrodes [139,144], which hold the key to high energy density batteries. These models have been experimentally validated, but the nanoscale design parameters have yet to be optimized in the same manner as continuum-scale design parameters.
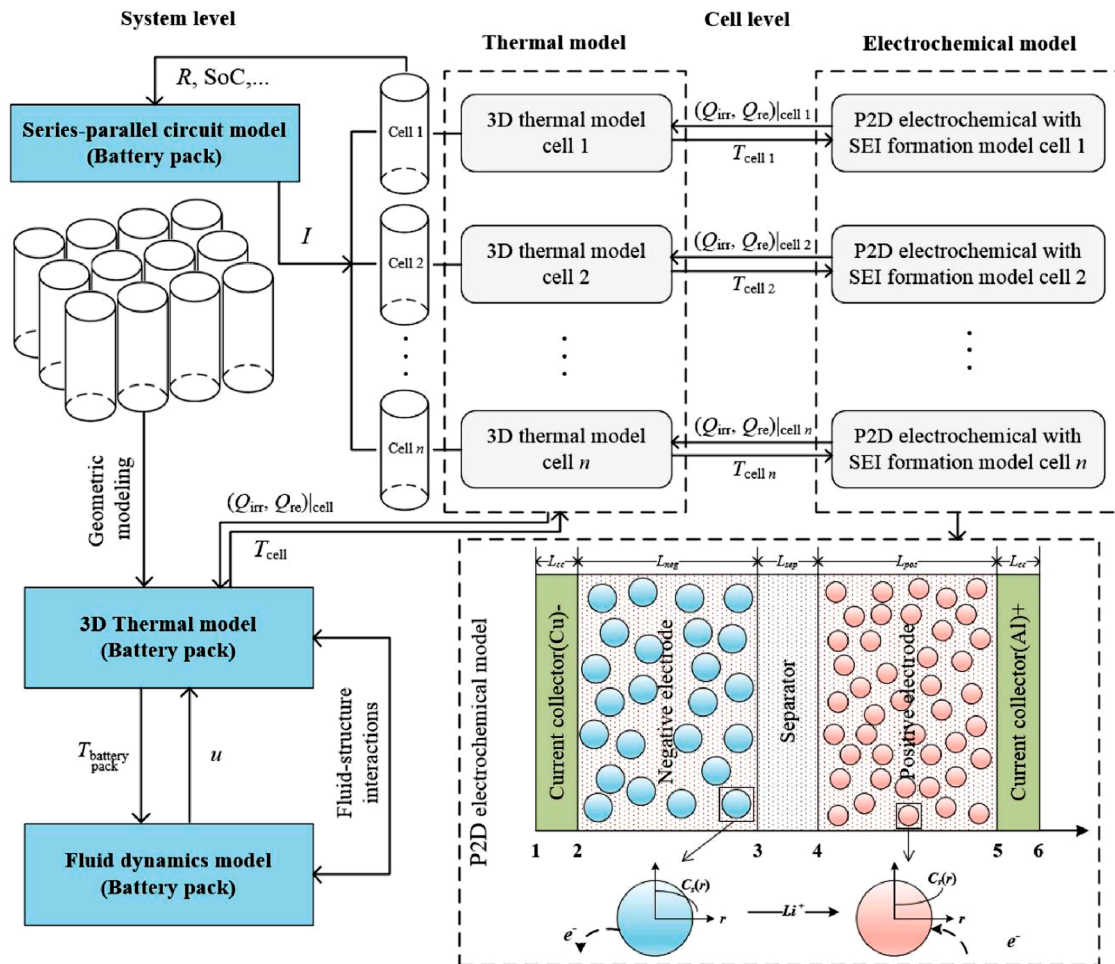
Fig. 8. The multi-scale coupling scheme developed by Xia et al. (2020) to model a battery pack. The continuum-scale electrochemical-thermal model is coupled with a pack-scale temperature distribution model. (Fig. from [16])

The multiphysics models for Li-ion batteries can also be extended based on studies at the material and particle scales. For instance, Chouchane et al. developed a 3D computational domain with realistic particle geometries to study the effects of binder placement on the electrochemical performance of Li-ion batteries [177]. Yan et al. also generated a similar domain to show that heat generation in a Li-ion battery at the continuum-scale can be affected by the inhomogeneous microstructure of graphite particles and poor contact between particles [178]. As discussed earlier, mechanical stress models typically dealt with spherical particles, but the works of Kim et al. [110] and Wu et al. [115] built on this by studying electrodes with realistic geometries in 2D. SEI formation was often modeled assuming uniform particles, but Tahmasbi and Eikerling accounted for nonuniform particle sizes by including a size distribution of spherical particles in their model [130]. Mechanical stress and SEI formation models may be refined by using a 3D computational domain with realistic particle geometries.

2.4.3. Continuum scale to system scale

Capacity fade is a particle-scale phenomena with large-scale implications. The lifespan of a battery affects its techno-economic feasibility in renewable energy systems [3] and electric vehicles [43], so efforts have been made towards reducing the computational cost of capacity fade modeling to widen its applicability from individual cells to battery packs. For instance, Zhang et al. developed a methodology for decomposing capacity fade data into LII, LAM, and under-charge or under-discharge, which was then implemented in a multiphysics model [125]. Arrhenius-type expressions were also used to estimate capacity

fade as a function of temperature and number of cycles [179,180]. Xia et al. modeled the degradation of a single Li-ion cell as a stochastic process [15,181]. This cell-level model was then used to evaluate different cell configurations in a battery pack [15], generate an appropriate cooling strategy [16] (Fig. 8), and optimize its layout [17]. Note that these studies used empirical models instead of the physics-based models introduced earlier to reduce the computational complexity. Simplified physics-based models can be implemented in future work. The modeling of capacity fade may also be linked to thermal safety, which is discussed in a review by Abada et al. [182].

Reduced-order models are also ideal for large-scale applications where the battery must be diagnosed quickly, such as in battery management systems [183–185] and the monitoring of thermal runaway [168–170]. One class of reduced-order models involves the use of machine learning models to predict the output of a multiphysics model, but with less computational cost. For example, Ragone et al. trained machine learning algorithms to replicate the SOC estimation of a multiphysics model for a Li-ion battery in an electric vehicle [186]. Yamanaka et al. simulated the thermal runaway of a Li-ion battery due to nail piercing via multiphysics modeling, then generated a machine learning model that can predict the same output given the nail piercing parameters [187]. Mathematical simplifications of the Li-ion multiphysics model have also been developed, much like the simplified thermal runaway models discussed earlier [168–170]. Tran et al. demonstrated the reduction of a Li-ion multiphysics model using Padé approximations [188]. Hennessy and Moyles derived asymptotic simplifications of the Li-ion multiphysics model under constant and periodic currents [189].

Fig. 9. Computational domain of a lead-acid battery. A flooded lead-acid battery has all the indicted domains, but a VRLA does not have an electrolyte reservoir because the electrolyte is immobilized in the separator.
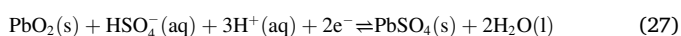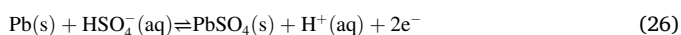
The single particle model (SPM) is another reduced-order model wherein the electrodes of the Li-ion battery are lumped into one effetive particle as opposed to multiple small particles. Lin et al. utilized the SPM to design a charging strategy that minimizes capacity fade [190]. Lotfi et al. developed an algorithm based on the SPM to monitor the state of charge of Li-ion batteries in real time [191]. Note that the SPM is widely used in the modeling of battery management systems, so there is a vast amount literature on this model beyond what is presented here. Lastly, there are equivalent circuit models wherein the battery is simplified into a network of circuit elements including voltage elements, resistors, and capacitors. This was performed for a Li-ion battery in the work of Li et al. [108]. Reduced-order models have a potential application in energy systems modeling studies wherein a battery model must be evaluated multiple times to simulate the operation of an energy system. Energy systems models often use idealized battery models [192,193] due to their simplicity, but a reduced-order model would allow for better accuracy and the consideration of cell-level design parameters [188]. Bonkile and Ramadesigan integrated the SPM into an energy systems model and simulated an off-grid solar photovoltaic and Li-ion battery system [194]. In future work, they plan to optimize the off-grid system in the same manner as techno-economic studies on renewable energy deployment.

3. Lead-acid

3.1. Description

Lead-acid batteries may be classified as either flooded or valve-regulated lead-acid (VRLA) depending on the state of the electrolyte. In a flooded lead-acid battery, the electrolyte exists in a reservoir as a free liquid. Accidental contact between electrodes is prevented by coating the negative electrode with a thin separator [195]. In contrast, the electrolyte in a VRLA battery is immobilized in either a gel [196] or an absorptive glass mat (AGM) [197]. The immobilized electrolyte doubles as a separator, so the negative electrode is not coated.

Both variants consist of a Pb negative electrode and a PbO_2 positive electrode in contact with 4.8 M H_2SO_4 electrolyte when the battery is fully charged [198–201]. The half-reactions of these electrodes are given by (Eqs. 26,27), respectively, wherein the forward reactions occur during discharge. The electrodes are made porous to increase the active surface area for reaction. The current collector, which also provides structural support, is formed into a grid instead of a solid plate to reduce the battery weight. Lead with calcium and tin additives is a common choice for the grid material [202]. Plastic or fiber grids coated with lead may be used to further reduce the battery mass [203]. Copper or aluminum anodic grids are suitable for high-power applications due to their high conductivity [203]. Titanium cathodic grids with conductive oxides increase strength and corrosion resistance [203]. For a longer cycle life, the positive electrode can be formed into tubes instead of a flat plate [204].

$$Pb(s) + HSO_4^-(aq) \rightleftharpoons PbSO_4(s) + H^+(aq) + 2e^- \qquad (26)$$

$$PbO_2(s) + HSO_4^-(aq) + 3H^+(aq) + 2e^- \rightleftharpoons PbSO_4(s) + 2H_2O(l) \qquad (27)$$

3.2. Electrochemical model

3.2.1. Governing equations

The computational domain of the lead-acid battery model is presented in Fig. 9. The current collectors are made of solid metal wherein only solid phase charge transport occurs. The electrodes are porous and are treated as superimposed solid (active electrode material) and liquid (electrolyte) phases in accordance with Newman's porous electrode theory. The active material allows only the transport of charge (electrons), unlike Li-ion batteries, because the reaction product $PbSO_4$ deposits on the electrode rather than diffusing into it. The electrolyte is concentrated and assumed to be binary because H_2SO_4 completely dissociates into H^+ and HSO_4^-, and the high H^+ concentration inhibits further dissociation of HSO_4^-. This electrolyte participates in simultaneous charge (charge of H^+) and mass (H^+) transport. The separator is also modeled according to Newman's porous electrode theory, but neither charge nor mass is transported through the solid phase (inert separator material). The electrolyte reservoir is a free liquid through which charge (charge of H^+), mass (H^+), and momentum (flow due to density differences) transport occur. This is present in flooded lead-acid batteries but not in VRLA batteries. Several studies assume a 1D model, but this can be extended to 2D if convection and acid stratification in the reservoir are to be modeled [28,29].

The charge, mass, and momentum transport equations that describe lead-acid batteries are summarized in Table 4. Charge in the solid (Eqs. 29,30) and liquid (Eqs. 31,32) phases are transported by electrons and H^+ ions, respectively. This is analogous to charge transport in Li-ion, so the charge transport equations are identical. The concentration term in (Eq. 30) is different, however, because ϕ^L is measured with the Pb/$PbSO_4$ couple as the reference electrode, as opposed to lithium metal with Li-ion batteries [74].

Mass transport of H^+ in the liquid phase is described by concentrated solution theory (Eqs. 32,33). The migration-generation term in each electrode is different because the stoichiometric coefficients of H^+ in the anode and cathode reactions are different. A convective term is included to describe the flow of electrolyte. Flow through porous media in flooded lead-acid batteries is modeled using the Darcy equation (Eq. 34), which depends on the hydraulic permeability given by the Kozeny-Carman equation (Eq. 35). Flow in the reservoir is adequately described by the Stokes equation with the Boussinesq approximation (Eq. 36). The Stokes equation results from neglecting the inertia term $\rho \mathbf{v} \cdot \nabla \mathbf{v}$ in the Navier-Stokes equation due to the small flow velocity [28], while the Boussinesq term describes flow induced by density differences in the acid reservoir. In VRLA batteries, no flow occurs because the electrolyte is immobilized (Eq. 37).

Unlike the Li-ion model, no mass transport equations are developed for the solid phase because the ions do not diffuse into the solid electrode material. Instead, the reaction products deposit on the electrode surface, which decreases the active surface area during operation (Eq. 41). The porosity also decreases during discharge because the molar volume of $PbSO_4$ is greater than that of Pb or PbO_2 (Eq. 43,44).

The equations describing electrode kinetics in lead-acid batteries are given in Table 5. Compared to the Butler-Volmer equation, the current density (Eq. 44) contains a nonlinear concentration term to account for mass transfer effects. No expression is given for the exchange current density. Instead, it is specified at a reference concentration, and any concentration dependence is incorporated in the current density expression.

The equations describing the heat generation and boundary conditions in lead-acid batteries, along with their physical interpretations, are identical to those in Li-ion batteries.

3.2.2. Electrochemical properties

The gridded design of the current collector decreases its electrical conductivity because the gaps are occupied by the electrode materials,

Table 4

Charge, mass, and momentum transport equations in lead-acid batteries.

Name	Equation		Ref.
Solid phase charge transport			[29,201]
	$\mathbf{j}^{\mathrm{S}} = -\sigma_{\mathrm{eff}}^{\mathrm{S}} \nabla \phi^{\mathrm{S}}$	(28)	
	$\nabla \cdot \mathbf{j}^{\mathrm{S}} = -aj$	(29)	
Liquid phase charge transport			[29,205,34]
	$\mathbf{j}^{\mathrm{L}} = -\sigma_{\mathrm{H^+,eff}}^{\mathrm{L}} \nabla \phi^{\mathrm{L}} + \dfrac{RT\sigma_{\mathrm{H^+,eff}}^{\mathrm{L}}}{F}(1-2t_{\mathrm{H^+}})\nabla \ln c_{\mathrm{H^+}}^{\mathrm{L}}$	(30)	
	$\nabla \cdot \mathbf{j}^{\mathrm{L}} = aj$	(31)	
Liquid phase mass transport			[29,205,34,206]
	$\dfrac{\partial c_{\mathrm{H^+}}^{\mathrm{LN}} \varepsilon^{\mathrm{LN}}}{\partial t} + \mathbf{v}^{\mathrm{N}} \cdot \nabla c_{\mathrm{H^+}}^{\mathrm{LN}} = \nabla \cdot \left(D_{\mathrm{H^+,eff}}^{\mathrm{LN}} \nabla c_{\mathrm{H^+}}^{\mathrm{LN}} \right) + (1-2t_{\mathrm{H^+}})\dfrac{a^{\mathrm{N}}j^{\mathrm{N}}}{2F}$	(32)	
	$\dfrac{\partial c_{\mathrm{H^+}}^{\mathrm{LP}} \varepsilon^{\mathrm{LP}}}{\partial t} + \mathbf{v}^{\mathrm{P}} \cdot \nabla c_{\mathrm{H^+}}^{\mathrm{LP}} = \nabla \cdot \left(D_{\mathrm{H^+,eff}}^{\mathrm{LP}} \nabla c_{\mathrm{H^+}}^{\mathrm{LP}} \right) + (3-2t_{\mathrm{H^+}})\dfrac{a^{\mathrm{P}}j^{\mathrm{P}}}{2F}$	(33)	
Liquid phase flow in porous media (flooded, at least 2D)			[29]
	$\varepsilon^{\mathrm{L}} \mathbf{v} = \dfrac{\kappa}{\mu}\left[\nabla p - \rho^{\mathrm{L}} \mathbf{g}\left[1 + \beta\left(c_{\mathrm{H^+}}^{\mathrm{L}} - c_{\mathrm{H^+},0}^{\mathrm{L}} \right) \right] \right]$	(34)	
	$\kappa = \dfrac{d_{\mathrm{p}}^2 \varepsilon^{\mathrm{L}\,3}}{16 K_{\mathrm{KC}}(1-\varepsilon^{\mathrm{L}})^2}$	(35)	
Liquid phase flow in reservoir (flooded, at least 2D)			[28,207]
	$0 = -\nabla p + \mu \nabla^2 \mathbf{v} - \rho^{\mathrm{L}} \mathbf{g}\left[1 + \beta\left(c_{\mathrm{H^+}}^{\mathrm{L}} - c_{\mathrm{H^+},0}^{\mathrm{L}} \right) \right]$	(36)	
Liquid phase flow (VRLA)			[206,201]
	$\mathbf{v} = 0$	(37)	
Effective properties			[29,205,200,201]
	$\sigma_{\mathrm{eff}}^{\mathrm{S}} = \sigma^{\mathrm{S}} \varepsilon^{\mathrm{S}\,1.5}$	(38)	
	$D_{\mathrm{H^+,eff}}^{\mathrm{L}} = D_{\mathrm{H^+}}^{\mathrm{L}} \varepsilon^{\mathrm{L}\,1.5}$	(39)	
	$\sigma_{\mathrm{H^+,eff}}^{\mathrm{L}} = \sigma_{\mathrm{H^+}}^{\mathrm{L}} \varepsilon^{\mathrm{L}\,1.5}$	(40)	
Material properties			[29,200,201]
	$a = \begin{cases} a_0\left[1 - \mathrm{SOC}^{0.55} \right] & \text{charge} \\ a_0 \mathrm{SOC}^{0.55} & \text{discharge} \end{cases}$	(41)	
	$\dfrac{\partial \varepsilon^{\mathrm{LN}}}{\partial t} = \left(V_{\mathrm{m,Pb}} - V_{\mathrm{m,PbSO_4}} \right)\dfrac{a^{\mathrm{N}}j^{\mathrm{N}}}{2F}$	(42)	
	$\dfrac{\partial \varepsilon^{\mathrm{LP}}}{\partial t} = \left(V_{\mathrm{m,PbSO_4}} - V_{\mathrm{m,PbO_2}} \right)\dfrac{a^{\mathrm{P}}j^{\mathrm{P}}}{2F}$	(43)	

which become less conductive upon conversion to $PbSO_4$. The ohmic drop creates a large potential gradient near the current collector lugs (Fig. 10b), which induces a nonuniform reaction current (Fig. 10c) [12, 13]. Electrochemical property distributions are made uniform by using diagonal grids, placing the current collector lug in the middle (Fig. 10d), and tapering the grid wires [12,13].

Across the positive electrode, the maximum reaction current initially develops at the reservoir-positive electrode interface [201,208]. Electrode materials near the separator are utilized [201,209,210], and decrease in porosity [208] (Fig. 11a). Diffusion into the positive electrode is hindered, and acid concentration becomes appreciable only at the separator-current interface [199,201,205,208,210]. The reaction

Table 5

Kinetics in lead-acid batteries.

Name	Equation	Ref.
Current density	$$j = j_0 \left(\frac{c_{H^+}^L}{c_{H^+,ref}^L}\right)^\gamma \left[\exp\left(\frac{\alpha_A \eta F}{RT}\right) - \exp\left(\frac{-\alpha_C \eta F}{RT}\right)\right] \quad (44)$$	[200, 201]
Overpotential	$$\eta = \phi^S - \phi^L - V_{eq} \quad (45)$$	[205]

front consequently remains at the reservoir-positive electrode interface [201,208], unlike in Li-ion batteries. The porosity decreases more in the positive electrode. Diffusion in the negative electrode is therefore less restricted, creating uniform SOC [201,209,210] (Fig. 11b) and concentration [199,201,205,208,210] profiles.

3.2.3. Research Trends

The small number of studies about the multiphysics modeling of lead-acid batteries is in stark contrast with the vast amount of literature available about Li-ion batteries. Research on computational frameworks predate the 2010's [199,208], while modern studies are typically conducted using COMSOL Multiphysics® [12,13,205]. Minimal discrepancy between simulations and experiments is observed with discharge curves [199,201,210]. Unlike with Li-ion batteries, there appears to be
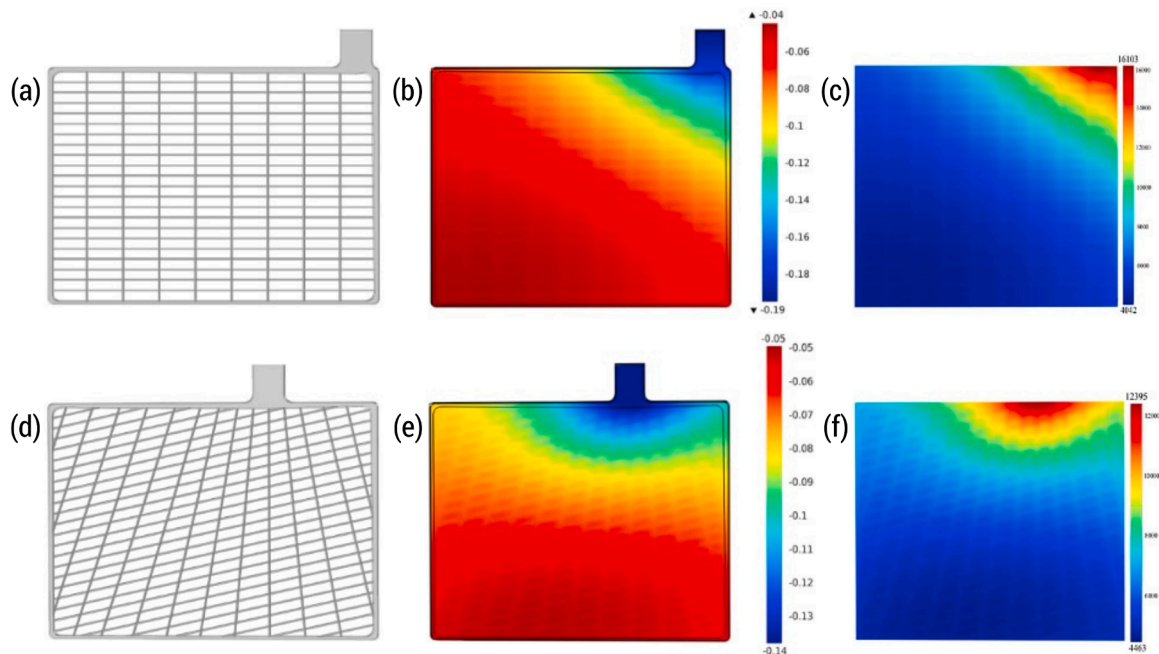
Fig. 10. A current collector grid with horizontal and vertical wires and a lug placed on the edge (a), and the corresponding potential distribution in the electrode (b) and reaction current density in the surrounding electrolyte (c). A grid with diagonal wires and a lug near the center (d) yields more uniform potential (e) and reaction current density (f) distributions. These are calculated assuming a 100 A discharge current and a 4.8 M H_2SO_4 electrolyte. (Fig. from [12])
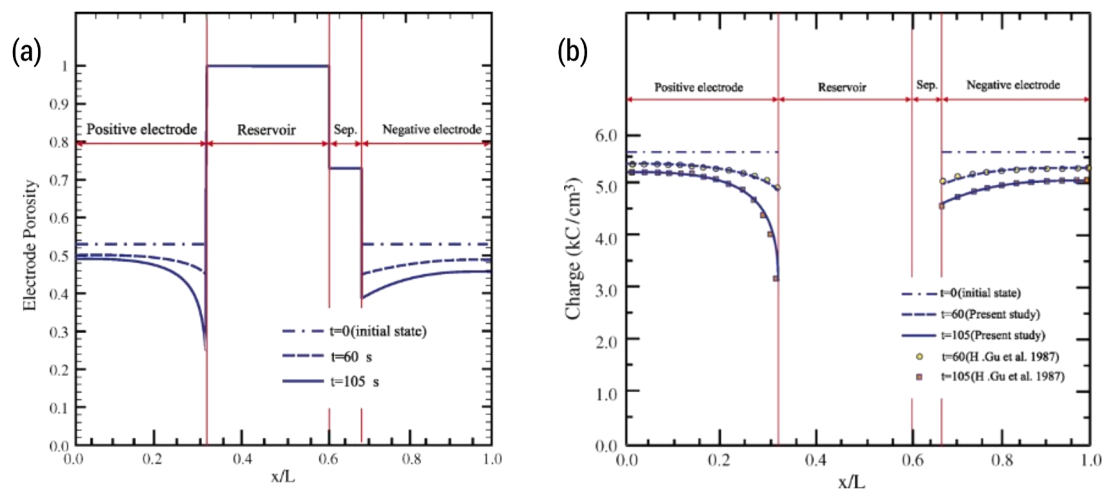

Fig. 11. Porosity (a) and charge (b) distributions in a lead-acid battery. The reaction occurs mostly near the reservoir-positive electrode interface, which explains the decreased porosity and charge at that area. (Fig. from [208])
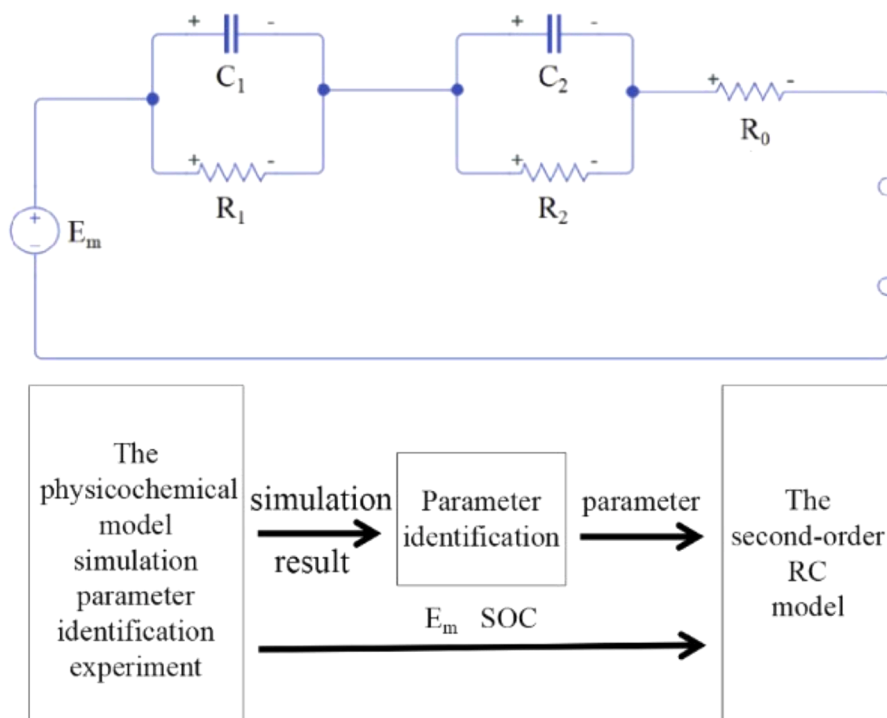
Fig. 12. The model simplification scheme developed by Shi et. al. (2020). The resistances, capacitances, and open circuit potential in the equivalent circuit model are determined from a multiphysics model. (Fig. from [42]).

no motivation to develop faster computational frameworks without resorting to lumped models or reduced-order models.

There have been studies dealing with the transient behavior and control of a lead-acid battery. Nazghelichi et al. identified regions in terms of dimensionless numbers wherein charging may lead to thermal runaway, which they then used to develop a strategy for reducing the charging time of a lead-acid battery [211]. Tenno and Nefedov came up with controls that maximizes the discharge current and capacity of a lead-acid battery while preventing electrolyte depletion [205]. Huck and Sauer noted that the continuum-scale electrochemical model neglects short-term transient effects, so they modified the lead-acid multiphysics model to account for such phenomena [207]. The transient behavior of thermal phenomena was discussed by Siniard et al. [210].

3.3. Extended models

3.3.1. Side reactions

Gas evolution is an important side reaction that occurs during charging. O_2 evolves from the positive electrode (Eq. 46), while H_2 evolves from the negative electrode (Eq. 47). To account for these processes, additional migration-generation terms representing the side reactions are added to the liquid phase mass transport equation [33,206,212]. The transport of dissolved O_2 is also modeled [33,206,212]. These side reactions consume electrons otherwise intended for the main reactions, so they also contribute to sulfation or the irrecoverable formation of $PbSO_4$ [198,213].

$$2H_2O(l) \rightarrow O_2(g) + 4H^+(aq) + 4e^- \tag{46}$$

$$2H^+(aq) + 2e^- \rightarrow H_2(g) \tag{47}$$

3.3.2. Flow battery

The lead-acid battery has been redesigned as a flow battery for grid-scale energy storage applications. Flow batteries are easier to scale up than the conventional battery design. Energy and power can also be sized independently by increasing the reactant tank volume or

increasing the active surface area, respectively. The redesign, however, requires modifications to the traditional lead-acid chemistry. The lead-acid flow battery still uses a Pb negative electrode and a PbO_2 positive electrode, but the electrolyte is replaced with lead methanesulfonate Pb $(CH_3SO_3)_2$ dissolved in methanesulfonic acid CH_3SO_3H. The anodic (Eq. 48) and cathodic (Eq. 49) reactions no longer form $PbSO_4$, and the ionic charge carrier is now Pb^{2+} instead of H^+. The forward reactions in these equations occur during discharge. This chemistry is advantageous over other flow chemistries because it does not need a selective membrane.

$$Pb(s) \rightleftharpoons Pb^{2+}(aq) + 2e^- \tag{48}$$

$$PbO_2(s) + 4H^+(aq) + 2e^- \rightleftharpoons Pb^{2+}(aq) + 2H_2O(l) \tag{49}$$
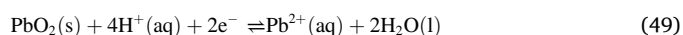
The chemistry and design of flow batteries are different from a lead-acid cell, so a new multiphysics model must be developed. Shah et al. developed the earliest model for this system, which assumed that the electrolyte is pumped between the positive and negative electrodes [37]. This model was later validated experimentally by Bates et al. [214]. Other researchers have proposed alternative designs. Zhang et al. demonstrated that covering the electrode with conductive dots promotes a uniform reaction rate while reducing the amount of active material [215]. Oury et al. investigated a honeycomb geometry for the positive electrode [216].

3.4. Outlook

3.4.1. Material scale to continuum scale

Several experimental studies have demonstrated the use of nanostructured electrodes for reducing the charging time and increasing the capacity [217,218] of lead-acid batteries. Literature regarding the multiphysics modeling of nanostructured electrodes for lead-acid batteries is scarce, however. To date, only the work of Madusanka et al. has investigated the impacts of nanostructured lead-acid battery electrodes at the continuum scale via multiphysics modeling. They found that nanostructured electrodes can improve the voltage and capacity of the lead-acid battery [209]. As discussed earlier, models of nanostructured
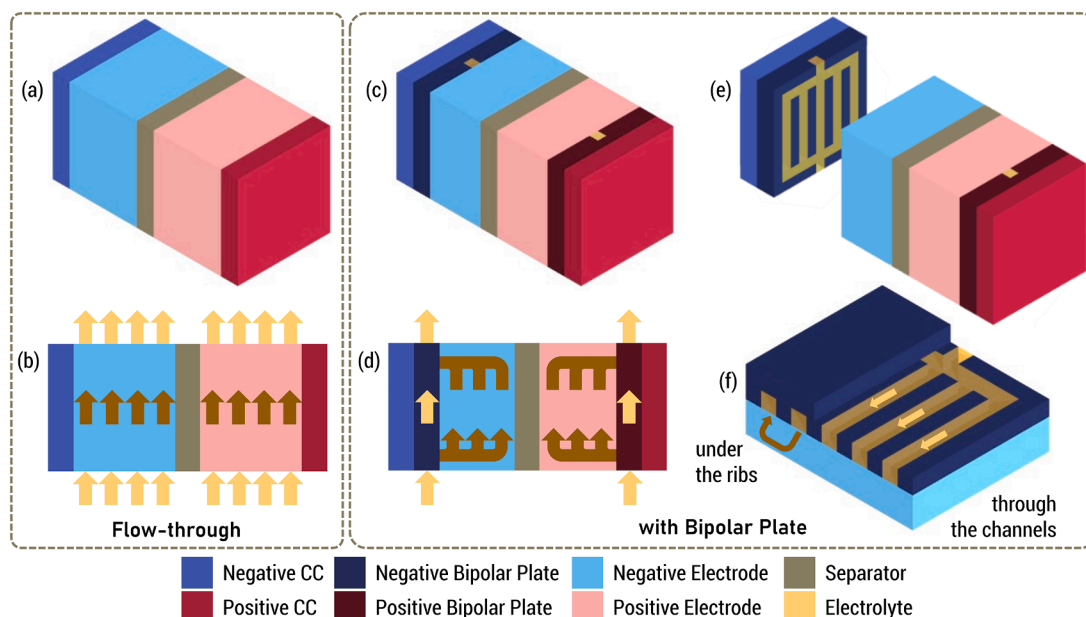
Fig. 13. The flow-through design consists of current collectors, electrodes, and a selective membrane (a). Electrolyte is pumped directly into the electrodes (b). An alternative design contains a bipolar plate (c), which distributes the electrolyte (d). The bipolar plate is placed between the current collector and the electrodes with the flow channels contacting the electrodes (e). Electrolyte may pass through the flow channels or under the ribs (f).

electrodes have advanced the study of silicon negative electrodes for Li-ion batteries, so this may be a worthwhile pursuit for lead-acid batteries as well.

3.4.2. Continuum scale to system scale

Lead-acid batteries are deployed in large-scale applications such as uninterruptable power supplies and automobiles. This could explain the small number of multiphysics modeling studies on lead-acid batteries, as large-scale applications require simpler models for rapid evaluation and diagnosis. Recent work has therefore focused on developing reduced-order models, which have a lower computational cost. For example, Sulzer et al. reduced the lead-acid model into three different asymptotic models while preserving material characteristics such as porosity [219]. Shahbazi and Esfahanian applied cluster analysis methods to yield a reduced-order lead-acid model that accurately predicted discharge curves, concentration profiles, and SOC profiles [41]. Shi et al. demonstrated an alternative approach wherein the results of a multi-physics model were incorporated into an equivalent circuit model [42] (Fig. 12). These simplified models preserve essential physics regarding the battery while still being fast enough for large-scale applications.

4. Vanadium redox flow

4.1. Description

Before discussing the reactions and materials involved in a VRF battery, it is best to describe the flow battery and its differences with conventional batteries such as Li-ion and lead-acid. A conventional battery has negative and positive electrodes that serve as the active materials. The electrolyte usually only transports the ionic current and is not consumed in the net reaction, except in lead-acid batteries. In contrast, the active materials in a flow battery are the anolyte and catholyte, which are the electrolytes at the negative and positive electrodes, respectively. The electrode typically only conducts the electric current and does not participate in the reactions, although the lead-acid flow battery discussed earlier is an exception. The anolyte and catholyte are separated by a selective membrane to prevent the undesired crossover of some species. The electrolytes are stored in tanks and pumped into the battery during charge or discharge.

Flow batteries may either be flow-through or may have bipolar plates. In a flow-through design (Fig. 13a), the electrolytes are pumped directly into the porous electrode (Fig. 13b). During discharge, electric current flows from the positive electrode to the positive current collector, to the external circuit, to the negative current collector, and finally
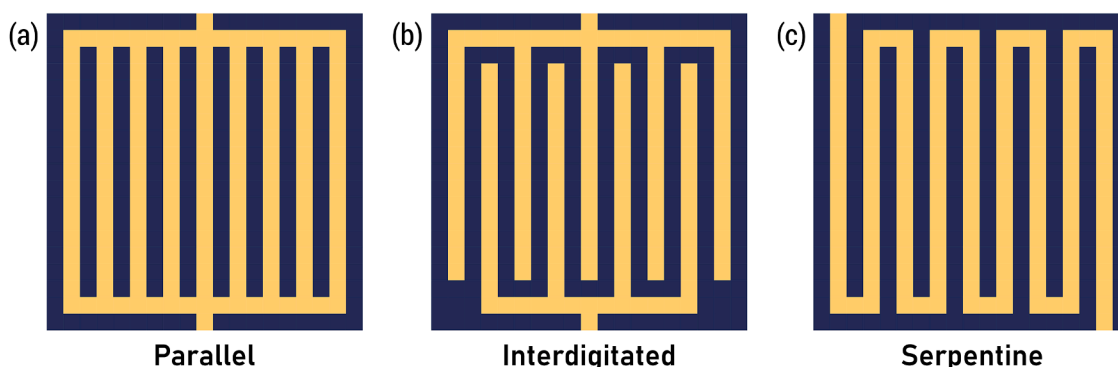

Fig. 14. Parallel (a), interdigitated (b), and serpentine (c) designs are commonly studied for use in VRF batteries.
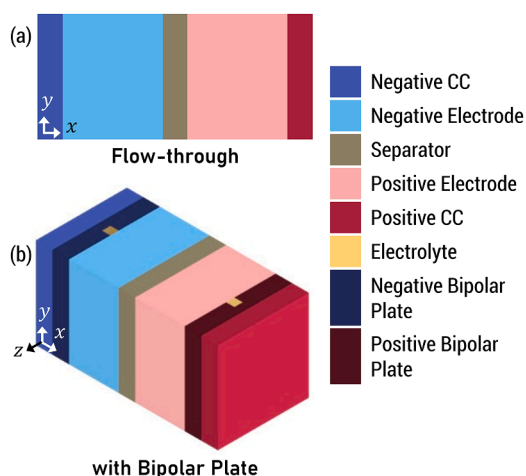
Fig. 15. Computational domain of a VRF battery. The flow-through design can be modeled in 2D (a), while designs with the bipolar plate often involve a 3D domain (b).

to the negative electrode. Other designs contain bipolar plates (Fig. 13c) through which the electrolyte is pumped (Fig. 13d). These are sandwiched between the current collectors and the porous electrodes (Fig. 13e). The electrolyte may follow the flow channels engraved in the bipolar plates. It may also flow from the flow channels, under the ribs and into the electrodes, then back to the flow channels (Fig. 13f). The bipolar plates are electrically conductive, so electric current during discharge flows from the positive electrode, to the positive bipolar plate, to the positive current collector, to the external circuit, to the negative current collector, to the negative bipolar plate, and lastly to the negative electrode.

In a VRF battery, the anolyte is 1.5 M vanadium ions (V^{2+}/V^{3+}) in 5 M sulfuric acid, while the catholyte is 1.5 M vanadium ions (VO_2^+/VO^{2+}) in 5 M sulfuric acid [220]. The corresponding half-reactions are shown in (Eqs. 50,51), respectively [221], wherein the forward reactions occur during discharge. The electrodes are made from unreactive carbon paper [222] or carbon felt [223], while the half-cells are separated by a membrane selective to H^+, such as Nafion [224,225].

$$V^{2+}(aq) \rightleftharpoons V^{3+}(aq) + e^- \tag{50}$$

$$VO_2^+(aq) + 2H^+(aq) + e^- \rightleftharpoons VO^{2+}(aq) + H_2O(l) \tag{51}$$
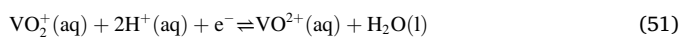
As for the bipolar plates, the parallel, interdigitated, and serpentine patterns are common flow field designs in VRF batteries (Fig. 14), although others also exist. A parallel design allows the electrolyte to easily flow through the channels [226]. In contrast, the interdigitated pattern is not continuous from the inlet to the outlet, so electrolyte is forced to flow under the ribs [226–229]. The serpentine flow field is a middle ground between the parallel and interdigitated patterns. It is continuous, but the long and winding path encourages flow under the ribs at the switchbacks for a shorter path [227,228].

4.2. Electrochemical model

4.2.1. Governing equations

The computational domain of the VRF battery model is shown in Fig. 15. The flow-through design is often modeled in 2D (Fig. 15a) [230, 231]. The current collectors are solid conductors wherein only solid phase charge transport occurs. The electrodes are porous and are treated as superimposed solid (carbon) and liquid (electrolyte) phases in accordance with Newman's porous electrode theory. The solid phase participates in charge transport (electrons) only, while the electrolyte allows simultaneous charge (charge of ions), mass (ions), and momentum transport. The separator is also modeled according to

Newman's porous electrode theory, but neither charge nor mass is transported through the solid phase (inert separator material). The separator is selective, and only the mass transport of H^+ in the liquid phase is permitted. Simulations involving flow channels are often carried out in 3D (Fig. 15b) [226,227]. The bipolar plate is a solid electrical conductor just like the current collectors, while the flow channel is a free liquid wherein charge (charge of ions), mass (ions), and momentum transport occurs.

The charge, mass, and momentum transport equations in VRF batteries are summarized in Table 6. Charge in the solid phase is transported by electrons, so the current density vector is given by Ohm's law (Eq. 52). Charge in the liquid phase (Eq. 53) is transported by multiple ions, so the charge flux (i.e., mass flux multiplied by charge) of each ion is added. The terms in the summation, from left to right, indicate the effects of diffusion, migration, and convection, respectively. The charge balance (Eq. 54) represents electron generation due to the reactions. The selective membrane, however, has its own charge transport equations. It contains fixed sites with charge z_f and concentration c_f that facilitate the transport of H^+. Because the solid phase is charged, the liquid phase must have an equal and opposite charge ($c_{H^+}^L = -z_f c_f = (\text{constant})$) so that the membrane is electrically neutral [30]. Simplifying the porous electrode equations under the described conditions yields the charge transport equations (Eqs. 55,56) in the membrane. Note that the diffusion coefficient of H^+ depends on the membrane.

Mass transport equations (Eq. 57) are developed for each ion. The terms, from left to right, represent accumulation, convection, diffusion, migration, and species generation, respectively. These equations were derived from the Nernst-Planck equation, which describes the mass flux of ions in dilute solutions. Unlike the mass transport equation for a concentrated binary electrolyte, the migration and species generation terms are separated. The stoichiometric coefficient of H^+ is different in the anodic and cathodic reactions, so an equation is developed for each electrode. In the separator, the flux of H^+ is dictated mostly by the potential gradient (Eq. 58).

The flow of electrolyte through the porous electrodes is described by the Brinkman equation (Eq. 59) with the Kozeny-Carman equation (Eq. 60). The application of the Darcy equation is equally valid [232], but the Brinkman equation ensures a smooth transition to the Navier-Stokes equation in the flow channel [227] (Eq. 61).

The equations describing kinetics in VRF batteries are given in Table 8. The current density (Eqs. 64,65) is given by a modified Butler-Volmer equation that accounts for mass transfer effects. The overpotential (Eq. 66) [237] in the negative and positive electrodes depend on the equilibrium potential of the V^{2+}/V^{3+} and VO_2^+/VO^{2+} half-reactions, respectively. The exchange current densities are given by (Eq. 67,68).

The equations describing heat generation in VRF batteries, along with their physical interpretation, are identical to those in Li-ion and lead-acid batteries. The boundary conditions in VRF batteries, however, are different. Ions from the liquid electrolyte cannot penetrate the bipolar plates or current collectors, so no-flux conditions are placed at their interface [35,226,234]. A no-slip condition is also assumed between the electrolyte in the flow channel and the bipolar plate [226]. Electrons in the solid phase of the electrode cannot pass through the membrane, so a zero potential flux is imposed [230]. The membrane is selective to H^+, so the flux of all other ions through the membrane is zero [30,31]. The concentration of H^+ at the electrode-membrane interface is given by the Donnan boundary condition [234].

4.2.2. Hydraulic properties

The velocity profile depends on the flow field design. Flow under the ribs is minimal in a parallel flow field [226]. In contrast, electrolyte velocity in the electrodes is highest under the ribs of an interdigitated design (Fig. 16a) [226–229]. This velocity is uniform along the length of the channels [226–229]. In a serpentine flow field, the electrolyte

Table 6
Charge, mass, and momentum transport equations in VRF batteries.

Name	Equation		Ref.
Solid phase charge transport			[233]
	$\mathbf{j}^S = -\sigma_{\text{eff}}^S \nabla \phi^S$	(52)	
Liquid phase charge transport			[227,231]
	$\mathbf{j}^L = \sum_i \left[-z_i F D_{i,\text{eff}}^L \nabla c_i^L - \dfrac{z_i^2 F^2 D_{i,\text{eff}}^L c_i^L}{RT} \nabla \phi^L + z_i F c_i^L \mathbf{v} \right]$	(53)	
	$\nabla \cdot \mathbf{j}^L = aj$	(54)	
Liquid phase charge transport (separator)			[234,230]
	$\mathbf{j}^L = \dfrac{z_f F^2 D_{H^+}^L c_f}{RT} \nabla \phi^L$	(55)	
	$\nabla \cdot \mathbf{j}^L = 0$	(56)	
Liquid phase mass transport[1]			[227,226,235]
	$\dfrac{\partial \varepsilon^L c_i^L}{\partial t} + \mathbf{v} \cdot \nabla c_i^L = \nabla \cdot \left[D_{i,\text{eff}}^L \nabla c_i^L + \dfrac{z_i D_{i,\text{eff}}^L F c_i^L}{RT} \nabla \phi^L \right] - \dfrac{s_i aj}{F}$	(57)	
Liquid phase mass transport (separator)			[232]
	$\dfrac{\partial \varepsilon^L c_{H^+}^L}{\partial t} = -\nabla \cdot \left[\dfrac{z_f D_{H^+}^L c_f F}{RT} \nabla \phi^L \right]$	(58)	
Liquid phase flow (porous)			[227,230,236]
	$\dfrac{\rho^L}{\varepsilon^{L2}} \mathbf{v} \cdot \nabla \mathbf{v} = -\nabla p + \nabla \cdot \left[\dfrac{\mu}{\varepsilon^L} \left(\nabla \mathbf{v} + \nabla \mathbf{v}^T \right) \right] - \dfrac{\mu}{\kappa} \mathbf{v}$	(59)	
	$\kappa = \dfrac{d_p^2 \varepsilon^{L3}}{16 K_{KC} (1 - \varepsilon^L)^2}$	(60)	
Liquid phase flow (flow channel)			[230]
	$\rho^L \mathbf{v} \cdot \nabla \mathbf{v} = -\nabla p + \mu \nabla^2 \mathbf{v} + \mathbf{g}$	(61)	
Effective properties			[233]
	$\sigma_{\text{eff}}^S = \sigma^S \varepsilon^{S1.5}$	(62)	
	$D_{i,\text{eff}}^L = D_i^L \varepsilon^{L1.5}$	(63)	

[1] Refer to Table 7 for the values of s_i.

Table 7
Values of s_i in the liquid phase mass transport equation.

Ion	s_i^N	s_i^P
V^{2+}	+1	
V^{3+}	-1	
VO^{2+}		+1
VO_2^+		-1
H^+	0	-2

velocity under the ribs is higher at the switchbacks wherein flow through the electrode provides a shorter path than flow though the channels (Fig. 16b) [227,228]. The velocity profiles affect the distribution of reactant concentration, thereby affecting the current density distribution and battery performance.

Unlike Li-ion and lead-acid batteries, the performance of a VRF battery is not solely determined by the distribution of electrochemical properties. A lower pressure drop between the inlet and outlet is also desired to minimize the power required to pump the electrolyte through the cell. This pumping load may be counterproductive if the pressure drop is too high. Serpentine patterns have high pressure drops because the electrolyte flows under the ribs several times [227,228]. In contrast, interdigitated patterns have lower pressure drops than serpentine designs because the electrolyte passes the electrodes only once [227,228]. In both designs, the pressure drop increases greatly with flow rate [227, 228].

4.2.3. Electrochemical properties

The reactant concentration profile depends on the velocity profile. The parallel flow pattern directs the electrolyte down the channels near the inlets, so the reactant concentration is higher in these channels [226, 238]. The interdigitated channel forces electrolyte through the electrodes at a uniform velocity, so the resulting concentration profile is uniform in each channel, and the reaction current is uniform along the channel length (Fig. 17a) [227]. The serpentine flow channel yields a concentration profile that gradually reduces towards the outlet [227]. The reaction current is high near the inlet, and becomes lower through the rest of the electrode (Fig. 17b) [227,228].

Table 8

Kinetics in VRF batteries.

Name	Equation	Ref.
Current density	$$j^{N} = j_0^{N} \left[\frac{c_{V^{2+},s}^{LN}}{c_{V^{2+}}^{LN}} \exp\left(\frac{\alpha_A^{N} \eta^{N} F}{RT} \right) - \frac{c_{V^{3+},s}^{LN}}{c_{V^{3+}}^{LN}} \exp\left(\frac{-\alpha_C^{N} \eta^{N} F}{RT} \right) \right] \quad (64)$$	
	$$j^{P} = j_0^{P} \left[\frac{c_{VO^{2+},s}^{LP}}{c_{VO^{2+}}^{LP}} \exp\left(\frac{\alpha_A^{P} \eta^{P} F}{RT} \right) - \frac{c_{VO_2^+,s}^{LP}}{c_{VO_2^+}^{LP}} \exp\left(\frac{-\alpha_C^{P} \eta^{P} F}{RT} \right) \right] \quad (65)$$	
Overpotential		[237]
	$$\eta = \phi^{S} - \phi^{L} - V_{eq} \quad (66)$$	
Exchange current density		
	$$j_0^{N} = F k_V^{N} \left(c_{V^{2+}}^{LN} \right)^{\alpha_C^{N}} \left(c_{V^{3+}}^{LN} \right)^{\alpha_A^{N}} \quad (67)$$	
	$$j_0^{P} = F k_V^{P} \left(c_{VO^{2+}}^{LP} \right)^{\alpha_C^{P}} \left(c_{VO_2^+}^{LP} \right)^{\alpha_A^{P}} \quad (68)$$	
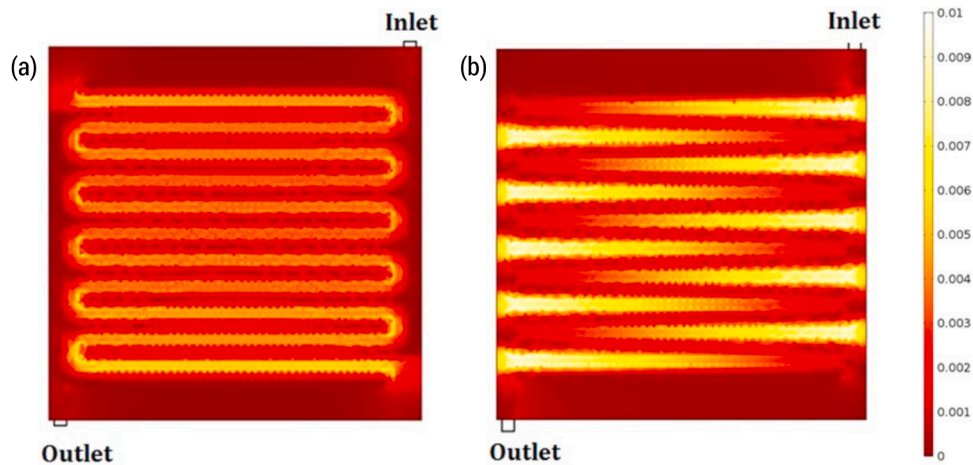
Fig. 16. Electrolyte velocity distributions in the electrode taken halfway through the electrode thickness when using an interdigitated (a) and serpentine (b) flow field. The interdigitated flow field yields uniform velocities along the length of the flow channel, while the serpentine flow fields have higher velocities at the switchbacks. (Fig. from [228])
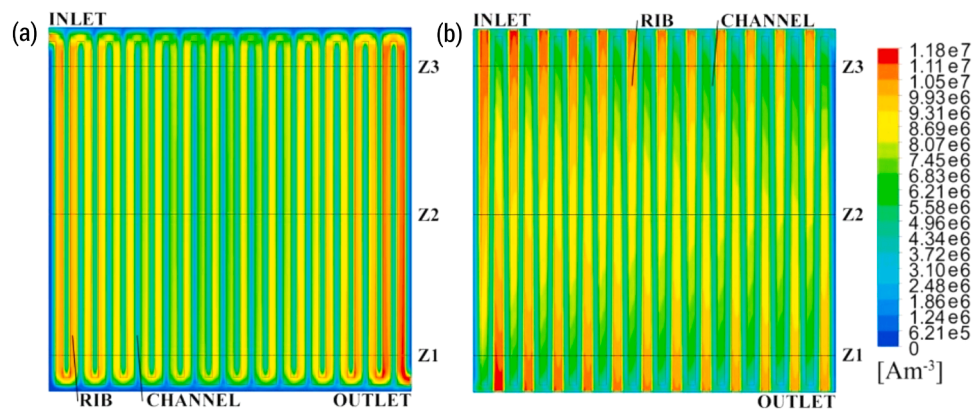
Fig. 17. Reaction current density distributions halfway through the thickness of the positive electrode at 60% SOC when using an interdigitated (a) and serpentine (b) flow field. The interdigitated flow field yields a uniform reaction current density, while the serpentine flow field has a less uniform current density. (Fig. from [227])
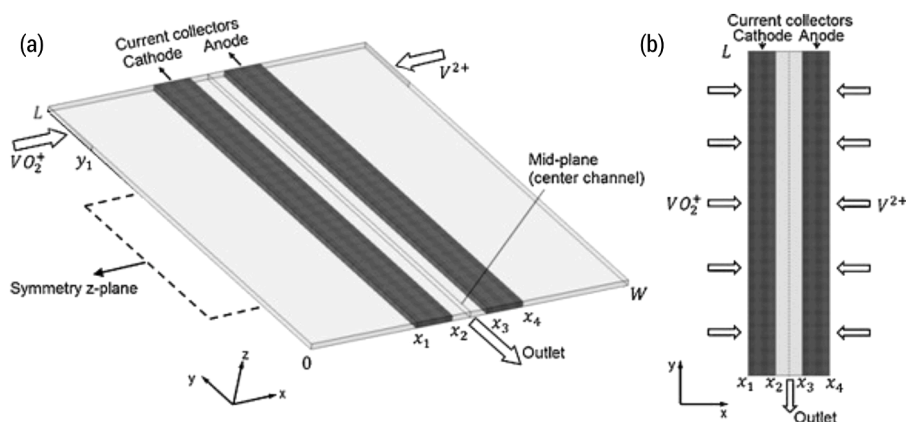
Fig. 18. Schematic diagram of the flow-through microfluidic VRF battery. The anolyte and catholyte pass through the electrodes and meet at the middle. They undergo laminar flow in the middle channel before exiting. (Fig. from [237])

Along the thickness of the battery, the reaction current generally increases with reactant concentration. In flow-through designs, the reactant concentration is highest near the membranes [230]. The reaction current profile is more uniform in the positive electrode due to the higher diffusivity of VO^{2+} and VO_2^+ [236]. If a flow channel is present, then the reaction rate is appreciable near the flow channel [233].

4.2.4. Research trends

Several studies on the multiphysics modeling of VRF batteries have dealt with the optimization of flow fields. For instance, Lee et al. compared serpentine flow fields with different channel widths and flow rates in terms of a power-based efficiency that accounts for overpotentials and pumping losses [239]. Li et al. conducted a similar study for the interdigitated flow field [240]. Chen et al. used topology optimization to design a flow field pattern that maximizes the average concentration of reactants at the surface of the electrode [226]. Yaji et al. also designed flow field patterns via topology optimization to maximize the reaction rate at various porosities and pressure drops [241]. They also developed a framework for reducing the computational cost of topology optimization by coupling low-fidelity and high-fidelity methods [242]. Chen and Kang presented an alternative approach wherein the porosity distribution was optimized instead of flow field design [243], while Tsushima and Suzuki noted that material properties and flow channel geometry must be optimized simultaneously [244].

The simulation of VRF batteries is typically performed with computational fluid dynamics (CFD) software such as Ansys Fluent® [227,233,238,245] and STAR-CCM+® [229,246] due to the presence of moving fluid, although some simulations were also implemented in COMSOL® Multiphysics [226,228,230,247]. The voltage vs. current density curves obtained from simulations and experimental data are generally in agreement, although Messaggi et al. showed that discrepancies arise at larger flow rates and current densities due to the overestimation of the mass transfer coefficient [227]. Multiphysics models also overpredict the pressure drop of serpentine flow channels and underpredict that of interdigitated channels [227,228].

4.3. Extended models

4.3.1. Microfluidic cell

The VRF battery has been redesigned as a microfluidic device to eliminate the membrane, which in turn reduces ohmic losses, as well as manufacturing and maintenance costs [248,249]. Separation of the anolyte and catholyte becomes possible because of laminar flow at the microfluidic scale. Many studies assume a flow-through design wherein the feed anolyte and catholyte pass through a porous electrode then contact each other while flowing in a laminar fashion towards the outlet (Fig. 18). The earliest multiphysics model for this design was proposed

by Krishnamurthy et al. [237], which they then used to conduct a parametric study [250]. Li et al. showed that increasing the electrocatalytic activity in high reaction rate regions can increase its power density [251], while Tanveer and Kim compared various cross-sectional shapes in the mixing region [252]. Ibáñez et al. quantified vanadium crossover under two limiting cases concerning the rate of reaction [248].

Other microfluidic VRF battery designs were also investigated. Li et al. demonstrated a radial design that can have larger sizes without affecting the laminar mixing region, which in turn improves the single-cell power output [249]. Tanveer and Kim studied Y-shaped designs with various cross-sections and tapering [253]. Ouyang et al. compared the flow-through and flow-over designs, and found that the performance of the flow-through design is more stable with regards to its physical orientation (i.e., effect of gravity) [254].

4.3.2. Electrode compression

Contact resistances in VRF batteries result in inactive regions, ohmic losses, and temperature buildups that may damage the battery components [255]. This can be addressed by compressing the electrodes, which eliminates contact resistances while also improving the performance of a VRF battery [256]. Electrode compression reduces porosity and thickness, which decreases ohmic overpotentials [38,257–259]. Too much compression, however, results in increased concentration overpotentials [256,257] and pressure drops [258]. This has prompted several studies on optimizing the compression ratios in flow-through designs. Yue et al. developed a polarization model, which they coupled with a compression model to find the compression ratio with the lowest overpotential [257]. Xiong et al. showed that large compression forces increase the power density, but excessive compression forces should be avoided to prevent mechanical fracture [256]. Park et al. optimized the compression ratios for carbon felt electrodes and found that optimum compression ratios for charge capacity and power are different for energy efficiency [259]. Gurieff et al. introduced an alternative design that varied the compression ratio by placing the membrane at an angle. This increased the limiting current density while reducing the pressure drop [260].

Electrode compression in designs with flow channels has also been studied. This was shown to cause intrusion of the electrode into the flow channels. Kumar et al. developed a correlation between the depth of the intrusion and the compression ratio, which they used to simulate the pressure drop in a serpentine flow channel [261]. Wang et al. modeled the uneven compression of a VRF battery with a serpentine flow field, which was used to find a compression ratio with a uniform concentration distribution and minimum overpotential [262].

4.3.3. Vanadium crossover

Vanadium crossover refers to the permeation of vanadium ions into the membrane and into the opposite half-cell. V^{2+} and V^{3+} from the
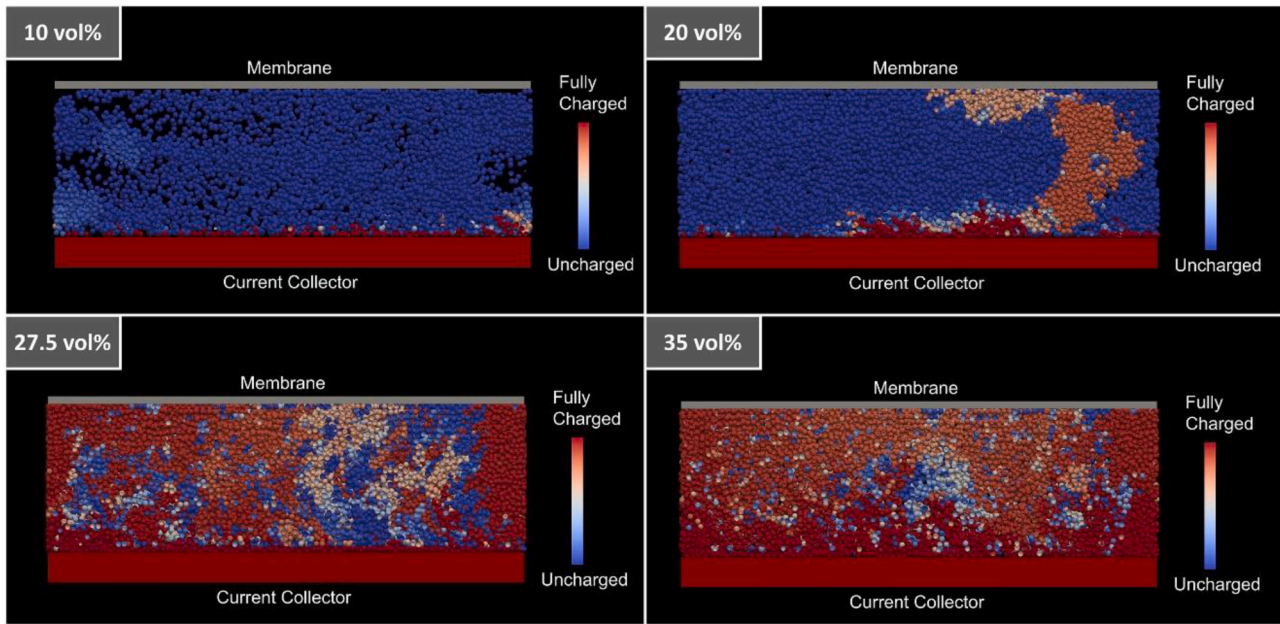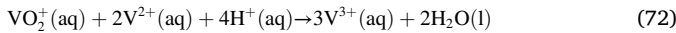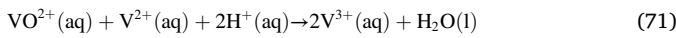
Fig. 19. Lohaus et al. (2020) coupled CFD and DEM to simulate a VRF battery wtih slurry electrodes. At low particle volume fractions (10% and 20%), not all the particles are charged. This result would have been difficult to achieve using a pure CFD approach. (Fig. from [271])

anolyte react with the catholyte (Eqs. 69,70), and VO_2^+ or VO^{2+} from the catholyte react with the anolyte (Eqs. 71,72) [263]. These reactions are irreversible and are responsible for capacity fade in VRF batteries [35,221,235,263,264].

$$V^{2+}(aq) + 2VO_2^+(aq) + 2H^+(aq) \rightarrow 3VO^{2+}(aq) + H_2O(l) \qquad (69)$$

$$V^{3+}(aq) + VO_2^+(aq) \rightarrow 2VO^{2+}(aq) \qquad (70)$$

$$VO^{2+}(aq) + V^{2+}(aq) + 2H^+(aq) \rightarrow 2V^{3+}(aq) + H_2O(l) \qquad (71)$$

$$VO_2^+(aq) + 2V^{2+}(aq) + 4H^+(aq) \rightarrow 3V^{3+}(aq) + 2H_2O(l) \qquad (72)$$

The model developed by Knehr et al. has been widely adopted in vanadium crossover simulations. Instead of restricting the species in the membrane to H^+, this model allows the transport of all ions across the membrane [35]. The membrane is still largely selective to H^+, however, due to the small diffusion coefficients of positively charged vanadium ions and the displacement of negatively charged sulfate ions by the fixed site charges. The side reactions are assumed to occur instantly when an ion reaches the opposite half-cell. This is modeled using the appropriate boundary conditions [35]. Flow in the membrane is described by the Schlogl equation. This accounts for osmosis, which is the flow due to pressure, and electro-osmotic drag, which is the flow of water due to its attraction to ions [35,235]. The volume changes due to water transport were shown by Jeong and Jung to have a notable effect during cycling simulations [235]. Chou et al. analyzed the impact of vanadium crossover on the cell potential and the distribution of concentrations and overpotentials in the electrode [265]. Lei et al. improved the model of Knehr et al. by addressing the discontinuous concentration of HSO_4^- resulting from the electroneutrality assumption [266].

The understanding of vanadium crossover spurred the development of strategies for mitigating capacity fade in VRF batteries. Many of these involved the asymmetric operation or design of the electrodes. For instance, Lu et al. showed that vanadium ion flux from the anolyte to the catholyte is typically larger, so increasing the catholyte concentration can address the flux imbalance and reduce capacity fade [267]. They also demonstrated that starting with a larger positive electrode then compressing both electrodes to the same thickness can greatly reduce capacity fade and improve energy efficiency [268]. Agar et al. classified ion exchange membranes as either diffusion or convection controlled [263] and found that asymmetric charging (i.e., charging current higher than discharging current) can reduce capacity fade, especially when
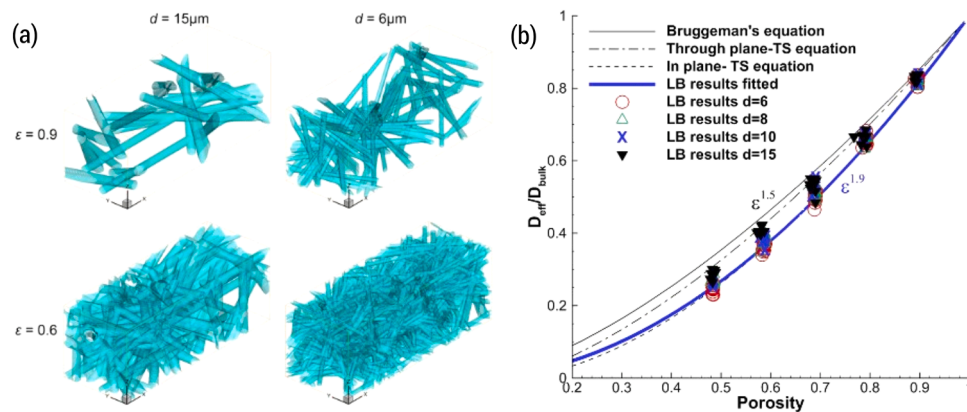

Fig. 20. Chen et al. (2017) performed a pore-level simulation of a VRF battery using the lattice Boltzmann method. Simulations on the reconstructed geometry (a) yielded a correlation between the porosity and effective diffusivity (b). (Fig. from [273])

diffusion controlled membranes are used, albeit at the cost of voltage efficiency [264].

4.4. Outlook

4.4.1. Challenges at the continuum scale

Unlike Li-ion and lead-acid batteries, much work still needs to be done regarding continuum-scale research on VRF batteries. Studies at the continuum scale have optimized the design parameters of Li-ion [9–11] and lead-acid batteries [201] due to their simple geometries. The performance of VRF batteries, however, depends on the complex interaction between hydraulic and electrochemical phenomena. There have been efforts towards optimizing a specified flow field design based on the net power (i.e., accounting for hydraulic and electrochemical losses) [239,240], topology optimization based on concentration or kinetics [226,241,242], and material properties [243], however optimizing these parameters separately may lead to non-optimum designs [244]. The development of a framework that simultaneously optimizes the flow field topology and material properties with respect to the net power is a worthwhile endeavor.

In addition, many studies modeled VRF batteries using the Nernst-Planck equation, which is valid only for dilute solutions. This was likely due to the difficulty of obtaining parameters for Newman's concentrated solution theory, which accounts for the interaction between charged species [23] and the effect of concentration gradients on charge transport [23]. So far, VRF models that have implemented the concentrated solution theory have focused on the membrane [269,270]. Crothers et al. used this to compute performance metrics for the cell [270], although explicit modeling of the electrodes and flow channels has yet to be performed.

Researchers have also recently investigated semisolid electrodes, which are made by suspending the active materials in the electrolyte solution. Lohaus et al. modeled a slurry electrode by coupling CFD for fluid flow with discrete element modeling (DEM) for particle flow [271]. In contrast with results from a pure CFD approach, the inclusion of DEM showed that not all the particles participate in the reaction and that increasing the particle concentration improves battery performance (Fig. 19) [271]. Smith et al. modeled a non-Newtonian fluid electrode [272]. They demonstrated that promoting slip flow reduces the pumping requirements but reduces electrical contact. In contrast, plug flow operation improves electrochemical performance at the cost of higher pumping power [272]. Models regarding this system are still under development.

4.4.2. Material scale to continuum scale

Nevertheless, there have been studies suggesting the integration of VRF multiphysics modeling with research in other length scales. For instance, Chen et al. simulated the reactions in a VRF battery at the pore scale (Fig. 20a), including the gas formation side reactions [273]. They compared their results with empirical correlations used in continuum-scale studies and revealed that the Bruggeman correlation overpredicts effective diffusivities (Fig. 20b) and gas coverage ratios [273]. Sadeghi et al. employed a pore-scale model to show that increasing the porosity increases the hydraulic permeability but decreases the reaction surface area [274]. This signifies a tradeoff between electrochemical and hydraulic properties at the continuum scale. It was also shown that aligning the fibers at the pore scale increases hydraulic permeability and power density [274]. This study was based on the hydrogen-bromine system, but the framework is applicable to VRFs as well. The findings of pore-scale studies should be applied to continuum-scale research as well to advance the design and optimization of VRF batteries.

4.4.3. Continuum scale to system scale

Scaling up the VRF has proven challenging because of the complex interaction of hydraulic and electrochemical phenomena. In addition to the pumping losses present in VRF cells, the formation of VRF stacks introduces shunt currents, which further reduces its energy efficiency [275]. Shunt currents refer to the electrical currents that form between the positive electrode of one cell and the negative electrode of an adjacent cell, which results in self-discharge during charging, discharging, and standby [276]. Considering the scale of the problem, many studies have opted to use simpler models for describing shunt currents, but some have incorporated continuum-scale multiphysics models. Moro et al. introduced an alternative stack topology that puts electrodes of the same polarity next to each other to minimize shunt currents [277]. The individual cells were described via multiphysics models, while the piping system and shunt currents were modeled as equivalent circuits. A continuum-scale 3D model accounting for shunt currents in a VRF stack was developed by Yin et al. [278], although optimization of this system has yet to be performed.

There has also been interest towards the development of reduced-order models. For instance, Vynnycky et al. reduced the 2D flow-through VRF multiphysics model, which contained 11 partial differential equations, into a reduced-order model with only four ordinary differential equations [231]. Sharma et al. demonstrated the reduction of a 2D flow-through VRF multiphysics model into a 0D model. They also identified two dimensionless numbers that determine the applicability

Table 9
Comparison between multiphysics modeling studies.

| Category	Li-ion	Lead-acid	VRF
Electrochemical Model	• concentrated binary electrolyte • negligible electrolyte flow	• concentrated binary electrolyte • Darcy equation for flow in porous media • Navier-Stokes equation or Stokes flow in reservoir	• dilute multicomponent electrolyte • Darcy or Brinkman equation for flow in porous media • Navier-Stokes equation in flow channels
Simulation Tools	• COMSOL Multiphysics® • Dualfoil • LIONSIMBA	• COMSOL Multiphysics®	• COMSOL Multiphysics® • ANSYS Fluent® • STAR-CCM+®
Extended Models	• mechanical stresses, • SEI formation, thermal runaway • silicon negative electrode	• gas evolution • flow battery	• vanadium crossover • electrode compression • microfluidic cell
Continuum-scale	• current collector tab width and placement • battery optimization • comparison between chemistries	• current collector lug placement • grid design • transient effects and control	• battery optimization • concentrated solution theory • slurry electrode
Molecular to Continuum	• physicochemical property estimation	• N/A	• N/A
Material to Continuum	• nanostructure optimization • particle-scale simulation	• nanostructure optimization	• pore-scale simulation
Continuum to Systems	• capacity fade • reduced-order model	• reduced-order model	• stack simulation • reduced-order model
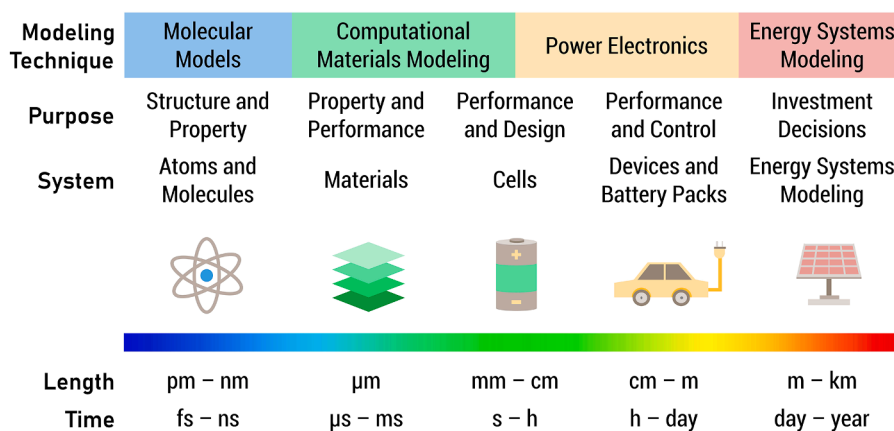
Fig. 21. Interaction of multiphysics modeling with disciplines in other length scales.

of their reduced-order model [234]. Ke et al. introduced an analytical solution for the volumetric flow rate in the porous layer as a function of the inlet flow rate in a serpentine channel [279]. Other model reduction methods, such as machine learning and reduced-order equivalent circuit models, can be applied in future work. This is especially true for reduced-order equivalent circuit models, which have seen extensive use in battery management systems [280,281].

5. Discussion

A comparison between the multiphysics modeling studies of Li-ion, lead-acid, and VRF batteries is shown in Table 9. At the continuum scale, these batteries are described by charge and mass transport equations derived from Newman's porous electrode theory [23] and an electrolyte model. The concentrated solution theory is used in Li-ion [26,70–72] and lead-acid models [29,34,205,206], while the Nernst-Planck equation is often applied in VRF models [226,227,235]. Electrolyte flow may be described by the Darcy equation in porous media [29,232] and the Navier-Stokes equations in free electrolyte [28, 230]. Other flow equations may be considered, but their usage must be justified. These continuum-scale studies have been established in Li-ion [9,11] and lead-acid batteries [201] due to their simple geometries. The performance of these chemistries can be improved by optimizing the current collector placement [11–13,49] and using thinner assemblies [80,86]. This promotes a uniform distribution of electrochemical and thermal properties, which avoids the overutilization of battery materials. As for VRF batteries, the complex interaction between geometry, electrochemistry, and hydraulics makes it difficult to optimize the overall performance of the cell [228,239]. It is for this reason that multiphysics studies on Li-ion and lead-acid batteries have already advanced to address practical applications, while recent work on VRF batteries still focuses mostly on continuum-scale improvements.

Progress in multiphysics modeling has been led by the demands and applications for each chemistry. Li-ion batteries are being increasingly used in electric vehicles and grid balancing. The performance of these batteries can be improved by incorporating silicon electrodes [36,134, 139,144,147,149,282,283] or reducing degradation from SEI formation [112,126,130] and mechanical stresses [81,82,109,110,114,117]. Safety is promoted by planning strategies against thermal runaway [32, 70,73,158,160,168,170] and predicting battery behavior during ultra-fast discharge [164–166]. Lead-acid batteries are deployed in uninterruptable power systems. Side reactions in these systems can be avoided by predicting gas evolution [33,198,206] or by completely revising the battery design [37,214–216]. VRF batteries are utilized in large-scale energy storage applications, however, recent efforts are still directed towards cell-level improvements, as discussed earlier. Capacity loss is minimized by avoiding vanadium crossover [35,221,235,263,

264,269,270], while efficiency is increased by optimizing the cell compression [38,255,256,261,262]. The battery has also been redesigned as a microfluidic cell [237,251,284] or by using semisolid electrodes [271,272] to manage the interaction between electrochemical and hydraulic effects.

As multiphysics modeling studies delve deeper into the practical applications of each chemistry, it is inevitable that these models will bridge into different length scales (Fig. 21). Device-level applications such as Li-ion battery packs for electric vehicles and energy storage have been investigated with multiphysics modeling. These couple cell-level models with external considerations, such as the temperature distribution [15,16] and capacity fade due to repeated cycling [125]. System-level research can greatly benefit from reduced-order battery models. The multiphysics models of Li-ion [188] and lead-acid [41,219] batteries were reduced using machine learning techniques, while a lead-acid model was regressed into an equivalent circuit model [42]. The latter technique may prove useful for energy systems modeling software, such as HOMER Pro®. These often use simplified models [193] that may contain circuit-based models [285]. Simple models are necessary for this application as the battery model is evaluated repeatedly in the simulation of an energy system [192,286].

The design and improvement of batteries have also been investigated with multiphysics modeling. Traditionally, this has been done by developing continuum-scale models and then optimizing parameters such as thickness and tab placement. Recent work, however, has brought this paradigm to nanostructured materials in Li-ion [175] and lead-acid batteries [209]. Models have been developed for these nanostructures, which can be optimized in future work. This holds the key to deploying silicon negative electrodes in Li-ion batteries, as silicon nanostructures were shown to mitigate the effects of volumetric expansion [139,144]. Small-scale studies may also improve existing multiphysics models. Particle-scale simulations in Li-ion batteries that incorporate realistic geometries [110,177] can provide more realistic LII and LAM degradation models [112,126,130]. Pore-scale studies in VRF batteries also showed that material-level improvements may yield improved electrochemical performance and reduced pressure drop [274]. Another pore-scale VRF model suggested several corrections to empirical models used in continuum-scale modeling [273]. Molecular-scale techniques such as density functional theory and kinetic Monte Carlo simulations in Li-ion batteries have been shown to predict continuum-scale transport parameters [39,171,172] and produce SEI formation models from first principles [40,131–133].

6. Conclusions

In this review, we discussed advances on the multiphysics modeling of Li-ion, lead-acid, and VRF batteries. Over the past few decades, the

electrochemical models of these chemistries have drastically improved. Further modifications are necessary only for specialized applications, such as the modeling of mechanical effects and side reactions. Recent advances in battery research have therefore focused on introducing new concepts instead of refining existing models. For example, the demand for high energy density batteries has motivated the study of Li-ion systems with silicon electrodes. Some systems were also redesigned, such as the lead-acid flow battery and VRF microfluidic cell. Nevertheless, models have been successfully developed for these novel applications.

Future work on multiphysics modeling should focus on its integration with disciplines from various length scales. The design of materials and nanostructures can be optimized with respect to the overall cell performance. Molecular-scale techniques can be employed in the determination of continuum-scale properties or the development of new multiphysics models. The design and management of battery packs for electric vehicles and grid-balancing applications can be improved by considering particle-scale and cell-scale effects. Lastly, energy systems modeling can utilize reduced-order multiphysics models. With the increasing power of computational technology, multiphysics modeling will be applicable to these endeavors and will still be the leading approach to investigatory battery research.

Declaration of Competing Interest

The authors declare that they have no known competing financial interests or personal relationships that could have appeared to influence the work reported in this paper.

Acknowledgement

References

[1] S. Chaurasiya, B. Singh, A G2V/V2G off-board fast charger for charging of lithium-ion based electric vehicles, in: Proc. - 2019 IEEE Int. Conf. Environ. Electr. Eng. 2019 IEEE Ind. Commer. Power Syst. Eur. EEEIC/CPS Eur. 2019, IEEE, 2019.

[2] O. Schmidt, A. Hawkes, A. Gambhir, I. Staffell, The future cost of electrical energy storage based on experience rates, Nat. Energy. 2 (8) (2017), 17110, https://doi.org/10.1038/nenergy.2017.110.

[3] O Schmidt, S Melchior, A Hawkes, I. Staffell, Projecting the future levelized cost of electricity storage technologies, Joule 3 (1) (2019) 81–100, https://doi.org/10.1016/j.joule.2018.12.008.

[4] A.H. Fathima, K. Palanismay, Modeling and operation of a vanadium redox flow battery for PV applications, Energy Procedia 117 (2017) 607–614, https://doi.org/10.1016/j.egypro.2017.05.157.

[5] Y. Zhang, J. Zhao, P. Wang, M. Skyllas-Kazacos, B. Xiong, R. Badrinarayanan, A comprehensive equivalent circuit model of all-vanadium redox flow battery for power system analysis, J. Power Sources 290 (2015) 14–24, https://doi.org/10.1016/j.jpowsour.2015.04.169.

[6] C. Caceres, A. Ortega, L. Silva-Llanca, G.F. Jones, N. Sapia, Thermal and exergy analysis in UPS and battery rooms by numerical simulations, in: Proc. 17th Intersoc. Conf. Therm. Thermomechanical Phenom. Electron. Syst. ITherm 2018, IEEE, 2018, pp. 521–529.

[7] Suwarno, Witantyo Suwarno, Irawan, Effect of depth of discharge on morphology and size of sulfate particles in VRLA battery electrodes, in: AIP Conf. Proc. 2018 1983, AIP Publishing, 2018, 050015.

[8] K. Khodadadi Sadabadi, P. Ramesh, P. Tulpule, G. Rizzoni, Design and calibration of a semi-empirical model for capturing dominant aging mechanisms of a PbA battery, J. Energy Storage 24 (May) (2019), 100789, https://doi.org/10.1016/j.est.2019.100789.

[9] E. Hosseinzadeh, J. Marco, P. Jennings, Electrochemical-thermal modelling and optimisation of lithium-ion battery design parameters using analysis of variance, Energies 10 (9) (2017), https://doi.org/10.3390/en10091278.

[10] H. Li, C. Liu, A. Saini, Y. Wang, H. Jiang, T. Yang, et al., Coupling multi-physics simulation and response surface methodology for the thermal optimization of ternary prismatic lithium-ion battery, J. Power Sources 438 (July) (2019), 226974, https://doi.org/10.1016/j.jpowsour.2019.226974.

[11] W. Mei, H. Chen, J. Sun, Q. Wang, Numerical study on tab dimension optimization of lithium-ion battery from the thermal safety perspective, Appl. Therm. Eng. 142 (2018) 148–165, https://doi.org/10.1016/j.applthermaleng.2018.06.075.

[12] A. Alagheband, M. Azimi, H. Hashemi, M. Kalani, D. Nakhaie, Optimization of grid configuration by investigating its effect on positive plate of lead-acid batteries via numerical modeling, J. Energy Storage 12 (2017) 202–214, https://doi.org/10.1016/j.est.2017.04.012.

[13] D. Nakhaie, P.H. Benhangi, A. Alfantazi, A. Davoodi, The effect of grid configurations on potential and current density distributions in positive plate of lead-acid battery via numerical modeling, Electrochim. Acta 115 (2014) 189–196, https://doi.org/10.1016/j.electacta.2013.10.152.

[14] M.R. Khan, S.K. Kaer, Multiphysics based thermal modeling of a pouch lithium-ion battery cell for the development of pack level thermal management system, in: 2016 11th Int. Conf. Ecol. Veh. Renew. Energies, EVER 2016, IEEE, 2016.

[15] Q. Xia, Z. Wang, Y. Ren, B. Sun, D. Yang, Q. Feng, A reliability design method for a lithium-ion battery pack considering the thermal disequilibrium in electric vehicles, J. Power Sources 386 (February) (2018) 10–20, https://doi.org/10.1016/j.jpowsour.2018.03.036.

[16] Q. Xia, D. Yang, Z. Wang, Y. Ren, B. Sun, Q. Feng, et al., Multiphysical modeling for life analysis of lithium-ion battery pack in electric vehicles, Renew. Sustain. Energy Rev. 131 (May) (2020), 109993, https://doi.org/10.1016/j.rser.2020.109993.

[17] Q. Xia, Z. Wang, Y. Ren, D. Yang, B. Sun, Q. Feng, et al., Performance reliability analysis and optimization of lithium-ion battery packs based on multiphysics simulation and response surface methodology, J. Power Sources 490 (February) (2021), 229567, https://doi.org/10.1016/j.jpowsour.2021.229567.

[18] J. Xu, C. Lan, Y. Qiao, Y. Ma, Prevent thermal runaway of lithium-ion batteries with minichannel cooling, Appl. Therm. Eng. 110 (2017) 883–890, https://doi.org/10.1016/j.applthermaleng.2016.08.151.

[19] W. Zhang, Z. Liang, X. Yin, G. Ling, Avoiding thermal runaway propagation of lithium-ion battery modules by using hybrid phase change material and liquid cooling, Appl. Therm. Eng. 184 (October 2020) (2021), 116380, https://doi.org/10.1016/j.applthermaleng.2020.116380.

[20] F. Larsson, J. Anderson, P. Andersson, B. Mellander, Thermal modelling of cell-to-cell fire propagation and cascading thermal runaway failure effects for lithium-ion battery cells and modules using fire walls, J. Electrochem. Soc. 163 (14) (2016) A2854–A2865, https://doi.org/10.1149/2.0131614jes.

[21] Q. Li, C. Yang, S. Santhanagopalan, K. Smith, J. Lamb, L.A. Steele, et al., Numerical investigation of thermal runaway mitigation through a passive thermal management system, J. Power Sources 429 (March) (2019) 80–88, https://doi.org/10.1016/j.jpowsour.2019.04.091.

[22] X. Feng, L. Lu, M. Ouyang, J. Li, X. He, A 3D thermal runaway propagation model for a large format lithium ion battery module, Energy 115 (2016) 194–208, https://doi.org/10.1016/j.energy.2016.08.094.

[23] J. Newman, K.E. Thomas, Electrochemical Systems. Electrochemical Systems, 3rd ed., John Wiley & Sons, New Jersey, 2004.

[24] T. Fuller, M. Doyle, J. Newman, Simulation and optimization of the dual lithium ion insertion cell, J. Electrochem. Soc. 141 (1) (1994), https://doi.org/10.1149/1.2054684.

[25] M. Doyle, J. Newman, Comparison of modeling predictions with experimental data from plastic lithium ion cells, J. Electrochem. Soc. 143 (6) (1996) 1890, https://doi.org/10.1149/1.1836921.

[26] W.H. Tiedemann, J. Newman, Battery design and optimization, The Electrochemical Society Softbound Proceedings Series, Princeton, New Jersey, 1979.

[27] H. Gu, T.V. Nguyen, R.E. White, A mathematical model of a lead-acid cell: Discharge, rest, and charge, J. Electrochem. Soc. 134 (12) (1987) 2953, https://doi.org/10.1149/1.2100322.

[28] F. Alavyoon, A. Eklund, F.H. Bark, R.I. Karlsson, D. Simonsson, Theoretical and experimental studies of free convection and stratification of electrolyte in a lead-acid refining cell during recharge, Electrochim. Acta 36 (14) (1991) 2153–2164, https://doi.org/10.1016/0013-4686(91)85224-U.

[29] W.B. Gu, C.Y. Wang, B.Y. Liaw, Numerical modeling of coupled electrochemical and transport processes in lead-acid batteries, J. Electrochem. Soc. 144 (6) (1997) 2053, https://doi.org/10.1149/1.1837741.

[30] A.A. Shah, M.J. Watt-Smith, F.C. Walsh, A dynamic performance model for redox-flow batteries involving soluble species, Electrochim. Acta 53 (27) (2008) 8087–8100, https://doi.org/10.1016/j.electacta.2008.05.067.

[31] H. Al-Fetlawi, A.A. Shah, F.C. Walsh, Non-isothermal modelling of the all-vanadium redox flow battery, Electrochim. Acta 55 (1) (2009) 78–89, https://doi.org/10.1016/j.electacta.2009.08.009.

[32] A. Melcher, C. Ziebert, M. Rohde, H.J. Seifert, Modeling and simulation of the thermal runaway behavior of cylindrical Li-ion cells-computing of critical parameters, Energies 9 (4) (2016), https://doi.org/10.3390/en9040292.

[33] W.B. Gu, G.Q. Wang, C.Y. Wang, Modeling the overcharge process of VRLA batteries, J. Power Sources 108 (1–2) (2002) 174–184, https://doi.org/10.1016/S0378-7753(02)00043-5.

[34] Rensburg A.J. Van, Multi-scale model of a valve-regulated lead-acid battery with electromotive force characterization to investigate irreversible sulphation, North-West University Yunibersity Ya Bokone-Bophirima Noordwes-Universiteit, 2015.

[35] K.W. Knehr, E. Agar, C.R. Dennison, A.R. Kalidindi, E.C. Kumbur, A transient vanadium flow battery model incorporating vanadium crossover and water transport through the membrane, J. Electrochem. Soc. 159 (9) (2012) A1446–A1459.

[36] A.F. Bower, P.R. Guduru, V.A. Sethuraman, A finite strain model of stress, diffusion, plastic flow, and electrochemical reactions in a lithium-ion half-cell, J. Mech. Phys. Solids 59 (4) (2011) 804–828, https://doi.org/10.1016/j.jmps.2011.01.003.

[37] A.A. Shah, X. Li, R.G.A. Wills, F.C. Walsh, A mathematical model for the soluble lead-acid flow battery, J. Electrochem. Soc. 157 (5) (2010) A589–A599, https://doi.org/10.1149/1.3328520.

[38] K. Oh, S. Won, H. Ju, Numerical study of the effects of carbon felt electrode compression in all-vanadium redox flow batteries, Electrochim. Acta 181 (2015) 13–23, https://doi.org/10.1016/j.electacta.2015.02.212.

[39] F. Hanke, N. Modrow, R.L.C. Akkermans, I. Korotkin, F.C. Mocanu, V.A. Neufeld, M. Veit, Multi-scale electrolyte transport simulations for lithium ion batteries, J. Electrochem. Soc. 167 (1) (2020), 013522, https://doi.org/10.1149/2.0222001jes.

[40] F. Röder, R.D. Braatz, U. Krewer, Multi-scale modeling of solid electrolyte interface formation in lithium-ion batteries, Comput. Aided Chem. Eng. 38 (2016) 157–162, https://doi.org/10.1016/B978-0-444-63428-3.50031-X.

[41] A.A. Shahbazi, V. Esfahanian, Reduced-order modeling of lead-acid battery using cluster analysis and orthogonal cluster analysis method, Int. J. Energy Res. 43 (13) (2019) 6779–6798, https://doi.org/10.1002/er.4645.

[42] M. Shi, J. Yuan, L. Dong, D. Zhang, A. Li, J. Zhang, Combining physicochemical model with the equivalent circuit model for performance prediction and optimization of lead-acid batteries, Electrochim. Acta 353 (2020), 136567, https://doi.org/10.1016/j.electacta.2020.136567.

[43] Z.P. Cano, D. Banham, S. Ye, A. Hintennach, J. Lu, M. Fowler, et al., Batteries and fuel cells for emerging electric vehicle markets, Nat. Energy 3 (4) (2018) 279–289, https://doi.org/10.1038/s41560-018-0108-1.

[44] A.I. Stan, M. Swierczynski, D.I. Stroe, R. Teodorescu, S.J. Andreasen, Lithium ion battery chemistries from renewable energy storage to automotive and back-up power applications - An overview, in: 2014 Int. Conf. Optim. Electr. Electron. Equipment, OPTIM 2014, IEEE, 2014, pp. 713–720.

[45] P. Peng, F. Jiang, Thermal safety of lithium-ion batteries with various cathode materials: A numerical study, Int. J. Heat. Mass. Transf. 103 (2016) 1008–1016, https://doi.org/10.1016/j.ijheatmasstransfer.2016.07.088.

[46] A.V. Potapenkoa, S.A. Kirillov, Lithium manganese spinel materials for high-rate electrochemical applications, J. Energy Chem. 23 (5) (2014) 543–558, https://doi.org/10.1016/S2095-4956(14)60184-4.

[47] X. Chen, W. Shen, T.T. Vo, Z. Cao, A. Kapoor, An overview of lithium-ion batteries for electric vehicles, 10th Int. Power Energy Conf. IPEC (2012) 230–235, https://doi.org/10.1109/ASSCC.2012.6523269, 2012.

[48] T. Kim, W. Song, D.Y. Son, L.K. Ono, Y. Qi, Lithium-ion batteries: outlook on present, future, and hybridized technologies, J. Mater. Chem. A 7 (7) (2019) 2942–2964, https://doi.org/10.1039/C8TA10513H.

[49] A. Samba, N. Omar, H. Gualous, O. Capron, P. Van Den Bossche, J. Van Mierlo, Impact of tab location on large format lithium-ion pouch cell based on fully coupled tree-dimensional electrochemical-thermal modeling, Electrochim. Acta 147 (2014) 319–329, https://doi.org/10.1016/j.electacta.2014.08.115.

[50] J. Lu, Z. Chen, F. Pan, Y. Cui, K. Amine, High-performance anode materials for rechargeable lithium-ion batteries, Electrochem. Energy Rev. 1 (1) (2018) 35–53, https://doi.org/10.1007/s41918-018-0001-4.

[51] N. Nadkarni, T. Zhou, D. Fraggedakis, T. Gao, M.Z. Bazant, Modeling the metal–insulator phase transition in Li_xCoO_2 for energy and information storage, Adv. Funct. Mater. 29 (40) (2019), 1902821, https://doi.org/10.1002/adfm.201902821.

[52] C. Bubulinca, I. Sapurina, N.E. Kazantseva, J. Vilčáková, Q. Cheng, P. Sáha, Fabrication of a flexible binder-free lithium manganese oxide cathode for secondary Li - Ion batteries, J. Phys. Chem. Solids 137 (2020), 109222, https://doi.org/10.1016/j.jpcs.2019.109222.

[53] Z. Li, X. Feng, L. Mi, J. Zheng, X. Chen, W. Chen, Hierarchical porous onion-shaped $LiMn_2O_4$ as ultrahigh-rate cathode material for lithium ion batteries, Nano Res. 11 (8) (2018) 4038–4048, https://doi.org/10.1007/s12274-018-1986-z.

[54] E. Flores, N. Vonrüti, P. Novák, U. Aschauer, E.J Berg, Elucidation of $Li_xNi_{0.8}Co_{0.15}Al_{0.05}O_2$ redox chemistry by operando Raman spectroscopy, Chem. Mater. 30 (14) (2018) 4694–4703, https://doi.org/10.1021/acs.chemmater.8b01384.

[55] S.T. Myung, F. Maglia, K.J. Park, C.S. Yoon, P. Lamp, S.J. Kim, et al., Nickel-rich layered cathode materials for automotive lithium-ion batteries: achievements and perspectives, ACS Energy Lett. 2 (1) (2017) 196–223, https://doi.org/10.1021/acsenergylett.6b00594.

[56] A.K. Haridas, Q.A. Nguyen, B.F. Song, R. Blaser, S.L. Biswal, ALD-Modified $LiNi_{0.33}Mn_{0.33}Co_{0.33}O_2$ paired with macroporous silicon for lithium-ion batteries: An investigation on lithium trapping, resistance rise, and cycle-life performance, ACS Appl. Energy Mater. 3 (1) (2020) 456–468, https://doi.org/10.1021/acsaem.9b01728.

[57] R. Tatara, Y. Yu, P. Karayaylali, A.K. Chan, Y. Zhang, R. Jung, et al., Enhanced cycling performance of Ni-rich positive electrodes (NMC) in Li-Ion batteries by reducing electrolyte free-solvent activity, ACS Appl. Mater. Interfaces 11 (38) (2019) 34973–34988, https://doi.org/10.1021/acsami.9b11942.

[58] M. Reichert, J. Haetge, D. Berghus, C. Wendt, V. Meier, U. Rodehorst, et al., Lithium cell nail penetration safety experiments under adiabatic conditions, ECS Trans. 61 (27) (2014) 87–103, https://doi.org/10.1149/06127.0087ecst.

[59] N. Delaporte, M.L. Trudeau, D. Bélanger, K. Zaghib, Protection of $LiFePO_4$ against moisture, Materials 13 (942) (2020), https://doi.org/10.3390/ma13040942.

[60] Y. Deng, S. Wang, Y. Zhou, Y. Qian, X. Qin, G. Chen, The enhancement of rate and cycle performance of $LiMn_2O_4$ at elevated temperatures by the synergistic roles of porous structure and dual-cation doping, J. Appl. Electrochem. 48 (10) (2018) 1083–1094, https://doi.org/10.1007/s10800-018-1200-8.

[61] W.J. Huang, J.Y. Zheng, J.J. Liu, R.M. Yang, F.X. Cheng, H.B. Suo, et al., Boosting rate performance of $LiNi_{0.8}Co_{0.15}Al_{0.05}O_2$ cathode by simply mixing lithium iron phosphate, J. Alloys Compd. 827 (2020), 154296, https://doi.org/10.1016/j.jallcom.2020.154296.

[62] X. Lu, N. Zhang, M. Jahn, W. Pfleging, Improved capacity retention of SiO_2-coated $LiNi_{0.6}Mn_{0.2}Co_{0.2}O_2$ cathode material for lithium-ion batteries, Appl. Sci. 9 (2019) 3671, https://doi.org/10.3390/app9183671.

[63] E. Lee, R.A. Salgado, B. Lee, A.V. Sumant, T. Rajh, C. Johnson, A.A. Balandin, E. V. Shevchenko, Design of lithium cobalt oxide electrodes with high thermal conductivity and electrochemical performance using carbon nanotubes and diamond particles, Carbon 129 (2018) 702–710, https://doi.org/10.1016/j.carbon.2017.12.061.

[64] M. Wang, M. Tang, S. Chen, H. Ci, K. Wang, L. Shi, L. Lin, H. Ren, J. Shan, P. Gao, Z. Liu, H. Peng, Graphene-armored aluminum foil with enhanced anticorrosion performance as current collectors for lithium-ion battery, Adv. Mater. 29 (47) (2017), https://doi.org/10.1002/adma.201703882.

[65] W. Honggowiranto, E. Kartini, Rofika RNS Sudaryanto, R.N.S. Rofika, E. Hutamaningtyas, A. Subhan, A. Sudjatno, et al., Improving performance of $LiFePO_4$ by addition of carbon nano tube for lithium ion battery, IOP Conf. Ser. Mater. Sci. Eng 553 (1) (2019), 012060, https://doi.org/10.1088/1757-899X/553/1/012060.

[66] F. Diaz, Y. Wang, T. Moorthy, B. Friedrich, Degradation mechanism of nickel-cobalt-aluminum (NCA) cathode material from spent lithium-ion batteries in microwave-assisted pyrolysis, Metals 8 (8) (2018) 565, https://doi.org/10.3390/met8080565.

[67] P. Teichert, G.G. Eshetu, H. Jahnke, E. Figgemeier, Degradation and aging routes of Ni-rich cathode based Li-ion batteries, Batteries 6 (1) (2020) 8, https://doi.org/10.3390/batteries6010008.

[68] F. Bahiraei, M. Ghalkhani, A. Fartaj, G.A. Nazri, A pseudo 3D electrochemical-thermal modeling and analysis of a lithium-ion battery for electric vehicle thermal management applications, Appl. Therm. Eng. 125 (2017) 904–918, https://doi.org/10.1016/j.applthermaleng.2017.07.060.

[69] C.Y. Li, Z.Q. Tian, Y. Yu, C. Wang, Y. Zhang, S.Y. Zheng, et al., Surface changes of $LiNi_yMn_yCo_{1-x-y}O_2$ in Li-Ion batteries using in situ surface-enhanced Raman spectroscopy, J. Phys. Chem. C 124 (7) (2020) 4024–4031, https://doi.org/10.1021/acs.jpcc.9b11677.

[70] L. Zhang, P. Zhao, M. Xu, X. Wang, Computational identification of the safety regime of Li-ion battery thermal runaway, Appl. Energy 261 (October 2019) (2020), 114440, https://doi.org/10.1016/j.apenergy.2019.114440.

[71] M. Doyle, J. Newman, The use of mathematical modeling in the design of lithium/polymer battery systems, Electrochim. Acta 40 (13–14) (1995) 2191–2196, https://doi.org/10.1016/0013-4686(95)00162-8.

[72] J. Li, Y. Cheng, L. Ai, M. Jia, S. Du, B. Yin, et al., 3D simulation on the internal distributed properties of lithium-ion battery with planar tabbed configuration, J. Power Sources 293 (2015) 993–1005, https://doi.org/10.1016/j.jpowsour.2015.06.034.

[73] A. Rheinfeld, J. Sturm, A. Frank, S. Kosch, S.V. Erhard, A. Jossen, Impact of cell size and format on external short circuit behavior of lithium-ion cells at varying cooling conditions: Modeling and simulation, J. Electrochem. Soc. 167 (1) (2020), 013511, https://doi.org/10.1149/2.0112001JES.

[74] G.G. Botte, V.R. Subramanian, R.E. White, Mathematical modeling of secondary lithium batteries, Electrochim. Acta 45 (15–16) (2000) 2595–2609, https://doi.org/10.1016/S0013-4686(00)00340-6.

[75] J. Newman, K.E. Thomas, H. Hafezi, D.R. Wheeler, Modeling of lithium-ion batteries, J. Power Sources 119–121 (2003) 838–843, https://doi.org/10.1016/S0378-7753(03)00282-9.

[76] D. Bernardi, E. Pawlikowski, J. Newman, A general energy balance for battery systems, J. Electrochem. Soc. 132 (5) (1985), https://doi.org/10.1149/1.2113792.

[77] C. Ziebert, A. Melcher, B. Lei, W. Zhao, M. Rohde, H.J. Seifert, Electrochemical-thermal characterization and thermal modeling for batteries, Emerging Nanotechnologies in Rechargeable Energy Storage Systems (2017) 195–229, https://doi.org/10.1016/B978-0-323-42977-1/00006-6.

[78] S. Allu, S. Kalnaus, W. Elwasif, S. Simunovic, J.A. Turner, S. Pannala, A new open computational framework for highly-resolved coupled three-dimensional multiphysics simulations of Li-ion cells, J. Power Sources 246 (2014) 876–886, https://doi.org/10.1016/j.jpowsour.2013.08.040.

[79] P. Vyroubal, J. Maxa, T. Kazda, J. Vondrak, Computational modeling of lithium ion battery, ECS Trans. 63 (1) (2014) 99–110, https://doi.org/10.1149/06301.0099ecst.

[80] E. Hosseinzadeh, J. Marco, P. Jennings, The impact of multi-layered porosity distribution on the performance of a lithium ion battery, Appl. Math. Model. 61 (2018) 107–123, https://doi.org/10.1016/j.apm.2018.04.001.

[81] S. Kim, H.Y.S. Huang, Mechanical stresses at the cathode-electrolyte interface in lithium-ion batteries, J. Mater. Res. 31 (22) (2016) 3506–3512, https://doi.org/10.1557/jmr.2016.373.

[82] W. Mei, Q. Duan, P. Qin, J. Xu, Q. Wang, J. Sun, A three-dimensional electrochemical-mechanical model at the particle level for liithium-ion battery, J. Electrochem. Soc. 166 (14) (2019) A3319–A3331, https://doi.org/10.1149/2.0741914jes.

[83] M. Ghalkhani, F. Bahiraei, G.A. Nazri, M. Saif, Electrochemical–thermal model of pouch-type lithium-ion batteries, Electrochim. Acta 247 (2017) 569–587, https://doi.org/10.1016/j.electacta.2017.06.164.

[84] Y. Huang, H. Lai, Effects of discharge rate on electrochemical and thermal characteristics of LiFePO4/graphite battery, Appl. Therm. Eng. 157 (2019), 113744, https://doi.org/10.1016/j.applthermaleng.2019.113744.

[85] J. Li, Y. Cheng, M. Jia, Y. Tang, Y. Lin, Z. Zhang, et al., An electrochemical-thermal model based on dynamic responses for lithium iron phosphate battery, J. Power Sources 255 (2014) 130–143, https://doi.org/10.1016/j.jpowsour.2014.01.007.

[86] R. Zhao, J. Liu, J. Gu, The effects of electrode thickness on the electrochemical and thermal characteristics of lithium ion battery, Appl. Energy 139 (2015) 220–229, https://doi.org/10.1016/j.apenergy.2014.11.051.

[87] A. Nazari, S. Farhad, Heat generation in lithium-ion batteries with different nominal capacities and chemistries, Appl. Therm. Eng. 125 (2017) 1501–1517, https://doi.org/10.1016/j.applthermaleng.2017.07.126.

[88] H. Kwon, H. Park, Numerical simulation of prismatic lithium-ion battery life cycles under a wide range of temperature, Int. J. Precis. Eng. Manuf. - Green Technol. 6 (1) (2019) 63–73, https://doi.org/10.1007/s40684-019-00034-3.

[89] G. Zheng, W. Zhang, X. Huang, Lithium-ion battery electrochemical-thermal model using various materials as cathode material: A simulation study, ChemistrySelect 3 (41) (2018) 11573–11578, https://doi.org/10.1002/slct.201802556.

[90] H.H. Huang, H.Y. Chen, K.C. Liao, H.T. Young, C.F. Lee, J.Y. Tien, Thermal-electrochemical coupled simulations for cell-to-cell imbalances in lithium-iron-phosphate based battery packs, Appl. Therm. Eng. 123 (2017) 584–591, https://doi.org/10.1016/j.applthermaleng.2017.05.105.

[91] M. Xu, Z. Zhang, X. Wang, L. Jia, L. Yang, Two-dimensional electrochemical-thermal coupled modeling of cylindrical LiFePO4 batteries, J. Power Sources 256 (2014) 233–243, https://doi.org/10.1016/j.jpowsour.2014.01.070.

[92] M. Xu, Z. Zhang, X. Wang, L. Jia, L. Yang, A pseudo three-dimensional electrochemical-thermal model of a prismatic LiFePO4 battery during discharge process, Energy 80 (2015) 303–317, https://doi.org/10.1016/j.energy.2014.11.073.

[93] L. Zhang, C. Lyu, G. Hinds, L. Wang, W. Luo, J. Zheng, et al., Parameter sensitivity analysis of cylindrical LiFePO4 battery performance using multi-physics modeling, J. Electrochem. Soc. 161 (5) (2014) A762–A776, https://doi.org/10.1149/2.048405jes.

[94] L. Zhang, L. Wang, C. Lyu, J. Zheng, F. Li, Multi-physics modeling of lithium-ion batteries and charging optimization, in: Proc. 2014 Progn. Syst. Heal. Manag. Conf. PHM 2014, IEEE, 2014, pp. 391–400.

[95] F. Bahiraei, A. Fartaj, G.A. Nazri, Electrochemical-thermal modeling to evaluate active thermal management of a lithium-ion battery module, Electrochim. Acta 254 (2017) 59–71, https://doi.org/10.1016/j.electacta.2017.09.084.

[96] G.H. Kim, K. Smith, K.J. Lee, S. Santhanagopalan, A. Pesaran, Multi-domain modeling of lithium-ion batteries encompassing multi-physics in varied length scales, J. Electrochem. Soc. 158 (8) (2011) A955, https://doi.org/10.1149/1.3597614.

[97] T. Dong, P. Peng, F. Jiang, Numerical modeling and analysis of the thermal behavior of NCM lithium-ion batteries subjected to very high C-rate discharge/charge operations, Int. J. Heat. Mass. Transf. 117 (2018) 261–272, https://doi.org/10.1016/j.ijheatmasstransfer.2017.10.024.

[98] S. Kosch, Y. Zhao, J. Sturm, J. Schuster, G. Mulder, E. Ayerbe, et al., A computationally efficient multi-scale model for lithium-ion cells, J. Electrochem. Soc. 165 (10) (2018) A2374–A2388, https://doi.org/10.1149/2.1241810jes.

[99] N. Lin, X. Xie, R. Schenkendorf, U. Krewer, Efficient global sensitivity analysis of 3D multiphysics model for Li-ion batteries, J. Electrochem. Soc. 165 (7) (2018) A1169–A1183, https://doi.org/10.1149/2.1301805jes/meta.

[100] P. Lyu, Y. Huo, Z. Qu, Z. Rao, Investigation on the thermal behavior of Ni-rich NMC lithium ion battery for energy storage, Appl. Therm. Eng. 166 (May 2019) (2020), 114749, https://doi.org/10.1016/j.applthermaleng.2019.114749.

[101] W. Mei, H. Chen, J. Sun, Q. Wang, The effect of electrode design parameters on battery performance and optimization of electrode thickness based on the electrochemical-thermal coupling model, Sustain. Energy Fuels 3 (1) (2019) 148–165, https://doi.org/10.1039/C8SE00503F.

[102] W. Mei, C. Liang, J. Sun, Q. Wang, Three-dimensional layered electrochemical-thermal model for a lithium-ion pouch cell, Int. J. Energy Res. 44 (11) (2020) 8919–8935, https://doi.org/10.1002/er.5601.

[103] P.R. Nileshwar, A. McGordon, T.R. Ashwin, D. Greenwood, Parametric optimization study of a lithium-ion cell, Energy Procedia 138 (2017) 829–834, https://doi.org/10.1016/j.egypro.2017.10.088.

[104] J. Smekens, J. Paulsen, W. Yang, N. Omar, J. Deconinck, A. Hubin, et al., A Modified Multiphysics model for lithium-ion batteries with a LixNi1/3Mn1/3Co1/3O2 electrode, Electrochim. Acta 174 (2015) 615–624, https://doi.org/10.1016/j.electacta.2015.06.015.

[105] J. Mao, W. Tiedemann, J. Newman, Simulation of Li-ion cells by Dualfoil model under constant-resistance load, ECS Trans. 58 (48) (2014) 71–81, https://doi.org/10.1149/05848.0071ecst.

[106] P. Albertus, J. Newman, Introduction to Dualfoil 5.0. Berkley (2007) 1–6. http://www.cchem.berkeley.edu/jsngrp/fortran_files/Intro_Dualfoil5.pdf.

[107] M. Torchio, L. Magni, R.B. Gopaluni, R.D. Braatz, D.M. Raimondo, LIONSIMBA: A Matlab framework based on a finite volume model suitable for Li-Ion battery design, simulation, and control, J. Electrochem. Soc. 163 (7) (2016) A1192–A1205, https://doi.org/10.1149/2.0291607jes.

[108] Y. Li, M. Vilathgamuwa, T. Farrell, S.S. Choi, N.T. Tran, J. Teague, A physics-based distributed-parameter equivalent circuit model for lithium-ion batteries, Electrochim. Acta 299 (2019) 451–469, https://doi.org/10.1016/j.electacta.2018.12.167.

[109] W. Wu, X. Xiao, X. Huang, S. Yan, A multiphysics model for the in situ stress analysis of the separator in a lithium-ion battery cell, Comput. Mater. Sci. 83 (2014) 127–136, https://doi.org/10.1016/j.commatsci.2013.10.002.

[110] S. Kim, J. Wee, K. Peters, H.Y.S. Huang, Multiphysics coupling in lithium-ion batteries with reconstructed porous microstructures, J. Phys. Chem. C 122 (10) (2018) 5280–5290, https://doi.org/10.1021/acs.jpcc.7b12388.

[111] A. Carnovale, X. Li, A modeling and experimental study of capacity fade for lithium-ion batteries, Energy AI 2 (2020) 100032, https://doi.org/10.1016/j.egyai.2020.100032.

[112] S.C. Yang, Y. Hua, D. Qiao, Y.B. Lian, Y.W. Pan, Y.L. He, A coupled electrochemical-thermal-mechanical degradation modelling approach for lifetime assessment of lithium-ion batteries, Electrochim. Acta (2019) 326, https://doi.org/10.1016/j.electacta.2019.134928.

[113] D. Clerici, F. Mocera, A. Somà, Shape influence of active material micro-structure on diffusion and contact stress in lithium-ion batteries, Energies 14 (1) (2020) 134, https://doi.org/10.3390/en14010134.

[114] B. Hu, Z. Ma, W. Lei, Y. Zou, C. Lu, A chemo-mechanical model coupled with thermal effect on the hollow core–shell electrodes in lithium-ion batteries, Theor. Appl. Mech. Lett. 7 (4) (2017) 199–206, https://doi.org/10.1016/j.taml.2017.09.001.

[115] W. Wu, X. Xiao, M. Wang, X. Huang, A microstructural resolved model for the stress analysis of lithium-ion batteries, J. Electrochem. Soc. 161 (5) (2014) A803–A813, https://doi.org/10.1149/2.082405jes.

[116] X. Xiao, W. Wu, X. Huang, A multi-scale approach for the stress analysis of polymeric separators in a lithium-ion battery, J. Power Sources 195 (22) (2010) 7649–7660, https://doi.org/10.1016/j.jpowsour.2010.06.020.

[117] Y. Bai, Y. Zhao, W. Liu, B.X. Xu, Two-level modeling of lithium-ion batteries, J. Power Sources 422 (September 2018) (2019) 92–103, https://doi.org/10.1016/j.jpowsour.2019.03.026.

[118] D. Sauerteig, N. Hanselmann, A. Arzberger, H. Reinshagen, S. Ivanov, A. Bund, Electrochemical-mechanical coupled modeling and parameterization of swelling and ionic transport in lithium-ion batteries, J. Power Sources 378 (December 2017) (2018) 235–247, https://doi.org/10.1016/j.jpowsour.2017.12.044.

[119] A.R. Mandli, A. Kaushik, R.S. Patil, A. Naha, K.S. Hariharan, S.M. Kolake, et al., Analysis of the effect of resistance increase on the capacity fade of lithium ion batteries, Int. J. Energy Res. 43 (6) (2019) 2044–2056, https://doi.org/10.1002/er.4397.

[120] S.P. Rangarajan, Y. Barsukov, P.P. Mukherjee, Anode potential controlled charging prevents lithium plating, J. Mater. Chem. A 8 (26) (2020) 13077–13085, https://doi.org/10.1039/D0TA04467A.

[121] S.K. Heiskanen, J. Kim, B.L. Lucht, Generation and evolution of the solid electrolyte interphase of lithium-ion batteries, Joule 3 (10) (2019) 2322–2333, https://doi.org/10.1016/j.joule.2019.08.018.

[122] J. Wandt, P. Jakes, J. Granwehr, R.A. Eichel, H.A. Gasteiger, Quantitative and time-resolved detection of lithium plating on graphite anodes in lithium ion batteries, Mater. Today 21 (3) (2018) 231–240, https://doi.org/10.1016/j.mattod.2017.11.001.

[123] M. Petzl, M.A. Danzer, Nondestructive detection, characterization, and quantification of lithium plating in commercial lithium-ion batteries, J. Power Sources 254 (2014) 80–87, https://doi.org/10.1016/j.jpowsour.2013.12.060.

[124] M. Dubarry, B.Y. Liaw, Identify capacity fading mechanism in a commercial LiFePO4 cell, J. Power Sources 194 (1) (2009) 541–549, https://doi.org/10.1016/j.jpowsour.2009.05.036.

[125] L. Zhang, J. Li, C. Lyu, A novel method for capacity fade analysis of lithium-ion batteries based on multi-physics model, in: 2016 IEEE Int. Conf. Progn. Heal. Manag. ICPHM 2016, IEEE, 2016.

[126] H.K. Kim, C.J. Kim, C.W. Kim, K.J. Lee, Numerical analysis of accelerated degradation in large lithium-ion batteries, Comput. Chem. Eng. 112 (2018) (2018) 82–91, https://doi.org/10.1016/j.compchemeng.2017.12.019.

[127] G. Bai, P. Wang, Multiphysics based failure identification of lithium battery failure for prognostics, in: 2014 Int. Conf. Progn. Heal. Manag. PHM 2014, IEEE, 2014.

[128] Y. Xie, J. Li, C. Yuan, Multiphysics modeling of lithium ion battery capacity fading process with solid-electrolyte interphase growth by elementary reaction kinetics, J. Power Sources 248 (2014) 172–179, https://doi.org/10.1016/j.jpowsour.2013.09.059.

[129] C. Liu, L. Liu, Optimal design of Li-Ion batteries through multi-physics modeling and multi-objective optimization, J. Electrochem. Soc. 164 (11) (2017) E3254–E3264, https://doi.org/10.1149/2.0291711jes.

[130] A.A. Tahmasbi, M.H. Eikerling, Statistical physics-based model of mechanical degradation in lithium ion batteries, Electrochim. Acta 283 (2018) 75–87, https://doi.org/10.1016/j.electacta.2018.06.119.

[131] G. Ramos-Sanchez, F.A. Soto, J.M Martinez de la Hoz, Z. Liu, P.P. Mukherjee, F. El-Mellouhi, J.M. Seminario, P.B. Balbuena, Computational studies of interfacial reactions at anode materials: Initial stages of the solid-electrolyte-interphase layer formation, J. Electrochem. Energy Convers. Storage 13 (3) (2016), 031002, https://doi.org/10.1115/1.4034412.

[132] F. Röder, R.D. Braatz, U. Krewer, Multi-scale simulation of heterogeneous surface film growth mechanisms in lithium ion batteries, J. Electrochem. Soc. 164 (11) (2017) E3335–E3344, https://doi.org/10.1149/2.0241711jes.

[133] C. Shinagawa, H. Ushiyama, K. Yamashita, Multiscale simulations for lithium-Ion batteries: SEI film growth and capacity fading, J. Electrochem. Soc. 164 (13) (2017) A3018–A3024, https://doi.org/10.1149/2.0381713jes.

[134] M. Wang, X. Xiao, X. Huang, Study of lithium diffusivity in amorphous silicon via finite element analysis, J. Power Sources 307 (2016) 77–85, https://doi.org/10.1016/j.jpowsour.2015.12.082.

[135] Z. Cui, F. Gao, J. Qu, Interface-reaction controlled diffusion in binary solids with applications to lithiation of silicon in lithium-ion batteries, J. Mech. Phys. Solids 61 (2) (2013) 293–310, https://doi.org/10.1016/j.jmps.2012.11.001.

[136] S. Kalnaus, K. Rhodes, C. Daniel, A study of lithium ion intercalation induced fracture of silicon particles used as anode material in Li-ion battery, J. Power Sources 196 (19) (2011) 8116–8124, https://doi.org/10.1016/j.jpowsour.2011.05.049.

[137] S. Huang, F. Fan, J. Li, S. Zhang, T. Zhu, Stress generation during lithiation of high-capacity electrode particles in lithium ion batteries, Acta Mater. 61 (12) (2013) 4354–4364, https://doi.org/10.1016/j.actamat.2013.04.007.

[138] A. Sengupta, J. Chakraborty, Geometry and charging rate sensitively modulate surface stress-induced stress relaxation within cylindrical silicon anode particles in lithium-ion batteries, Acta Mech. 231 (3) (2020) 999–1019, https://doi.org/10.1007/s00707-019-02550-4.

[139] H. Yang, F. Fan, W. Liang, X. Guo, T. Zhu, S. Zhang, A chemo-mechanical model of lithiation in silicon, J. Mech. Phys. Solids 70 (2014) 349–361, https://doi.org/10.1016/j.jmps.2014.06.004.

[140] S. Pal, S. Damle, S. Patel, M.K. Dutta, P.N. Kumta, S. Maiti, Micromechanisms of capacity fade in silicon anode for Lithium-Ion batteries, ECS Trans. 41 (11) (2019) 87–99, https://doi.org/10.1149/1.3687394.

[141] J. Réthoré, H. Zheng, H. Li, J. Li, K.E. Aifantis, A multiphysics model that can capture crack patterns in Si thin films based on their microstructure, J. Power Sources 400 (February) (2018) 383–391, https://doi.org/10.1016/j.jpowsour.2018.07.106.

[142] C.R. Becker, K.E. Strawhecker, Q.P. McAllister, C.A. Lundgren, In situ atomic force microscopy of lithiation and delithiation of silicon nanostructures for lithium ion batteries, ACS Nano 7 (10) (2013) 9173–9182, https://doi.org/10.1021/nn4037909.

[143] T. Song, L. Hu, U. Paik, One-dimensional silicon nanostructures for Li ion batteries, J. Phys. Chem. Lett. 5 (4) (2014) 720–731, https://doi.org/10.1021/jz4027979.

[144] M. Wang, X. Xiao, X. Huang, A multiphysics microstructure-resolved model for silicon anode lithium-ion batteries, J. Power Sources 348 (2017) 66–79, https://doi.org/10.1016/j.jpowsour.2017.02.037.

[145] K. Zhang, Y. Zhang, J. Zhou, Y. Li, B. Zheng, F. Yang, et al., A stress-based charging protocol for silicon anode in lithium-ion battery: Theoretical and experimental studies, J. Energy Storage 32 (June) (2020), 101765, https://doi.org/10.1016/j.est.2020.101765.

[146] S. Pal, S.S. Damle, S.H. Patel, M.K. Datta, P.N. Kumta, S. Maiti, Modeling the delamination of amorphous-silicon thin film anode for lithium-ion battery, J. Power Sources 246 (2014) 149–159, https://doi.org/10.1016/j.jpowsour.2013.06.089.

[147] Z. Zheng, B. Chen, Y. Gurumukhi, J. Cook, M.N. Ates, N. Miljkovic, et al., Surrogate model assisted design of silicon anode considering lithiation induced stresses, IEEE Int. Reliab. Phys. Symp. Proc. (2019), https://doi.org/10.1109/IRPS.2019.8720601, 2019-March:1–6.

[148] B. Liu, Y. Jia, J. Li, H. Jiang, S. Yin, J. Xu, Multiphysics coupled computational model for commercialized Si/graphite composite anode, J. Power Sources 450 (January) (2020), 227667, https://doi.org/10.1016/j.jpowsour.2019.227667.

[149] B. Liu, X. Wang, H.S. Chen, S. Chen, Chen S Sen, H. Yang, J. Xu, H. Jiang, D. N. Fang, A simultaneous multiscale and multiphysics model and numerical implementation of a core-shell model for lithium-ion full-cell batteries, J. Appl. Mech. 86 (4) (2019), 041005, https://doi.org/10.1115/1.4042432.

[150] X. Gao, W. Lu, J. Xu, Modeling framework for multiphysics-multiscale behavior of Si–C composite anode, J. Power Sources 449 (December 2019) (2020), 227501, https://doi.org/10.1016/j.jpowsour.2019.227501.

[151] X. Gao, W. Lu, J. Xu, Unlocking multiphysics design guidelines on Si/C composite nanostructures for high-energy-density and robust lithium-ion battery anode, Nano Energy 81 (October 2020) (2021), 105591, https://doi.org/10.1016/j.nanoen.2020.105591.

[152] S. Yayathi, W. Walker, D. Doughty, H. Ardebili, Energy distributions exhibited during thermal runaway of commercial lithium ion batteries used for human spaceflight applications, J. Power Sources 329 (2016) 197–206, https://doi.org/10.1016/j.jpowsour.2016.08.078.

[153] B. Mao, P. Huang, H. Chen, Q. Wang, J. Sun, Self-heating reaction and thermal runaway criticality of the lithium ion battery, Int. J. Heat. Mass Transf. 149 (2020), 119178, https://doi.org/10.1016/j.ijheatmasstransfer.2019.119178.

[154] L. Sun, C. Wei, D. Guo, J. Liu, Z. Zhao, Z. Zheng, Y. Jin, Comparative study on Thermal runaway characteristics of lithium iron phosphate battery modules under different overcharge conditions, Fire Technol. 56 (2020) 1555–1574, https://doi.org/10.1007/s10694-019-00942-5.

[155] B. Liu, Y. Jia, J. Li, S. Yin, C. Yuan, Z. Hu, L. Wang, Y. Li, J. Xu, Safety issues caused by internal short circuits in lithium-ion batteries, J. Mater. Chem. A 6 (43) (2018) 21475–21484, https://doi.org/10.1039/C8TA08997C.

[156] Q. Wang, B. Mao, S.I. Stoliarov, J. Sun, A review of lithium ion battery failure mechanisms and fire prevention strategies, Prog. Energy Combust. Sci. 73 (2019) 95–131, https://doi.org/10.1016/j.pecs.2019.03.002.

[157] R. Kantharaj, A.M. Marconnet, Heat generation and thermal transport in lithium-ion batteries: A scale-bridging perspective, Nanoscale Microscale Thermophys. Eng. 23 (2) (2019) 128–156, https://doi.org/10.1080/15567265.2019.1572679.

[158] C. Zhang, S. Santhanagopalan, M.A. Sprague, A.A. Pesaran, Coupled mechanical-electrical-thermal modeling for short-circuit prediction in a lithium-ion cell under mechanical abuse, J. Power Sources 290 (2015) 102–113, https://doi.org/10.1016/j.jpowsour.2015.04.162.

[159] C. Yuan, X. Gao, H.K. Wong, B. Feng, J. Xu, A multiphysics computational framework for cylindrical battery behavior upon mechanical loading based on LS-DYNA, J. Electrochem. Soc. 166 (6) (2019) A1160–A1169, https://doi.org/10.1149/2.1071906jes.

[160] B. Liu, H. Zhao, H. Yu, J. Li, J. Xu, Multiphysics computational framework for cylindrical lithium-ion batteries under mechanical abusive loading, Electrochim. Acta 256 (2017) 172–184, https://doi.org/10.1016/j.electacta.2017.10.045.

[161] L. Yiding, W. Wenwei, L. Cheng, Z. Fenghao, High-efficiency multiphysics coupling framework for cylindrical lithium-ion battery under mechanical abuse, J. Clean. Prod. 286 (2021), 125451, https://doi.org/10.1016/j.jclepro.2020.125451.

[162] G. Kermani, E. Sahraei, Review: Characterization and modeling of the mechanical properties of lithium-ion batteries, Energies 10 (11) (2017), https://doi.org/10.3390/en10111730.

[163] B. Liu, Y. Jia, C. Yuan, L. Wang, X. Gao, S. Yin, et al., Safety issues and mechanisms of lithium-ion battery cell upon mechanical abusive loading: A review, Energy Storage Mater. 24 (June) (2020) 85–112, https://doi.org/10.1016/j.ensm.2019.06.036.

[164] S. Taslimi Taleghani, B. Marcos, G. Lantagne, Modeling and simulation of a commercial graphite–LiFePO₄ cell in a full range of C-rates, J. Appl. Electrochem. 48 (12) (2018) 1389–1400, https://doi.org/10.1007/s10800-018-1239-6.

[165] J.B. Sangiri, S. Ghosh, C. Chakraborty, Electro-thermal modeling of lithium-ion cell for higher discharge rate applications, in: Int. Conf. 21st Century Energy Needs - Mater. Syst. Appl. ICTFCEN 2016, IEEE, 2017.

[166] S. Wang, K. Li, Y. Tian, J. Wang, Y. Wu, S. Ji, An experimental and numerical examination on the thermal inertia of a cylindrical lithium-ion power battery, Appl. Therm. Eng. 154 (March) (2019) 676–685, https://doi.org/10.1016/j.applthermaleng.2019.03.141.

[167] S. Abada, M. Petit, A. Lecocq, G. Marlair, V. Sauvant-Moynot, F.. Huet, Combined experimental and modeling approaches of the thermal runaway of fresh and aged lithium-ion batteries, J. Power Sources 399 (April) (2018) 264–273, https://doi.org/10.1016/j.jpowsour.2018.07.094.

[168] M. Ye, G. Hu, F. Guo, W. Huang, Z. Wang, X. Zhao, et al., A novel semi-analytical solution for calculating the temperature distribution of the lithium-ion batteries during nail penetration based on Green's function method, Appl. Therm. Eng. 174 (2020), 115129, https://doi.org/10.1016/j.applthermaleng.2020.115129.

[169] P.T. Coman, S. Rayman, R.E. White, A lumped model of venting during thermal runaway in a cylindrical lithium cobalt oxide lithium-ion cell, J. Power Sources 307 (2016) 56–62, https://doi.org/10.1016/j.jpowsour.2015.12.088.

[170] Z. An, K. Shah, L. Jia, Y. Ma, Modeling and analysis of thermal runaway in Li-ion cell, Appl. Therm. Eng. 160 (May) (2019), 113960, https://doi.org/10.1016/j.applthermaleng.2019.113960.

[171] X. Ji, Y. Wang, J. Zhang, Understanding the anisotropic strain effects on lithium diffusion in graphite anodes: A first-principles study, Phys. B Condens. Matter 539 (2018) 66–71, https://doi.org/10.1016/j.physb.2018.03.046.

[172] X. Yan, A. Gouissem, P. Sharma, Atomistic insights into Li-ion diffusion in amorphous silicon, Mech. Mater. 91 (2015) 306–312, https://doi.org/10.1016/j.mechmat.2015.04.001.

[173] C. Chang, X. Li, Z. Xu, Microstructure- and concentration-dependence of lithium diffusion in the silicon anode: Kinetic Monte Carlo simulations and complex network analysis, Appl. Phys. Lett. 113 (12) (2018), 121904, https://doi.org/10.1063/1.5022334.

[174] Y. Gwak, J. Moon, M. Cho, Multi-scale analysis of an electrochemical model including coupled diffusion, stress, and nonideal solution in a silicon thin film anode, J. Power Sources 307 (2016) 856–865, https://doi.org/10.1016/j.jpowsour.2016.01.037.

[175] L. Kraft, J.B. Habedank, A. Frank, A. Rheinfeld, A. Jossen, Modeling and simulation of pore morphology modifications using laser-structured graphite anodes in lithium-ion batteries, J. Electrochem. Soc. 167 (1) (2020), 013506, https://doi.org/10.1149/2.0062001JES.

[176] J. Xu, G. Lindbergh, J. Varna, Multiphysics modeling of mechanical and electrochemical phenomena in structural composites for energy storage: Single carbon fiber micro-battery, J. Reinf. Plast. Compos. 37 (10) (2018) 701–715, https://doi.org/10.1177/0731684418760207.

[177] M. Chouchane, A. Rucci, T. Lombardo, A.C. Ngandjong, A.A. Franco, Lithium ion battery electrodes predicted from manufacturing simulations: Assessing the impact of the carbon-binder spatial location on the electrochemical performance, J. Power Sources 444 (2019), 227285, https://doi.org/10.1016/j.jpowsour.2019.227285.

[178] B. Yan, C. Lim, L. Yin, L. Zhu, Simulation of heat generation in a reconstructed LiCoO₂ cathode during galvanostatic discharge, Electrochim. Acta 100 (2013) 171–179, https://doi.org/10.1016/j.electacta.2013.03.132.

[179] Y. Ye, Y. Shi, A.A.O. Tay, Electro-thermal cycle life model for lithium iron phosphate battery, J. Power Sources 217 (2012) 509–518, https://doi.org/10.1016/j.jpowsour.2012.06.055.

[180] N. Yang, X. Zhang, B. Shang, G. Li, Unbalanced discharging and aging due to temperature differences among the cells in a lithium-ion battery pack with parallel combination, J. Power Sources 306 (2016) 733–741, https://doi.org/10.1016/j.jpowsour.2015.12.079.

[181] Q. Xia, Z. Wang, Y. Ren, L. Tao, C. Lu, J. Tian, et al., A modified reliability model for lithium-ion battery packs based on the stochastic capacity degradation and dynamic response impedance, J. Power Sources 423 (March) (2019) 40–51, https://doi.org/10.1016/j.jpowsour.2019.03.042.

[182] S. Abada, G. Marlair, A. Lecocq, M. Petit, V. Sauvant-Moynot, F. Huet, Safety focused modeling of lithium-ion batteries: A review, J. Power Sources 306 (2016) 178–192, https://doi.org/10.1016/j.jpowsour.2015.11.100.

[183] J. Hu, H. He, Z. Wei, Y. Li, Disturbance-immune and aging-robust internal short circuit diagnostic for lithium-ion battery, IEEE Trans. Ind. Electron. (2021), https://doi.org/10.1109/TIE.2021.3063968 (c).

[184] Z. Wei, Z. Quan, J. Wu, Y. Li, J. Pou, H. Zhong, Deep deterministic policy gradient-DRL enabled multiphysics-constrained fast charging of lithium-ion battery, IEEE Trans. Ind. Electron. (2021), https://doi.org/10.1109/TIE.2021.3070514 (c).

[185] Z. Wei, J. Zhao, H. He, G. Ding, H. Cui, L. Liu, Future smart battery and management: Advanced sensing from external to embedded multi-dimensional measurement, J. Power Sources 489 (November 2020) (2021), 229462, https://doi.org/10.1016/j.jpowsour.2021.229462.

[186] M. Ragone, V. Yurkiv, A. Ramasubramanian, B. Kashir, F. Mashayek, Data driven estimation of electric vehicle battery state-of-charge informed by automotive simulations and multi-physics modeling, J. Power Sources 483 (November 2020) (2021), 229108, https://doi.org/10.1016/j.jpowsour.2020.229108.

[187] T. Yamanaka, Y. Takagishi, T. Yamaue, A framework for optimal safety Li-ion batteries design using physics-based models and machine learning approaches, J. Electrochem. Soc. 167 (10) (2020), 100516, https://doi.org/10.1149/1945-7111/ab975c.

[188] N.T. Tran, M. Vilathgamuwa, T. Farrell, S.S. Choi, Y. Li, J. Teague, A computationally-efficient electrochemical-thermal model for small-format cylindrical lithium ion batteries, in: 2018 IEEE 4th South Power Electron. Conf. SPEC 2018, IEEE, 2018, pp. 1–7.

[189] M.G. Hennessy, I.R. Moyles, Asymptotic reduction and homogenization of a thermo-electrochemical model for a lithium-ion battery, Appl. Math. Model. 80 (2020) 724–754, https://doi.org/10.1016/j.apm.2019.11.018.

[190] X. Lin, X. Hao, Z. Liu, W. Jia, Health conscious fast charging of Li-ion batteries via a single particle model with aging mechanisms, J. Power Sources 400 (2018) 305–316, https://doi.org/10.1016/j.jpowsour.2018.08.030.

[191] N. Lotfi, R.G. Landers, S. Member, J. Li, J. Park, Reduced-order electrochemical model-based uncertainty estimation, IEEE Trans. Control Syst. Technol. 25 (4) (2017) 1217–1230, https://doi.org/10.1109/TCST.2016.2598764.

[192] N. Diorio, A. Dobos, S. Janzou, A. Nelson, B. Lundstrom, N Diorio, et al., Technoeconomic modeling of battery energy storage in SAM. NREL (2015). http://www.nrel.gov/docs/fy15osti/64641.pdf.

[193] K. Anoune, M. Bouya, A. Astito, A. Ben Abdellah, Sizing methods and optimization techniques for PV-wind based hybrid renewable energy system: A review, Renew. Sustain. Energy Rev. 93 (May) (2018) 652–673, https://doi.org/10.1016/j.rser.2018.05.032.

[194] M.P. Bonkile, V. Ramadesigan, Power management control strategy using physics-based battery models in standalone PV-battery hybrid systems, J. Energy Storage 23 (2019) 258–268, https://doi.org/10.1016/j.est.2019.03.016. December 2018Available from:.

[195] V. Toniazzo, New separators for industrial and specialty lead acid batteries, J. Power Sources 107 (2) (2002) 211–216, https://doi.org/10.1016/S0378-7753(01)01073-4.

[196] V. Toniazzo, The key to success: Gelled-electrolyte and optimized separators for stationary lead-acid batteries, J. Power Sources 158 (2) (2006) 1124–1132, https://doi.org/10.1016/j.jpowsour.2006.02.106. SPEC. ISS.

[197] S. Shukla, V. Kumar, P.V. Kameswara Rao, S. Sharma, D. Sebők, I. Szenti, et al., Probing the three-dimensional porous and tortuous nature of absorptive glass mat (AGM) separators, J. Energy Storage 27 (August 2019) (2020), 101003, https://doi.org/10.1016/j.est.2019.101003.

[198] K.S. Gandhi, Modeling of sulfation in a flooded lead-acid battery and prediction of its cycle life, J. Electrochem. Soc. 167 (1) (2020), 013538, https://doi.org/10.1149/1945-7111/ab679b.

[199] V. Esfahanian, F. Torabi, Numerical simulation of lead-acid batteries using Keller-Box method, J. Power Sources 158 (2) (2006) 949–952, https://doi.org/10.1016/j.jpowsour.2005.11.031. SPEC. ISS.

[200] V.D. Munoz-Carpio, J. Mason, I. Celik, F. Elizalde-Blancas, A. Alatorre-Ordaz, Numerical and experimental study of lead-acid battery, in: ASME 2016 Heat Transf. Summer Conf., ASME, 2018, pp. 3–10.

[201] H. Pourmirzaagha, V. Esfahanian, F. Sabetghadam, F. Torabi, Single and multi-objective optimization for the a enhancement of lead–acid battery cell, Int. J. Energy Res. 40 (14) (2016) 1966–1978, https://doi.org/10.1002/er.3574.

[202] R.D. Prengaman, Current-collectors for lead-acid batteries, Lead-Acid Batteries for Future Automobiles (2017) 269–299, https://doi.org/10.1016/B978-0-444-63700-0.00009-X.

[203] A. Kirchev, Alternative current-collectors, Lead-Acid Batteries for Future Automobiles (2017) 301–321, https://doi.org/10.1016/B978-0-444-63700-0.00010-6.

[204] R. Wagner, Encyclopedia of electrochemical power sources, Encycl. Electrochem. Power Sources (2009) 677–692, https://doi.org/10.1016/B978-044452745-5.00138-6. http://www.sciencedirect.com/science/article/pii/B9780444527455001386.

[205] R. Tenno, E. Nefedov, Electrolyte depletion control laws for lead-acid battery discharge optimisation, J. Power Sources 270 (2014) 658–667, https://doi.org/10.1016/j.jpowsour.2014.07.154.

[206] F. Torabi, V. Esfahanian, Study of thermal-runaway in batteries, J. Electrochem. Soc. 160 (2) (2013) A223–A234, https://doi.org/10.1149/2.030302jes.

[207] M. Huck, D.U. Sauer, Modeling transient processes in lead-acid batteries in the time domain, J. Energy Storage 29 (April) (2020), 101430, https://doi.org/10.1016/j.est.2020.101430.

[208] V. Esfahanian, F. Torabi, A. Mosahebi, An innovative computational algorithm for simulation of lead-acid batteries, J. Power Sources 176 (1) (2008) 373–380, https://doi.org/10.1016/j.jpowsour.2007.10.052.

[209] S.A.U.A. Madusanka, D.M.O.R. Mahadiulwewa, S.P.A.A.J. Samarakoon, K.A.H. Sandeepanie, R.M.T. Damayanthi, Improving the performance of lead acid batteries using nano-technology, in: MERCon 2019 - Proceedings, 5th Int. Multidiscip. Moratuwa. Eng. Res. Conf., IEEE, 2019, pp. 589–593.

[210] K. Siniard, M. Xiao, S.Y. Choe, One-dimensional dynamic modeling and validation of maintenance-free lead-acid batteries emphasizing temperature effects, J. Power Sources 195 (20) (2010) 7102–7114, https://doi.org/10.1016/j.jpowsour.2010.04.056.

[211] T. Nazghelichi, F. Torabi, V. Esfahanian, Reducing the charging time of a lead–acid cell in the sense of linear stability analysis, J. Energy Storage 36 (February) (2021), 102369, https://doi.org/10.1016/j.est.2021.102369.

[212] P. Vyroubal, J. Maxa, J. Tichy, P. Baca, Simulation of charging and discharging process in the lead acid battery, ECS Trans. 48 (1) (2014) 105–113, https://doi.org/10.1149/04801.0105ecst.

[213] M. Huck, J. Badeda, D. Uwe Sauer, Modeling the crystal distribution of lead-sulfate in lead-acid batteries with 3D spatial resolution, J. Power Sources 279 (2015) 351–357, https://doi.org/10.1016/j.jpowsour.2014.12.157.

[214] A. Bates, S. Mukerjee, S.C. Lee, D. Lee, S. Park, An analytical study of a lead-acid flow battery as an energy storage system, J. Power Sources 249 (2014) 207–218, https://doi.org/10.1016/j.jpowsour.2013.10.090.

[215] X. Zhang, S. Luo, H. Liu, C. Wang, Numerical studies of the effectiveness of electrodes with conductive dots in flow batteries, in: ASME 2016 Int. Mech. Eng. Congr. Expo., ASME, 2016.

[216] A. Oury, A. Kirchev, Y. Bultel, A numerical model for a soluble lead-acid flow battery comprising a three-dimensional honeycomb-shaped positive electrode, J. Power Sources 246 (2014) 703–718, https://doi.org/10.1016/j.jpowsour.2013.07.101.

[217] M.G. Insinga, S. Pisana, R.L. Oliveri, C. Sunseri, R. Inguanta, Performance of lead-acid batteries with nanostructured electrodes at different temperature, in: IEEE 4th Int. Forum Res. Technol. Soc. Ind. RTSI 2018 - Proc., IEEE, 2018, pp. 18–21.

[218] M. Caruso, V. Castiglia, R. Miceli, C. Nevoloso, P. Romano, G. Schettino, F. Viola, M.G. Insinga, A. Moncada, R.L. Oliveri, F. Ganci, C. Sunseri, S. Piazza, R. Inguanta, Nanostructured lead acid battery for electric vehicles applications, in: 2017 Int Conf. Electr. Electron. Technol. Automot., IEEE, 2017.

[219] V. Sulzer, S.J. Chapman, C.P. Please, D.A. Howey, C.W. Monroe, Faster lead-acid battery simulations from porous-electrode theory: Part II. asymptotic analysis, J. Electrochem. Soc. 166 (12) (2019) A2372–A2382, https://doi.org/10.1149/2.0441908jes.

[220] C. Choi, S. Kim, R. Kim, Y. Choi, S. Kim, H.Y. Jung, J.H. Yang, H.T. Kim, A review of vanadium electrolytes for vanadium redox flow batteries, Renew. Sustain. Energy Rev. 69 (November 2016) (2017) 263–274, https://doi.org/10.1016/j.rser.2016.11.188.

[221] P.A. Boettcher, E. Agar, C.R. Dennison, E.C. Kumbur, Modeling of ion crossover in vanadium redox flow batteries: A computationally-efficient lumped parameter approach for extended cycling, J. Electrochem. Soc. 163 (1) (2016) A5244–A5252, https://doi.org/10.1149/2.031601jes.

[222] T. Liu, X. Li, H. Zhang, J. Chen, Progress on the electrode materials towards vanadium flow batteries (VFBs) with improved power density, J. Energy Chem. 27 (5) (2018) 1292–1303, https://doi.org/10.1016/j.jechem.2018.07.003.

[223] S. Yang, S. Cheng, X. Xiao, H. Pang, Development and application of carbon fiber in batteries, Chem. Eng. J. 384 (2020), 123294, https://doi.org/10.1016/j.cej.2019.123294.

[224] X. Li, H. Zhang, Z. Mai, H. Zhang, I. Vankelecom, Ion exchange membranes for vanadium redox flow battery (VRB) applications, Energy Environ. Sci. 4 (4) (2011) 1147–1160, https://doi.org/10.1039/C0EE00770F.

[225] B. Jiang, L. Wu, L. Yu, X. Qiu, J. Xi, A comparative study of Nafion series membranes for vanadium redox flow batteries, J. Memb. Sci. 510 (2016) 18–26, https://doi.org/10.1016/j.memsci.2016.03.007.

[226] C.H. Chen, K. Yaji, S. Yamasaki, S. Tsushima, K. Fujita, Computational design of flow fields for vanadium redox flow batteries via topology optimization, J. Energy Storage 26 (July) (2019), 100990, https://doi.org/10.1016/j.est.2019.100990.

[227] M. Messaggi, P. Canzi, R. Mereu, A. Baricci, F. Inzoli, A. Casalegno, et al., Analysis of flow field design on vanadium redox flow battery performance: development of 3D computational fluid dynamic model and experimental validation, Appl. Energy 228 (June) (2018) 1057–1070, https://doi.org/10.1016/j.apenergy.2018.06.148.

[228] J. Houser, J. Clement, A. Pezeshki, M.M. Mench, Influence of architecture and material properties on vanadium redox flow battery performance, J. Power Sources 302 (2016) 369–377, https://doi.org/10.1016/j.jpowsour.2015.09.095.

[229] E. Prumbohm, G.D. Wehinger, Exploring flow characteristics in vanadium redox-flow batteries: Optical measurements and CFD simulations, Chem. Ing. Tech. 91 (6) (2019) 900–906, https://doi.org/10.1002/cite.201800164.

[230] H.A. Ozgoli, S. Elyasi, M. Mollazadeh, Hydrodynamic and electrochemical modeling of vanadium redox flow battery, Mech. Ind. 16 (2) (2015), https://doi.org/10.1051/meca/2014071.

[231] M. Vynnycky, M. Assuncao, The vanadium redox flow battery: An asymptotic perspective, SIAM J. Appl. Math. 79 (4) (2019) 1147–1172, https://doi.org/10.1137/18M1168984.

[232] Q. Xu, T.S. Zhao, Fundamental models for flow batteries, Prog. Energy Combust. Sci. 49 (2015) 40–58, https://doi.org/10.1016/j.pecs.2015.02.001.

[233] S. Won, K. Oh, H. Ju, Numerical studies of carbon paper-based vanadium redox flow batteries, Electrochim. Acta 201 (2016) 286–299, https://doi.org/10.1016/j.electacta.2015.11.091.

[234] A.K. Sharma, C.Y. Ling, E. Birgersson, M. Vynnycky, M. Han, Verified reduction of dimensionality for an all-vanadium redox flow battery model, J. Power Sources 279 (2015) 345–350, https://doi.org/10.1016/j.jpowsour.2015.01.019.

[235] D. Jeong, S. Jung, Numerical analysis of cycling performance of vanadium redox flow battery, Int. J. Energy Res. 44 (7) (2020) 5209–5222, https://doi.org/10.1002/er.5261.

[236] Y. Wang, S.C. Cho, Analysis and three-dimensional modeling of vanadium flow batteries, J. Electrochem. Soc. 161 (9) (2014) A1200–A1212, https://doi.org/10.1149/2.0061409jes.

[237] D. Krishnamurthy, E.O. Johansson, J.W. Lee, E. Kjeang, Computational modeling of microfluidic fuel cells with flow-through porous electrodes, J. Power Sources 196 (23) (2011) 10019–10031, https://doi.org/10.1016/j.jpowsour.2011.08.024.

[238] J.Q. Chen, B.G. Wang, H.L. Lv, Numerical simulation and experiment on the electrolyte flow distribution for all vanadium redox flow battery, Adv. Mater. Res. 236–238 (2011) 604–607, https://doi.org/10.4028/www.scientific.net/AMR.236-238.604.

[239] J. Lee, J. Kim, H. Park, Numerical simulation of the power-based efficiency in vanadium redox flow battery with different serpentine channel size, Int. J. Hydrog. Energy 44 (56) (2019) 29483–29492, https://doi.org/10.1016/j.ijhydene.2019.05.013.

[240] F. Li, Y. Wei, P. Tan, Y. Zeng, Y. Yuan, Numerical investigations of effects of the interdigitated channel spacing on overall performance of vanadium redox flow batteries, J. Energy Storage 32 (August) (2020), 101781, https://doi.org/10.1016/j.est.2020.101781.

[241] K. Yaji, S. Yamasaki, S. Tsushima, T. Suzuki, K. Fujita, Topology optimization for the design of flow fields in a redox flow battery, Struct. Multidiscip. Optim. 57 (2) (2018) 535–546, https://doi.org/10.1007/s00158-017-1763-8.

[242] K. Yaji, S. Yamasaki, S. Tsushima, K. Fujita, A framework of multi-fidelity topology design and its application to optimum design of flow fields in battery systems, Proc. ASME Des. Eng. Tech. Conf. (2019), https://doi.org/10.1115/DETC2019-97675, 2A-2019.

[243] W. Chen, J. Kang, Optimization of electrolyte flow and vanadium ions conversion by utilizing variable porosity electrodes in vanadium redox flow batteries, Chem. Phys. 529 (October 2019) (2020), 110577, https://doi.org/10.1016/j.chemphys.2019.110577.

[244] S. Tsushima, T. Suzuki, Modeling and simulation of vanadium redox flow battery with interdigitated flow field for optimizing electrode architecture, J. Electrochem. Soc. 167 (2) (2020), 020553, https://doi.org/10.1149/1945-7111/ab6dd0.

[245] S. Sujali, M.R. Mohamed, A.N. Oumer, A. Ahmad, P. Leung, Study on architecture design of electroactive sites on Vanadium Redox Flow Battery (V-RFB), in: E3S Web Conf. 80, EDP Sciences, 2019, pp. 1–5.

[246] X. Wu, X. Yuan, Z. Wang, J. Liu, Y. Hu, Q. Deng, et al., Electrochemical performance of 5 kW all-vanadium redox flow battery stack with a flow frame of multi-distribution channels, J. Solid State Electrochem. 21 (2) (2017) 429–435, https://doi.org/10.1007/s10008-016-3361-x.

[247] Y. Kim, Y.Y. Choi, N. Yun, M. Yang, Y. Jeon, K.J. Kim, et al., Activity gradient carbon felt electrodes for vanadium redox flow batteries, J. Power Sources 408 (2018) 128–135, https://doi.org/10.1016/j.jpowsour.2018.09.066.

[248] S.E. Ibáñez, A.E. Quintero, P.A. García-Salaberri, M. Vera, Effects of the diffusive mixing and self-discharge reactions in microfluidic membraneless vanadium redox flow batteries, Int. J. Heat Mass Transf. 170 (2021), 121022, https://doi.org/10.1016/j.ijheatmasstransfer.2021.121022.

[249] L. Li, S. Bei, R. Liu, Q. Xu, K. Zheng, Y. She, Y. He, Design of a radial vanadium redox microfluidic fuel cell: A new way to break the size limitation, Int. J. Energy Res. 43 (7) (2019) 3028–3037, https://doi.org/10.1002/er.4473.

[250] J.W. Lee, D. Krishnamurthy, P. Hsiao, E. Kjeang, A parametric study on microfluidic vanadium fuel cells, in: Proc. ASME 2011 9th Fuel Cell Sci. Eng. Technol. Conf., ASME, 2012, pp. 653–661.

[251] L. Li, G. Nikiforidis, M.K.H. Leung, W.A. Daoud, Vanadium microfluidic fuel cell with novel multi-layer flow-through porous electrodes: Model, simulations and experiments, Appl. Energy 177 (2016) 729–739, https://doi.org/10.1016/j.apenergy.2016.05.072.

[252] M. Tanveer, K.Y. Kim, A membraneless microfluidic fuel cell with a hollow flow channel and porous flow-through electrodes, Int. J. Energy Res. 45 (6) (2021) 8536–8550, https://doi.org/10.1002/er.6390.

[253] M. Tanveer, K.Y. Kim, Effects of geometric configuration of the channel and electrodes on the performance of a membraneless micro-fuel cell, Energy Convers. Manag. 136 (2017) 372–381, https://doi.org/10.1016/j.enconman.2017.01.027.

[254] T. Ouyang, J. Chen, F. Zhou, J. Lu, P. Xu, N. Chen, C. Mo, Effects of force field and design parameters on the exergy efficiency and fuel utilization of microfluidic fuel cells, Int. J. Hydrog. Energy 45 (22) (2020) 12443–12458, https://doi.org/10.1016/j.ijhydene.2020.02.172.

[255] S. Jung, B. Choi, S. Park, D.W. Lee, Y.B. Kim, S. Kim, Computational study of effects of contact resistance on a large-scale vanadium redox flow battery stack, Int. J. Energy Res. 43 (6) (2019) 2343–2360, https://doi.org/10.1002/er.4453.

[256] J. Xiong, Y. Song, S. Wang, X. Li, J. Liu, C. Yan, A. Tang, Evaluation of the influence of clamping force in electrochemical performance and reliability of vanadium redox flow battery, J. Power Sources 431 (December 2018) (2019) 170–181, https://doi.org/10.1016/j.jpowsour.2019.05.061.

[257] M. Yue, Z. Lv, Q. Zheng, X. Li, H. Zhang, Battery assembly optimization: Tailoring the electrode compression ratio based on the polarization analysis in vanadium flow batteries, Appl. Energy 235 (November 2018) (2019) 495–508, https://doi.org/10.1016/j.apenergy.2018.10.136.

[258] K. Bromberger, J. Kaunert, T. Smolinka, A model for all-vanadium redox flow batteries: Introducing electrode-compression effects on voltage losses and hydraulics, Energy Technol. 2 (1) (2014) 64–76, https://doi.org/10.1002/ente.201300114.

[259] S.K. Park, J. Shim, J.H. Yang, C.S. Jin, B.S. Lee, Y.S. Lee, et al., The influence of compressed carbon felt electrodes on the performance of a vanadium redox flow battery, Electrochim. Acta 116 (2014) 447–452, https://doi.org/10.1016/j.electacta.2013.11.073.

[260] N. Gurieff, V. Timchenko, C. Menictas, Variable porous electrode compression for redox flow battery systems, Batteries 4 (4) (2018), https://doi.org/10.3390/batteries4040053.

[261] S Kumar, S. Jayanti, Effect of electrode intrusion on pressure drop and electrochemical performance of an all-vanadium redox flow battery, J. Power Sources 360 (2017) 548–558, https://doi.org/10.1016/j.jpowsour.2017.06.045.

[262] Q. Wang, Z.G. Qu, Z.Y. Jiang, W.W. Yang, Numerical study on vanadium redox flow battery performance with non-uniformly compressed electrode and serpentine flow field, Appl. Energy 220 (September 2017) (2018) 106–116, https://doi.org/10.1016/j.apenergy.2018.03.058.

[263] E. Agar, K.W. Knehr, D. Chen, M.A. Hickner, E.C. Kumbur, Species transport mechanisms governing capacity loss in vanadium flow batteries: Comparing Nafion® and sulfonated Radel membranes, Electrochim. Acta 98 (2013) 66–74, https://doi.org/10.1016/j.electacta.2013.03.030.

[264] E. Agar, A. Benjamin, C.R. Dennison, D. Chen, M.A. Hickner, E.C. Kumbur, Reducing capacity fade in vanadium redox flow batteries by altering charging and discharging currents, J. Power Sources 246 (2014) 767–774, https://doi.org/10.1016/j.jpowsour.2013.08.023.

[265] Y.S. Chou, S.C. Yen, A. Arpornwichanop, B. Singh, Y.S. Chen, Mathematical model to study vanadium ion crossover in an all-vanadium redox flow battery, ACS Sustain. Chem. Eng. 9 (15) (2021) 5377–5387, https://doi.org/10.1021/acssuschemeng.1c00233.

[266] Y. Lei, B.W. Zhang, B.F. Bai, T.S. Zhao, A transient electrochemical model incorporating the Donnan effect for all-vanadium redox flow batteries, J. Power Sources 299 (2015) 202–211, https://doi.org/10.1016/j.jpowsour.2015.08.100.

[267] M.Y. Lu, W.W. Yang, Y.M. Deng, W.Z. Li, Q. Xu, Y.L. He, Mitigating capacity decay and improving charge-discharge performance of a vanadium redox flow battery with asymmetric operating conditions, Electrochim. Acta 309 (2019) 283–299, https://doi.org/10.1016/j.electacta.2019.04.032.

[268] M.Y. Lu, W.W. Yang, X.S. Bai, Y.M. Deng, Y.L. He, Performance improvement of a vanadium redox flow battery with asymmetric electrode designs, Electrochim. Acta 319 (2019) 210–226, https://doi.org/10.1016/j.electacta.2019.06.158.

[269] Y. Ashraf Gandomi, T.A. Zawodzinski, M.M. Mench, Concentrated solution model of transport in all vanadium redox flow battery membrane separator, ECS Trans. 61 (13) (2014) 23–32, https://doi.org/10.1149/06113.0023ecst.

[270] A.R. Crothers, R.M. Darling, D.I. Kushner, M.L. Perry, A.Z. Weber, Theory of multicomponent phenomena in cation-exchange membranes: Part III. Transport in vanadium redox-flow-battery separators, J. Electrochem. Soc. 167 (1) (2020), 013549, https://doi.org/10.1149/1945-7111/ab6725.

[271] J. Lohaus, D. Rall, M. Kruse, V. Steinberger, M. Wessling, On charge percolation in slurry electrodes used in vanadium redox flow batteries, Electrochem. Commun. 101 (February) (2019) 104–108, https://doi.org/10.1016/j.elecom.2019.02.013.

[272] K.C. Smith, Y.M. Chiang, W. Craig Carter, Maximizing energetic efficiency in flow batteries utilizing non-newtonian fluids, J. Electrochem. Soc. 161 (4) (2014) A486–A496, https://doi.org/10.1149/2.011404jes.

[273] L. Chen, Y.L. He, W.Q. Tao, P. Zelenay, R. Mukundan, Q. Kang, Pore-scale study of multiphase reactive transport in fibrous electrodes of vanadium redox flow batteries, Electrochim. Acta 248 (2017) 425–439, https://doi.org/10.1016/j.electacta.2017.07.086.

[274] M.A. Sadeghi, M. Aganou, M. Kok, M. Aghighi, G. Merle, J. Barralet, et al., Exploring the impact of electrode microstructure on redox flow battery performance using a multiphysics pore network model, J. Electrochem. Soc. 166 (10) (2019) A2121–A2130, https://doi.org/10.1149/2.0721910jes.

[275] B. Chakrabarti, E. Kalamaras, A.K. Singh, A. Bertei, J. Rubio-Garcia, V. Yufit, K. Tenny, B. Wu, F. Tariq, Y.S. Hajimolana, N.P. Brandon, C.T.J. Low, E.P. L. Roberts, Y.M. Chiang, F.R. Brushett, Modelling of redox flow battery electrode processes at a range of length scales: A review, Sustain. Energy Fuels 4 (2020) 5433–5468, https://doi.org/10.1039/D0SE00667J. http://pubs.rsc.org/en/Content/ArticleLanding/2020/SE/D0SE00667J.

[276] M. Skyllas-Kazacos, J. McCann, Y. Li, J. Bao, A. Tang, The mechanism and modelling of shunt current in the vanadium redox flow battery, ChemistrySelect 1 (10) (2016) 2249–2256, https://doi.org/10.1002/slct.201600432.

[277] F. Moro, A. Trovò, S. Bortolin, D. Del Col, M. Guarnieri, An alternative low-loss stack topology for vanadium redox flow battery: Comparative assessment, J. Power Sources 340 (2017) 229–241, https://doi.org/10.1016/j.jpowsour.2016.11.042.

[278] C. Yin, S. Guo, H. Fang, J. Liu, Y. Li, H. Tang, Numerical and experimental studies of stack shunt current for vanadium redox flow battery, Appl. Energy 151 (2015) 237–248, https://doi.org/10.1016/j.apenergy.2015.04.080.

[279] X. Ke, J.I.D. Alexander, J.M. Prahl, R.F. Savinell, A simple analytical model of coupled single flow channel over porous electrode in vanadium redox flow battery with serpentine flow channel, J. Power Sources 288 (2015) 308–313, https://doi.org/10.1016/j.jpowsour.2015.04.138.

[280] Z. Wei, J. Zhao, B. Xiong, Dynamic electro-thermal modeling of all-vanadium redox flow battery with forced cooling strategies, Appl. Energy 135 (2014) 1–10, https://doi.org/10.1016/j.apenergy.2014.08.062.

[281] Z. Wei, T.M. Lim, M. Skyllas-Kazacos, N. Wai, K.J. Tseng, Online state of charge and model parameter co-estimation based on a novel multi-timescale estimator for vanadium redox flow battery, Appl. Energy 172 (2016) 169–179, https://doi.org/10.1016/j.apenergy.2016.03.103.

[282] X. Gao, W. Lu, J. Xu, Modeling framework for multiphysics-multiscale behavior of Si–C composite anode, J. Power Sources 449 (August) (2020), 227501, https://doi.org/10.1016/j.jpowsour.2019.227501.

[283] B. Liu, Y. Jia, J. Li, H. Jiang, S. Yin, J. Xu, Multiphysics coupled computational model for commercialized Si/graphite composite anode, J. Power Sources 450

(October 2019) (2020), 227667, https://doi.org/10.1016/j.jpowsour.2019.227667.

[284] Pinjari N., Kumar B., Bhargav A., Ruch P., Effect of electrode properties on performance on miniaturized vanadium redox flow battery, 16th IEEE Intersociety Conference on Thermal and Thermomechanical Phenomena in Electronic Systems (ITHERM) (2017), doi: 10.1109/ITHERM.2017.7992603.

[285] J. Manwell, J.G. McGowan, Lead acid battery storage model for hybrid energy systems, Sol. Energy 50 (5) (1993) 399–405, https://doi.org/10.1016/0038-092X(93)90060-2.

[286] HOMER Energy, HOMER Pro 3.14 user manual. https://www.homerenergy.com/products/pro/docs/latest/index.html, 2021 (accessed 19 June 2021).